DISS. ETH Nr. 11816

Measurements Using Missing Energy in semileptonic b-Decays

DISSERTATION

for the degree of
DOCTOR OF NATURAL SCIENCES

of the
SWISS FEDERAL INSTITUTE OF TECHNOLOGY ZURICH

presented by
Frank Behner

Dipl.–Phys. ETH-Zürich

born November 20, 1963
in Cologne, Nordrhein-Westfalen, Bundesrepublik Deutschland

Accepted on the recommendation of

Prof. Dr. H. Hofer examiner
Prof. Dr. F. Pauss co-examiner

- 1996 -

Contents

Abstract ix

Zusammenfassung xi

Introduction 1

1 Theoretical overview 3

1.1 A glance at the Standard Model . . . 3

1.2 What can be learned from semileptonic B- decays? . . . 11

1.3 Hadronization . . . 14

1.4 Consequences for models beyond the Standard Model . . . 18

2 Experimental Apparatus 21

2.1 The accelerator . . . 21

2.2 The detector . . . 22

2.2.1 The tracking system . . . 23

2.2.2 Calorimeters . . . 25

2.2.3 The muon system . . . 28

2.3 Data processing . . . 29

3 Event classification 33

3.1 Hadron selection . . . 33

3.2 B-tagging with leptons . . . 41

3.3 Tagging with the event distance . . . 48

3.4 High x tag . . . 50

4 Jet-energy measurement and calibration 51

4.1 Detector response to jets . . . 51

4.1.1 Response to single particles . . . 51

4.1.2 Noise reduction . . . 57

4.1.3 Jet energy calibration . . . 60

4.2 Energy scale determination . . . 64

5 Measurements and Results **69**
5.1 Monte Carlo parameters and fragmentation function 70
5.2 Direct measurement of the semileptonic branching ratio B $\rightarrow$ e(μ)νX 71
5.2.1 Measurement with electrons 71
5.2.2 Measurement with muons 77
5.2.3 Systematic uncertainties related to the two jet sample . . . 82
5.3 Testing the space-time structure in weak b-decays 85
5.4 The branching ratio b$\rightarrow$ ν X and b$\rightarrow$ $\tau\nu$ X 86

6 Summary and Conclusions **95**
6.1 The space time structure of the weak charged current 95
6.2 The semileptonic branching ratios and consequences for the CKM matrix 96
6.3 Comparison of Br(b $\rightarrow$ $\tau\nu$X) with theory 100
6.4 Final conclusions 103

A Calibration of the TEC **105**

Bibliography **115**

Acknowledgement **123**

Curriculum Vitae **125**

List of Figures

1.1 The higgs potential 4

1.2 Feynman graphs showing the different decay modes of B-mesons. . 10

1.3 The semileptonic b-decay in the spectator model with polarisation at the b-decay vertex. 13

1.4 The semileptonic b-hadron decay with no polarisation at the hadron decay vertex. 14

1.5 The energy spectrum of leptons and neutrinos with V-A×V-A coupling for a given b-hadron energy. 15

1.6 Difference in the neutrino spectra for agreeing charged lepton spectra with different models. 16

1.7 The normalised Peterson function for a typical value $\epsilon = 0.003$ used for b-quark fragmentation. 18

2.1 The location of the LEP ring and its four experiments. 22

2.2 The LEP injector chain. 23

2.3 An overview of the L3 detector 24

2.4 The TEC with its subcomponents. 24

2.5 A TEC segment 26

2.6 View on a BGO crystal of the electro-calorimeter 27

2.7 An overview of the parts of the detector which are inside the support tube. 28

2.8 r-ϕ view of an octant of the muon system. 29

2.9 The event dataflow up to the point where the physics analysis starts. 30

3.1 The visible energy relative to the beam energy. 35

3.2 The number of calorimetric clusters for different event sources. . . 35

3.3 The relative energy balance. 36

3.4 Number of tracks 37

3.5 Number of tracks with tighter track selection to reject $Z \rightarrow \tau\tau$ events. 38

3.6 Correlation of the number of cluster in the two hemispeheres for events with less than 10 good tracks. 39

3.7 The correlation of the number of tracks in the two hemispeheres of the remaining events before the three tracks against three tracks cut. 40

3.8 The energy ratio E9/E25 42
3.9 The number of crystals associated to a cluster 43
3.10 The energy of the BGO clusters 43
3.11 The energy in the cone of 50mrad behind the BGO in the hadron calorimeter 44
3.12 The distribution of the angle of the candidates track to the nearest neighbouring track 44
3.13 The absolute difference of the inverse p_t with respect to the beam and the inverse transverse energy E_t 45
3.14 The $\cos\theta$ distribution of the electron candidates. 45
3.15 The number of r-ϕ measuring segments on muon tracks. 46
3.16 The distribution of the distance of closest approach (DCA) to the vertex for muon candidates. 47
3.17 The distance of closest approach at the vertex divided by its error for muon candidates 47
3.18 The total distance of the events. 49

4.1 A scheme of the energy measurement and the two stages of the calorimeter. 52
4.2 The energy deposit of muons in the BGO and in the hadron calorimeter. 53
4.3 The ratio E9/E25 of the electron clusters 54
4.4 The number of crystals in an electromagnetic shower. 54
4.5 The ratio E9/E25 of clusters due to incoming hadrons. 56
4.6 The number of crystals for each cluster of incoming hadrons. . . . 56
4.7 The raw energy deposit for each cluster of incoming hadrons. . . . 57
4.8 Low energy noise in the BGO 58
4.9 The average energy of the 8 crystals surrounding the most energetic crystal. 59
4.10 The ratio of the energy in the central crystal over the energy in the 9 central crystals versus the energy in the central crystal. . . . 60
4.11 The energy weighted clusters in cosine of the polar angle θ. 61
4.12 The visible energy spectrum for each jet in the two jet sample . . 61
4.13 The resolution in the BGO and the muon chamber for electron and muons respectively. 63
4.14 The visible energy spectrum of the whole event. 65
4.15 Comparison of the generated missing energy spectrum, with gaussian smeared one and the reconstructed spectrum for tagged b $\rightarrow$ eνX candidates. 65
4.16 The visible energy spectrum of the b-enriched samples 67
4.17 The visible energy spectrum of the b-depleted samples 68

5.1 The spectrum of $p_\perp$ with respect to the jet direction for the electron candidates in different samples 73

5.2 The $\cos\Theta$ distribution of the electron candidates. 74
5.3 The ϕ distribution of the electron candidates. 75
5.4 The momentum spectrum of the electron sample in two $p_{\perp}$ ranges corresponding to the final sample. 76
5.5 The spectrum of $p_{\perp}$ with respect to the jet direction for the muon candidates in different samples 78
5.6 The description of the muon acceptance by the Monte Carlo . . . 80
5.7 The momentum spectrum of the final muon sample in two $p_{\perp}$ ranges 81
5.8 The mass of the "fat" jet. 83
5.9 a) The electron neutrino spectrum compared with V–A×V–A and the V+A×V–A prediction. b) The same for the muon neutrino. . 88
5.10 The hadronic background estimate 89
5.11 The final fitted distribution compared with the data. The neutrino content corresponds to the fitted branching ratio. 91
5.12 The final fitted distribution compared with the data and the τ neutrino content corresponding to the fitted branching ratio. . . . 93

6.1 The result for the determination of $|V_{cb}|$ and $|V_{ub}|$. 99
6.2 Comparison of the ratio of Br(b $\rightarrow \tau\nu$X) and Br(b $\rightarrow$ eνX) from this analysis with theory. 102

A.1 The mean residuals of the last wire of all outer TEC sectors as a function of drifttime, before the calibration process. 108
A.2 The mean residuals per wire, integrated over all sectors as a function of drifttime for some average wires, before the calibration process 109
A.3 The mean residuals of the last wire of all outer TEC sectors versus drifttime, after the calibration process. 110
A.4 The mean residuals per wire, integrated over all sectors as a function of drifttime for some average wires, after the calibration process 111
A.5 The resolution for transverse momentum with respect to the muon chamber measurement and the DCA resolution measured with Z $\rightarrow$ e^+e^- events. 112
A.6 The transverse momentum and DCA resolution as a function of local ϕ of an inner sector 113

List of Tables

1.1 The three generations of particles in the Standard Model. 3
1.2 The interaction particles 4
1.3 Comparison of measurements of electroweak parameters with theory. 6
1.4 Mean b-hadron lifetimes measured at LEP 12
1.5 Comparison of branching ratio measurements at ICHEP94. 12

2.1 The different data formats used. 31

4.1 The average energy per jet and $\cos\theta$ for data and Monte Carlo after the calibration process. 62
4.2 The result of mean energy obtained by the Gaussian fits between 40 and 65 GeV for the different samples in data and Monte Carlo. 66

5.1 Ratio Data vs. MC showing the $p_\perp$ dependency of the number of electron candidates for the different subsamples. 72
5.2 The observed number of electron candidates per hadronic event . 72
5.3 Estimated systematic errors for the branching ratio measurement of the high $p_\perp$ electrons. 74
5.4 Ratio of data vs. MC showing the $p_\perp$ dependence of the number of muon candidates for the different subsamples. 77
5.5 Estimated systematic errors for the branching ratio measurement of the high $p_\perp$ muons. 79
5.6 The observed number of muon candidates per hadronic event . . . 79
5.7 The ratios of the fractions of tagged "fat" jets per mass range . . 84
5.8 Observed number of events in the data with high $p_\perp$ electron or muon candidates for $p_\perp > 1.4$GeV and for the different mass bins of the "fat" jet 84
5.9 The measured average neutrino energies $< E_\nu >$ 85
5.10 The dominant contributions to the systematic error for the average charged lepton and neutrino energy measurement. 86
5.11 The observed number of events for different neutrino energy regions 87
5.12 The systematic errors of the semileptonic branching ratio b $\to \nu$X. 91
5.13 The systematic errors of the semileptonic branching ratio b $\to \tau\nu$X. 92

6.1 Summary of the different semileptonic branching ratio measurements. 97

6.2 Values of $|V_{ub}/V_{cb}|$ obtained by ARGUS and CLEO. 98
6.3 Comparison with measurements using the exclusive decay B $\rightarrow$ D$^*\ell\nu$ 100
6.4 The comparison with the other measurements of Br(b $\rightarrow \tau\nu$X). . . 101

Abstract

The excellent calorimetry of the L3 detector lead to the idea to probe the weak charged current in semileptonic b-decays emphasising neutrinos and hence missing energy. For the first time the space-time structure of the current was probed directly. The theoretical predicted V–A×V–A structure was confirmed. An exotic V+A×V–A is excluded by more than 6 standard deviations and a V×V–A structure is disfavoured by 3 standard deviations. The average neutrino energy was measured with a 3% relative precision.

Furthermore the coupling strength was studied by the measurement of semileptonic branching ratios. The semileptonic branching ratio $\mathrm{Br}(\mathrm{b} \to \mathrm{e}\nu\mathrm{X})$ was found to be $(10.89 \pm 0.20 \pm 0.51)\%$, the branching ratio $\mathrm{Br}(\mathrm{b} \to \mu\nu\mathrm{X})$ was found to be $(10.82 \pm 0.15 \pm 0.59)\%$. For the first time an inclusive branching ratio $\mathrm{Br}(\mathrm{b} \to \nu\mathrm{X})$ was measured using a lifetime tagged sample. The branching ratio was found to be $(23.08 \pm 0.77 \pm 1.24)\%$ using combined neutrino spectra with a ratio $1:1:0.25$ for ν_e, ν_μ and ν_τ, respectively. The combined branching ratio assuming $\mathrm{Br}(\mathrm{b} \to \mathrm{e}\nu\mathrm{X}) = \mathrm{Br}(\mathrm{b} \to \mu\nu\mathrm{X})$ yields $(10.68 \pm 0.11 \pm 0.46)\%$, taking also into account the inclusive neutrino branching ratio. With this branching ratio the elements $|V_{cb}|$ and $|V_{ub}|$ of the CKM matrix were extracted, giving $|V_{cb}| = 0.0373 \pm 0.0017$ and $|V_{ub}| = 0.0032 \pm 0.00019$.

The branching ratio $\mathrm{Br}(\mathrm{b} \to \tau\nu\mathrm{X}) = 1.7 \pm 0.5 \pm 1.1\%$ was used to also probe physics beyond the Standard Model. The ratio $\mathrm{Br}(\mathrm{b} \to \tau\nu\mathrm{X})/\mathrm{Br}(\mathrm{b} \to \mathrm{e}\nu\mathrm{X}) = 0.15 \pm 0.04 \pm 0.07$, obtained from this measurement, should be enhanced if there would be a charged current mediated by a charged Higgs boson. A limit of $r = \tan\beta/m_{H^\pm} < 0.24\mathrm{GeV}^{-1}$ was set, thus restricting the parameter space of minimal supersymmetric models.

Zusammenfassung

Die ausgezeichnete Kalorimetrie des L3 Detektors führte zu der Idee den schwachen geladenen Strom im semileptonischen b-Zerfall mit Neutrinos, und damit fehlender Energie, zu testen. Zum ersten Mal konnte die Raum-Zeit-Struktur des Stroms direkt getestet werden. Die theoretische Vorhersage einer V–A×V–A Struktur wurde bestätigt. Die eher exotische V+A×V–A Struktur wurde mit 6 Standardabweichungen ausgeschloßen. Die V×V–A Struktur wurde mit nur 3 Standardabweichungen ausgeschloßen. Die mittlere Neutrinoenergie konnte mit einer Präzision von 3% relativ gemessen werden.

Weiterhin wurde die Kopplungsstärke mit der Messung von semileptonischen Verzweigungsverhältnissen studiert. Das semileptonische Verzweigungsverhältnis $\mathrm{Br}(\mathrm{b} \to \mathrm{e}\nu\mathrm{X})$ wurde bestimmt als $(10.89 \pm 0.20 \pm 0.51)\%$. Das Verzweigungsverhältnis $\mathrm{Br}(\mathrm{b} \to \mu\nu\mathrm{X})$ wurde gemessen als $(10.82 \pm 0.15 \pm 0.59)\%$. Ebenso wurde erstmalig das Verzweigungsverhältnis $\mathrm{Br}(\mathrm{b} \to \nu\mathrm{X})$ gemessen in Ereignissen, die durch ein Lebensdauersignal selektiert wurden. Das Verzweigungsverhältnis wurde bestimmt als $(23.08 \pm 0.77 \pm 1.24)\%$ unter Benutzung kombinierter Neutrinospektra im Verhältnis $1 : 1 : 0.25$ für ν_e, ν_μ und ν_τ. Das gemeinsame Verzweigungsverhältnis mit der Annahme $\mathrm{Br}(\mathrm{b} \to \mathrm{e}\nu\mathrm{X}) = \mathrm{Br}(\mathrm{b} \to \mu\nu\mathrm{X})$ ergibt $(10.68 \pm 0.11 \pm 0.46)\%$, unter Berücksichtigung des inklusiven Neutrino-Verzweigungsverhältnisses. Mittels dieses Verzweigungsverhältnises sind die Elemente $|V_{cb}|$ und $|V_{ub}|$ der CKM Matrix bestimmt worden. Dies ergab $|V_{cb}| = 0.0373 \pm 0.0017$ und $|V_{ub}| = 0.0032 \pm 0.00019$.

Es wurde eine Messung des Verzweigungsverhältnisses $\mathrm{Br}(\mathrm{b} \to \tau\nu\mathrm{X}) = 1.7 \pm 0.5 \pm 1.1\%$ durchgeführt, um die über das Standardmodell hinausgehende Physik zu testen. Das Verhältnis $\mathrm{Br}(\mathrm{b} \to \tau\nu\mathrm{X})/\mathrm{Br}(\mathrm{b} \to \mathrm{e}\nu\mathrm{X}) = 0.15 \pm 0.04 \pm 0.07$, das in diese Messung bestimmt wurde, sollte erhöht sein, falls es einen geladenen Strom gibt, der durch das geladene Higgs-Boson vermittelt wird. Eine obere Grenze für den Parameter $r = \tan\beta/m_{H^\pm} < 0.24\mathrm{GeV}^{-1}$ wurde bestimmt, um den Paramterraum minimal supersymmetrischer Modelle zu begrenzen.

Introduction

Todays picture of the fundamental elements of matter and the forces between them is based on the existence of two distinct classes of point like particles, fermions and bosons. Fermions build anti-symmetric states under exchange of identical particles and follow therefore Fermi statistics. Bosons build symmetric states under exchange of identical particles and therefore follow the Einstein-Bose statistics. The dynamics or the forces between particles is mediated by the exchange of particles. The elementary building blocks of matter are the quarks and leptons which are fermions, and the particles which can be associated with the forces are the interaction bosons.

The dynamics of the interaction are described by the electroweak theory and the quantum chromo dynamics QCD which together build the Standard Model. A milestone in the development of this model was Glashow [1], Salam [2] and Weinberg's [3] unification of the electromagnetic and weak interaction.

The results of LEP I are a story of success for the Standard Model.LEP and the four experiments L3, ALEPH, OPAL and DELPHI were especially build to probe this model. The electroweak part of the model mediating the neutral current interaction $e^+e^- \to Z \to X$ is the main field of research at LEP I, therefore LEP I operates on the Z resonance. Many parameters of the Standard Model today are tested to a very high precision [4] [5]. Details will be given in the theoretical overview.

In the Standard Model quarks and leptons can be ordered in generations. Each generation contains exactly one neutrino species. The number of different species can be measured by observing the invisible decay width of the Z. This measurement limit this number to three, since the measurement gives 2.989 ± 0.012 [5]. Thus the number of generations is also limited to three, assuming that there is no heavy neutrino with a mass higher than half m_Z. The consequence is that nearly all elementary particles in the Standard Model are known. The famous exception is the Higgs boson. In a second phase LEP will also cover the weak boson interaction, $Z \to W^+W^-$.

A large fraction of Z bosons decays into $b\bar{b}$-quarks and so LEP I with its high luminosity and high Z-production cross-section is also an excellent laboratory to study b-quark physics. Weak decays of the b quark provide the possibility to study the universality of the weak charge current for the third generation of quarks. In the analysis presented here the weak charge current is tested in two respects.

Semileptonic branching ratios give information about the strength of the effective coupling and, by comparing the energy spectra of the charged and neutral leptons, the polarisation and the parity violation of the coupling. The measurement of the branching ratio, hence the decay rate, into leptons and the lifetime provides the partial width of the decay into leptons, and thus a determination of V_{cb}, an element of the Cabbibo-Kobayashi-Maskawa CKM Matrix [6]. This also probes the influence of QCD corrections in the weak decay. The comparison of the branching ratio into charged and neutral leptons also tests the structure of the coupling. Polarisation can be also tested directly by measuring the energy sharing between the charged lepton and neutrinos. These measurements are subject of this thesis.

The first chapter describes the theoretical background. The second chapter describes the experiment, where the discussion is concentrated on the elements which are important for the measurements. The event selection is presented in the third chapter, and the jet-energy calibration which is needed to perform a missing energy measurement is studied in the fourth chapter. The measurements are described in the fifth chapter which is followed by a discussion of the results in chapter six.

Chapter 1

Theoretical overview

A short overview of the Standard Model is given, focusing on the physics of the b-quark, emphasising the aspects of semileptonic b-decays. The consequence of the measurement of $\mathrm{b} \to \tau\nu\mathrm{X}$ for models beyond the Standard Model is discussed, as well.

1.1 A glance at the Standard Model

The general picture of the Standard Model contains three generations of particles, with a SU(2) flavour symmetry as the building blocks of matter shown in table 1.1. They carry weak isospin (I, I_3) and weak hypercharge Y as the main quantum numbers of the electroweak theory. Quarks carry in addition a colour quantum number, as the charge of QCD, the theory of strong interaction. The electric charge Q is given in analogy to the Gell-Mann Nishijima relation [7], where I_3 and Y denotes the weak isospin and the weak hypercharge:

$$Q = I_3 + \frac{Y}{2} \tag{1.1}$$

These elementary particles are fermions and carry spin one half. The interaction happens by the exchange of spin one bosons which are shown in table 1.2. The dynamics is described by a locally gauge invariant field theory. The full theory of the Standard Model is then a $\mathrm{SU(3)_C} \times \mathrm{SU(2)_I} \times \mathrm{U(1)_Y}$ field theory where I denotes the weak isospin, Y the weak hypercharge, and C the colour, the charge of the strong interaction. The last ingredient of the theory is the Higgs mechanism which breaks the $\mathrm{SU(2)_I} \times \mathrm{U(1)_Y}$ symmetry to the observed exact local symmetry

	Generation			Charge
	1.	2.	3.	Q
quarks	u	c	t	$+\frac{2}{3}$
	d	s	b	$-\frac{1}{3}$
leptons	ν_e	ν_μ	ν_τ	0
	e^-	μ^-	τ^-	-1

Table 1.1: The three generations of particles in the Standard Model.

Electromagnetic interaction	γ
Weak interaction	$W^{\pm}$, Z
Strong interaction	8 species of gluons

Table 1.2: The interaction particles

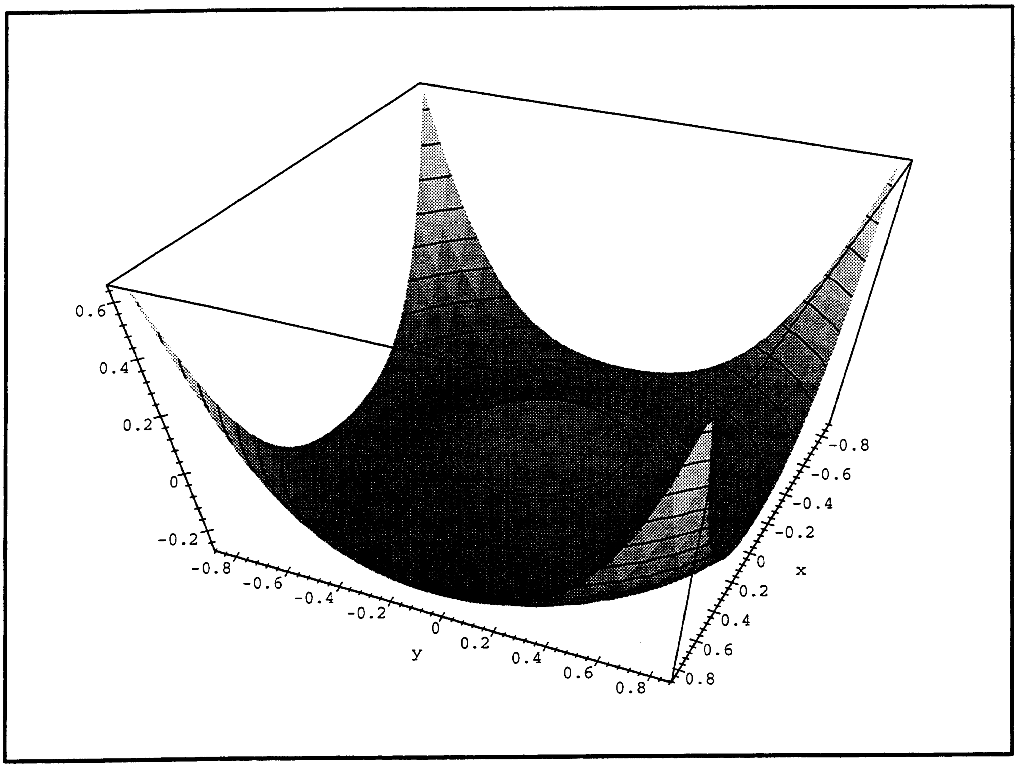

Figure 1.1: A schematic view on the potential of the Higgs field with arbitrary units. The vacuum expectation lies on a circle, but the position can be chosen due to the gauge freedom. At high energies the symmetry is exact.

$U(1)_{em}$. The Higgs mechanism predicts a physical scalar neutral Higgs boson and gives a mass to the bosons providing weak interaction. Thus it explains the short interaction distance of the weak force. The coupling strength of the Higgs to other particles is proportional to their mass. A Higgs potential can be seen in figure 1.1. The vacuum is the minimum of this potential and is degenerate on a circle. The local gauge freedom allows to chose as vacuum any point on that circle. The saddlepoint at (0,0) marks the energy where symmetry breaking begins, for higher energies the potential is symmetric, consequently the symmetry is exact.

The full Lagrangian is composed of:

$$\mathcal{L}_{SM} = \mathcal{L}_{QCD} + \mathcal{L}_{boson} + \mathcal{L}_{I} + \mathcal{L}_{fermion} + \mathcal{L}_{Higgs} \ , \qquad (1.2)$$

where $\mathcal{L}_{QCD}$ is the Lagrangian of all couplings involving gluons including their self interaction, $\mathcal{L}_{boson}$ describes the kinetic term and self interaction of the $W^{\pm}$, Z and γ, $\mathcal{L}_{I}$ represents the lepton and quark interaction with the electroweak gauge bosons, $\mathcal{L}_{fermion}$ are the mass terms and the kinetic energy of the fermions and finally $\mathcal{L}_{Higgs}$ is the interaction of the fermions and the weak gauge bosons with the Higgs field.

The unification of the weak and electromagnetic interactions can be shown by inspecting the interaction term [8], which is

$$\mathcal{L}_I = \bar{\psi}\gamma^\mu \left(-g\frac{\boldsymbol{\tau}}{2}\cdot \mathbf{W}_\mu (1-\gamma_5) - g'\frac{Y}{2}B_\mu\right)\psi \ , \tag{1.3}$$

ψ denotes the fermionic field, $\frac{\tau}{2}$ the charge operator of the weak isospin, with $\mathbf{W}_\mu$ the corresponding gauge field, and $\frac{Y}{2}$ the charge operator of the weak hypercharge, with B_μ the corresponding gauge field, $(1-\gamma_5)$ is the projector for left handed states and generates the V–A structure, g and g' are the coupling strengths. The operators

$$W_\mu^+ = \sqrt{\frac{1}{2}}\left(W_\mu^1 - iW_\mu^2\right) \tag{1.4}$$

$$W_\mu^- = \sqrt{\frac{1}{2}}\left(W_\mu^1 + iW_\mu^2\right) \tag{1.5}$$

describe the charge creation and annihilation operators and can be identified with the W$^\pm$ bosons. The third W-component and B_μ build

$$A_\mu = B_\mu \cos\theta_W + W_\mu^3 \sin\theta_W \tag{1.6}$$

$$Z_\mu = -B_\mu \sin\theta_W + W_\mu^3 \cos\theta_W \tag{1.7}$$

the massless γ and the massive Z boson. θ_W is defined as the Weinberg angle and describes the mixing of the weak and electromagnetic interaction. With this unification the interaction term can be rewritten in terms of the fields $W_\mu^\pm$,Z_μ and A_μ

$$\begin{aligned}\mathcal{L}_I =& \bar{\psi}\gamma^\mu \\ & \{-eQA_\mu \\ & -\frac{e}{\sin\theta_W}\left[\frac{\tau^+}{2}W_\mu^+(1-\gamma_5) + \frac{\tau^-}{2}W_\mu^-(1-\gamma_5)\right] \\ & -\frac{e}{\sin\theta_W\cos\theta_W}\left[\frac{\tau_3}{2}(1-\gamma_5) - \sin^2\theta_W Q\right]Z_\mu\} \\ & \psi \ ,\end{aligned} \tag{1.8}$$

where $\tau^\pm = \frac{1}{\sqrt{2}}(\tau_1 \pm i\tau_2)$ is the weak isospin raising and lowering operator. The Noether currents are the weak charged current

$$J^{\pm\mu} = \bar{\psi}\gamma^\mu\frac{\tau^\pm}{2}(1-\gamma_5)\psi \ , \tag{1.9}$$

the electroweak neutral current

$$J_Z^\mu = \bar{\psi}\gamma^\mu\left[\frac{\tau_3}{2}(1-\gamma_5) - \sin^2\theta_W Q\right]\psi \ , \tag{1.10}$$

and the electromagnetic current

$$J_{em}^\mu = \bar{\psi}\gamma^\mu Q\psi \ . \tag{1.11}$$

Experiment	Parameter	Value	Theory[4]
LEP collaborations [15]	m_Z [GeV]	91.1884 ± 0.0022	input
	Γ_Z [GeV]	$2.4963 \pm 0.0030 \pm 0.0010$	2.4974
	σ_h^0 [nb]	41.488 ± 0.078	41.439
	$\sin^2 \theta_{W_{eff}}^{\ell}$	0.2321 ± 0.0004	0.23199
CDF [16]	m_W [GeV]	80.41 ± 0.18	80.315

Table 1.3: Some electroweak parameters obtained in e^+e^- collisions at the Z peak (LEP) and in $p\bar{p}$ collisions at 1.8TeV (CDF) compared with the theoretical prediction. As can be seen, there is a excellent agreement up to a few permille. m_Z is an input for the theoretical calculation.

Since the discovery of the W [9] [10] and the Z-bosons [11] [12] LEP experiments as well as hadron collisider and neutrino experiments have tested the Standard Model to a high precision, as shown in table 1.3. After the direct observation of the top quark by the CDF collaboration [13] and the D0 collaboration [14]. Only the Higgs particle is missing to complete the Standard Model.

As shown, the fermions are left or right handed which is distinguished by the weak interaction. The reason to order the basic particles from table 1.1 into families lays in the GIM mechanism [17]. This mechanism transposes the observed SU(2) flavour structure seen in the lepton sector into the quark sector, which as a consequence at that time predicted the charm quark and established two generation of particles. It orders the left handed particles into the weak isospin doublets. The weak charged current as seen from equation 1.10 acts as a rising and lowering current between the states of the doublets. To allow the s $\rightarrow$ u transition, the states d and s for the weak interaction must be a mixture of the d and s eigenstates of the mass matrix. Such a mixing does not appear to occur in the lepton sector. The mixing matrix is a simple rotation in flavour space, and the current algebra requires the matrix to be unitary [18].

In the Standard Model this mixing matrix is also responsible for another observed effect, the so called CP-violation. The chirality of the weak interaction clearly violates parity, which exchanges the sign of the fourvector in the particle wavefunction and hence is equivalent to mirroring in spacetime. Until the measurement of Christenson et al. in 1964 [19] in the kaon system, it was believed that the product of the charge conjugation C, which exchanges particles with anti-particles, and the parity P was a conserved discrete symmetry. In the kaon system, assuming a phase convention, the CP operators transform the K^0 $\overline{K^0}$ system of the strong interaction as

$$CP|K^0> = -|\overline{K^0}> \quad . \tag{1.12}$$

Assuming no CP violation, the eigenstates for the weak forces would then be

$$|K_1^0> = \frac{1}{\sqrt{2}}\left[|K^0> -|\overline{K^0}>\right] \qquad (1.13)$$

$$|K_2^0> = \frac{1}{\sqrt{2}}\left[|K^0> +|\overline{K^0}>\right] , \qquad (1.14)$$

where K_1^0 has $CP = +1$ and K_2^0 has $CP = -1$. The $K_1^0K_2^0$ states cannot be identical to the mass eigenstates of the strong interaction $K^0\overline{K^0}$, due to the mixing of d and s quark in the weak eigenstates. The K_1^0 can decay into two pions, but the K_2^0 can only decay into three pions. Due to phase space suppression the first meson decays much faster than the second one. CP-violation can be explained if the decaying states are a combination of K_1^0 and K_2^0 with a small phase, ϵ,

$$|K_S^0> = \frac{1}{\sqrt{1+\epsilon^2}}\left[|K_1^0> -\epsilon|K_2^0>\right] \qquad (1.15)$$

$$|K_L^0> = \frac{1}{\sqrt{1+\epsilon^2}}\left[|K_2^0> +\epsilon|K_1^0>\right] . \qquad (1.16)$$

Even before the discovery of the c-quark and the particles of the third family, Kobayashi and Maskawa [20] discussed possibilities to include CP violation in the GIM framework. In this approach the most natural choice would be to have left handed doublets and right handed singlets. CP violation would occur if there were at least three families. The left handed doublets are:

$$\begin{pmatrix} u \\ d' \end{pmatrix}_l, \begin{pmatrix} c \\ s' \end{pmatrix}_l, \begin{pmatrix} t \\ b' \end{pmatrix}_l, \begin{pmatrix} \nu_e \\ e^- \end{pmatrix}_l, \begin{pmatrix} \nu_\mu \\ \mu^- \end{pmatrix}_l, \begin{pmatrix} \nu_\tau \\ \tau^- \end{pmatrix}_l \qquad (1.17)$$

and the right handed singlets:

$$u_r, d'_r, c_r, s'_r, t_r, b'_r, e_r^-, \mu_r^-, \tau_r^- . \qquad (1.18)$$

The prime denotes that these quarks are eigenstates of the weak interaction. As a consequence the Hamiltonian does not preserve CP and the eigenstates are not CP eigenstates. Neither $|K_L^0>$ nor its dominant component $|K_2^0>$ are pure CP eigenstates. The ϵ mixing of equations 1.15 and 1.16 expresses an indirect CP violation. The fact that the eigenstates of the weak interaction are not CP eigenstates expresses direct CP-violation. Models which consider nearly vanishing direct CP-violation are called superweak [21]. Including the Cabbibo-Kobayashi-Maskawa CKM matrix in the model, the weak charged current can be written as

$$J_\mu^{CC} = l_\mu + h_\mu \qquad (1.19)$$

$$l_\mu = \begin{pmatrix} \bar{\nu}_e & \bar{\nu}_\mu & \bar{\nu}_\tau \end{pmatrix} \gamma_\mu (1-\gamma_5) \begin{pmatrix} e^- \\ \mu^- \\ \tau^- \end{pmatrix} + h.c. \qquad (1.20)$$

$$h_\mu = \begin{pmatrix} \bar{u} & \bar{c} & \bar{t} \end{pmatrix} \gamma_\mu (1-\gamma_5) \mathbf{V} \begin{pmatrix} d \\ s \\ b \end{pmatrix} + h.c. , \qquad (1.21)$$

where $\mathbf{V}$ is the CKM matrix. A representation of this matrix is:

$$\mathbf{V} = \begin{pmatrix} V_{ud} & V_{us} & V_{ub} \\ V_{cd} & V_{cs} & V_{cb} \\ V_{td} & V_{ts} & V_{tb} \end{pmatrix} \tag{1.22}$$

$$= \begin{pmatrix} c_{12}c_{13} & s_{12}c_{13} & s_{13}e^{-i\delta_{13}} \\ -s_{12}c_{23} - c_{12}s_{23}s_{13}e^{-i\delta_{13}} & c_{12}c_{23} - s_{12}s_{23}s_{13}e^{-i\delta_{13}} & s_{23}c_{13} \\ s_{12}s_{23} - c_{12}c_{23}s_{13}e^{-i\delta_{13}} & -c_{12}s_{23} - s_{12}c_{23}s_{13}e^{-i\delta_{13}} & c_{23}c_{13} \end{pmatrix}, \tag{1.23}$$

where the elements V_{ij} are the element connecting the quark i and j; s_{ij} and c_{ij} are the sine and the cosine of the mixing angle between generation i and j; the phase δ is the CP violating phase. The second matrix is one of the possible representations, proposed by the particle data group PDG [22]. This representation has the phenomenological advantage that the angles, which determine the matrix, can be measured by a single physical process. For example $|V_{ub}|$ is given by a single angle θ_{13} and known to be small, so also θ_{23} is directly accessible by the measurement of b $\rightarrow$ c transitions. Another frequent used parameterisation of the CKM matrix is due to Wolfenstein [23]:

$$\mathbf{V} = \begin{pmatrix} 1-\frac{\lambda^2}{2} & \lambda & A\lambda^3(\rho - i\eta) \\ -\lambda & 1-\frac{\lambda^2}{2} & A\lambda^2 \\ A\lambda^3(1-\rho-i\eta) & -A\lambda^2 & 1 \end{pmatrix} \tag{1.24}$$

In contrast to equation (1.23), equation (1.24) is not an exact parameterisation. It is a development around λ, where $\lambda = \sin\theta_C$ is the sine of mixing angle between d and s quark, the so called Cabbibo angle. Terms of the order λ^4 are neglected. Since this representation assumes that the relation between generations are expressed in powers of λ, it is a more intuitive representation. In matrix (1.24) the CP violating phase is η, it only occurs in the elements V_{ub} and V_{td} which are elements of order λ^3, such that the suppression of CP violating effects is visible. To ensure the unitarity of the matrix, from the 9 relations 6 can be represented as triangles, the so called unitarity triangles of the CKM-matrix. For example, the elements containing the b-quark build

$$V_{ud}V_{ub}^* + V_{cd}V_{cb}^* + V_{td}V_{tb}^* = 0\ . \tag{1.25}$$

The current range of experimental values for the $|V_{ij}|$ are [22]:

$$\mathbf{V} = \begin{pmatrix} 0.9747-0.9759 & 0.218-0.224 & 0.002-0.005 \\ 0.218-0.224 & 0.9738-0.9752 & 0.032-0.048 \\ 0.004-0.015 & 0.030-0.048 & 0.9988-0.9995 \end{pmatrix} \tag{1.26}$$

The CKM matrix is important to understand the weak charge hadronic current, since it describes within the framework of the Standard Model, such important effects as the CP-violation in this current and the modification of the effective coupling depending on the flavour.

Semileptonic decays of hadrons are good probes to measure elements $|V_{ij}|$. There are two advantages: the influence of QCD is smaller, since gluons are not exchanged between the leptonic and hadronic system, and only one element of the matrix is involved. In the following analysis the elements $|V_{cb}|$ and $|V_{ub}|$ will be studied using inclusive semileptonic b-hadron decays.

We now turn to the description of the basic decay processes for b-hadrons. In a perturbative approach to quantum field theory processes can be expressed by Feynman graphs. The basic processes involve at maximum two-point functions [24][1], equivalent to one internal line connecting two vertices. They build the Born approximation level. This is also the level where the dominant b-decay processes described below can be understood. The next order in the pertubation series are graphs involving one loop like photon exchange at the vertex. These graphs have divergent terms. These terms can be controlled in a renormalizable theory if a scale for the processes can be fixed. For example, the known electric charge can be used to fix the scale for photon exchange at the vertex. Details can be found in reference [24] and [26]. Loops do not only lead to corrections for the Born level, but they also allow rare processes which are forbidden at Born level. The class of rare b-decays and the phenomenon of $B^0\overline{B^0}$ mixing are due to loop graphs.

Since the b quark decays inside a hadron, Feynman graphs for the decay of B-mesons are shown in figure 1.2. In the simplest model, the other quark is not involved in the decay process, and is a so called spectator. For baryons a second spectator quark has to be added. Figure 1.2a) shows the external spectator graph which is the decay mode for most of the B-mesons. The external spectator graph with a $b \rightarrow u$ decay is also shown in figure 1.2a) and measured for example in the endpoint of the spectrum of $b \rightarrow e\nu X$. Figure 1.2b) shows the internal spectator graph. The suppression of this mode can be seen for example in the branching ratio of $B^0 \rightarrow J/\psi K^0$ of $(7.5 \pm 2.1) \times 10^{-4}$ compared with $B^0 \rightarrow D^- D_s^+$ of $(8 \pm 4) \times 10^{-3}$. As examples for rare decays, figure 1.2c) and 1.2d) show the so called penguin graphs for $b \rightarrow d\gamma$ and $b \rightarrow s\gamma$, which are possible due to a loop.

The consequence of the processes involving loops, like the penguin graphs in figure 1.2c) and 1.2d) or the $B^0\overline{B^0}$ mixing shown in figure 1.2g) and 1.2h), is that the elements $|V_{tx}|$ involving the t-quark (x = d, s or b) are measurable below the threshold of t production. For example, the recent measurement of the CLEO collaboration [27] of the branching ratio of $b \rightarrow s\gamma$ of $(2.32 \pm 057 \pm 0.35) \times 10^{-4}$ allows to determine $|V_{ts}|$. Two elements are involved and not only top quarks, also charm and up quarks can contribute to the loop, as shown in figure 1.2d). Since the diagrams involving charm and up quarks are calculable using present measurements of the corresponding CKM matrix elements, and $|V_{tb}|$ should be close to one as seen in representation 1.24, $|V_{ts}|$ can nevertheless be determined.

The element V_{td}, which is studied in the measurement of the mixing rates, see figure 1.2g) and 1.2h), also includes a CP-violating phase. This is expressed in matrix 1.24. Therefore the last important field which is covered by b-physics is the CP-violation present in the B^0 $\overline{B^0}$ system. There the effect is predicted to be stronger then in the kaon system. It will be studied in dedicated experiments like at HERA-B or in dedicated facilities like asymmetric e^+e^- b-factories and later at LHC.

[1]The connection between stochastic models and quantum field theory is, from the viewpoint of stochastic models, described in [25].

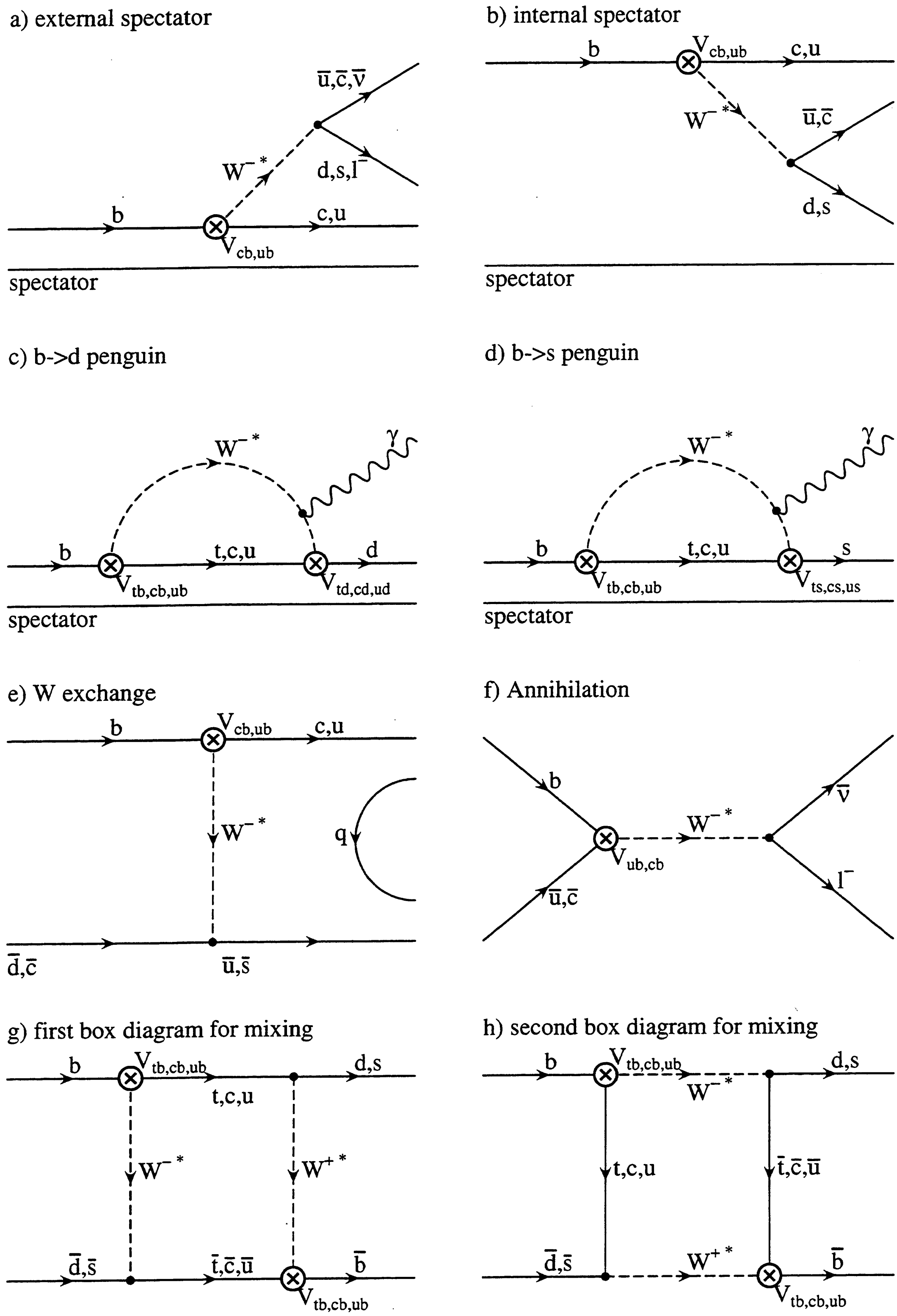

Figure 1.2: Feynman graphs showing the different decay modes of B-mesons.

1.2 What can be learned from semileptonic B-decays?

The b-quark decays inside a hadron after the hadronization process. A question is whether or not the b-quark decays as an independent parton as described in the spectator model. This is equivalent to the question how large QCD corrections are to the weak decay of the b-hadron. QCD corrections to quark decay are either calculated on the lattice or very successfully in the last years in heavy quark effective theory (HQET). In this theory the heavy quark nearly has the full momentum of the hadron, so that effects from the movement of the heavy quark inside the hadron can be neglected [28]. Therefore HQET is similar to a free quark model with corrections which enables the direct calculation of inclusive decay rates.

Several models exist which predict the dynamics of exclusive semileptonic b-hadron decays. The ACCMM [29] model is based on the parton model. The light quark is treated as stable partner during the decay process of the heavy one. Corrections from soft gluon exchange are added. The ISGW [30] model uses a constituent quark model containing valence and sea quarks. Relativistic extensions to these models are the KS model [31], which is an extension to the ACCMM model, and the WSB [32] model which extents the ISGW model. In all models QCD corrections are applied to the b-decay and different charged lepton spectra are predicted. In the ACCMM the difference to uncorrected spectra is only large at the endpoint of the spectra. Therefore it is often referenced as a free quark model. Since only part of the lepton spectra are measured due to experimental limitations, the efficiency for the lepton identification is determined by extrapolating part of the momentum spectrum. This is the reason why decay models are important for branching ratio measurements.

If the formfactors coming from QCD are known, then the partial width

$$\Gamma(\mathrm{b} \to \ell\nu\mathrm{X}) = \frac{\mathrm{Br}(\mathrm{b} \to \ell\nu\mathrm{X})}{\tau_{\mathrm{b}}} = \frac{G_F^2 m_{\mathrm{b}}^5}{192\pi^3}(f_c|V_{cb}|^2 + f_u|V_{ub}|^2) \tag{1.27}$$

relates the branching ratio (Br) to the elements of the CKM matrix, assuming universality of the weak charged current of the Standard Model. The coefficients f_c and f_u absorb the phase space constraints and the QCD corrections. The lifetime of the b-quark together with the semileptonic branching ratio defines a circle in the $|V_{cb}|$, $|V_{ub}|$ parameter space. In recent years the lifetime of b-hadrons has been measured to a good precision, see for example the results measured recently at LEP for the inclusive average lifetime in table 1.4.

The semileptonic branching ratio suffers, however, from an unresolved discrepancy between measurements at the threshold of $\Upsilon(4S)$ production and the LEP experiments operating at the Z pole [37] as shown in table 1.5.

The weak charged current distinguishes between left and right handed particles as described previously. The question is, whether the hadronic current couples in the same way as the leptonic current, and has a V–A structure at the vertex where the current couples to the W*. Another possibility is that a b-hadron decays as

Experiment	Result [ps]
ALEPH [33]	$1.533 \pm 0.013 \pm 0.022$
L3 [34]	$1.535 \pm 0.035 \pm 0.028$
DELPHI [35]	$1.575 \pm 0.010 \pm 0.026$
OPAL [36]	$1.523 \pm 0.034 \pm 0.038$

Table 1.4: Mean b-hadron lifetimes measured at LEP

	Experiment	$\mathrm{Br}(b \to \ell^{\pm}\nu X)$ [%]
$\Upsilon(4S)$	CRYSTALL BALL	$12.0 \pm 0.5 \pm 0.7$
	CUSB	$10.0 \pm 0.4 \pm 0.3$
	ARGUS	$10.2 \pm 0.5 \pm 0.2$
	CLEO	$10.5 \pm 0.2 \pm 0.4$
	CLEO	$10.48 \pm 0.07 \pm 0.33$
	ARGUS	$9.7 \pm 0.5 \pm 0.4$
	CLEO	$10.36 \pm 0.17 \pm 0.40$
$\Upsilon(4S)$	Average	$10.31 \pm 0.10 \pm 0.25$
Z	L3	$11.73 \pm 0.48 \pm 0.28 \pm 0.31$
	OPAL	$10.5 \pm 0.6 \pm 0.4 \pm 0.4$
	ALEPH	$11.40 \pm 0.33 \pm 0.37 \pm 0.20$
	DELPHI	$11.41 \pm 0.45 \pm 0.50 \pm 0.31$
Z	Average	$11.33 \pm 0.22 \pm 0.41$

Table 1.5: Measurements at the Z energy and the at the $\Upsilon(4S)$ energy as shown by R.Patterson [37] at ICHEP94 in Glasgow. The last two numbers from CLEO and ARGUS are model-independent, all other $\Upsilon(4S)$ results use the ACCMM model. The numbers at the Z energy are extracted with the ACCMM model where the third error indicates the model dependency.

a whole, which means the gluon exchange which binds the hadron together and also modifie the vertex destroys the polarisation of the virtual W, as seen in kaon decay. If the quark is heavier, the influence of the light partner and the gluon exchange between them should be less important, which is the assumption of HQET. This means that the polarisation effects should be stronger in b-hadron decays than in those of lighter flavours. Under the assumption that the coupling of the leptons and the W-propagator has the usual V–A structure, three cases for the quarks can be distinguished, V–A×V–A, V+A×V–A (figure 1.3), and the kaon like V×V–A (figure 1.4). Already in a paper from Altarelli et al. [29] in 1982 the possibility of an exotic V+A coupling is mentioned and in the work of Gronau and Wakaizumi [38] a first possibility to test this chirality is discussed.

The average polarisation of the virtual W can be seen in the energy sharing between the charged lepton and its neutrino, as shown in the lepton energy spectra in figure 1.5. In the $V-A \times V-A$ case, the neutrino spectrum is softer than the charged lepton spectrum, in the $V+A \times V-A$ the opposite is true. In the $V \times V-A$ case both leptons have the same spectrum, slightly softer than the charged lepton spectrum in the $V-A \times V-A$ case. If the charged lepton spectrum

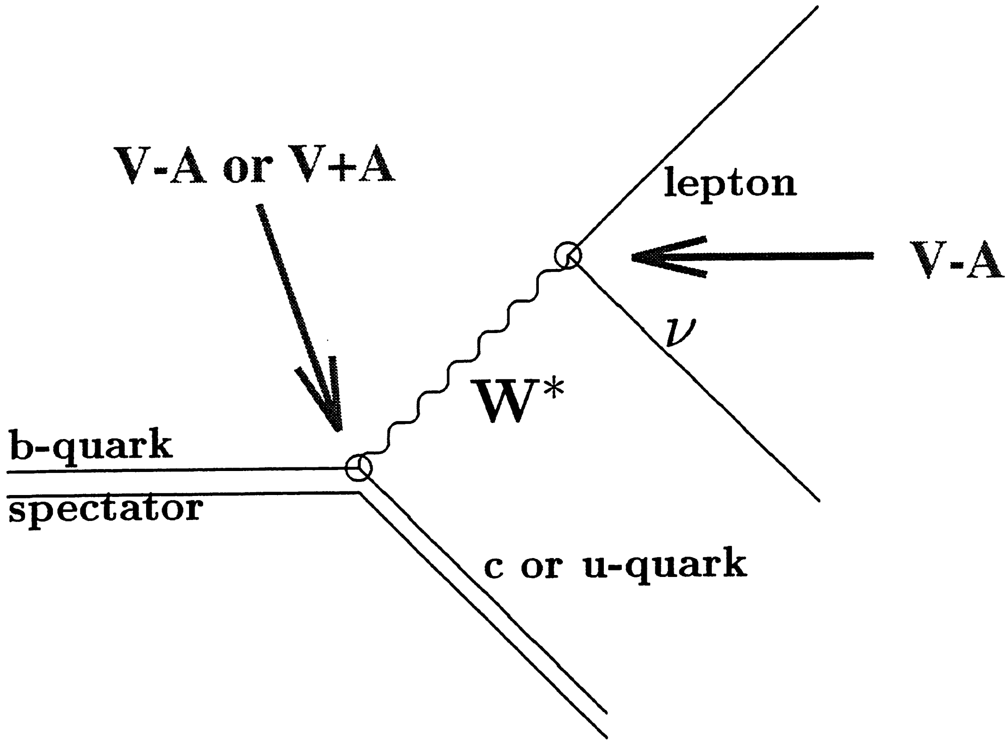

Figure 1.3: The semileptonic b-decay in the spectator model with polarisation at the b-decay vertex.

is only determined by the vertex structure, it would be sufficient to compare it with the predictions for the different models. There are however uncertainties from the branching ratios, the b-quark and c-quark masses, and also, as will be discussed later, in the fragmentation function. As a result, it is possible to adjust parameters, like the one for the fragmentation function, such that the spectrum for the charged lepton appears identical even for the two extreme assumptions, the $\mathrm{V-A\times V-A}$ and $\mathrm{V+A\times V-A}$ case, as seen in figure 1.6. However, it is impossible to make the neutrino spectrum for the different assumptions agree [39], as shown in the spectra of figure 1.6.

The difference in the mean neutrino energy for the two extreme assumptions would be 1.7GeV, which is obtained assuming typical values for energy, fragmentation and branching ratios for a measurement at the Z pole. After applying typical charged lepton selection criteria, a difference of about 1.1GeV remains [39]. Neutrinos in the L3 experiment are seen indirectly by a missing energy signal. The missing energy spectrum gives the neutrino spectrum.

Besides this possibility of a direct measurement of the polarisation, the difference would be also seen in a different apparent branching ratio obtained for neutrinos using the missing energy signal, compared with those for charged leptons. Under the assumption that nature has chosen a $\mathrm{V+A\times V-A}$ structure and the efficiency is obtained from Monte Carlo using V–A×V–A assumption, the Monte Carlo energy spectrum of the neutrinos would be too soft. Since the background is higher for soft neutrinos, the efficiency to tag a neutrino is underestimated by

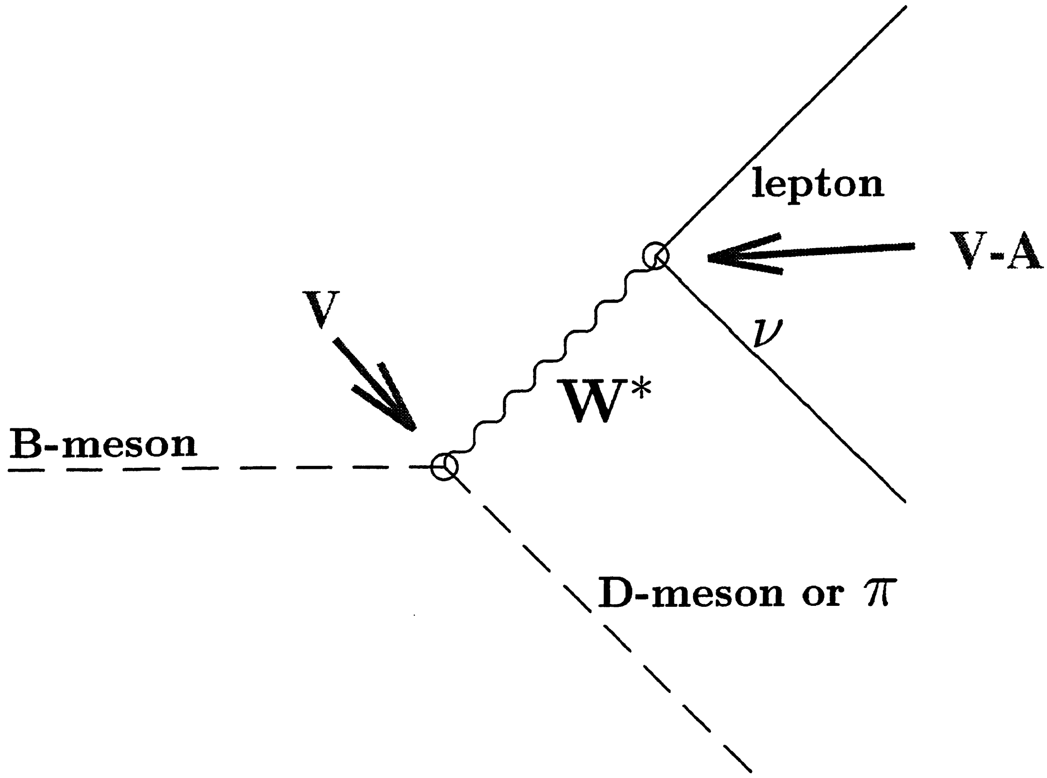

Figure 1.4: The semileptonic b-hadron decay with no polarisation at the hadron decay vertex.

the extrapolation with the Monte Carlo spectrum. This results in a much higher branching ratio than in the case of the charged lepton. So a consistent branching ratio measurement for neutrinos and charged leptons confirms the assumed polarisation of the Monte Carlo, while a discrepancy could hint towards a wrongly assumed polarization.

To summarise, measuring semileptonic branching ratios gives information about the CKM-matrix and therefore about the effective coupling. Using neutrinos as well as charged leptons, the polarisation of the weak charged current can be probed.

1.3 Hadronization

When Z decays to a quark anti-quark pair including possible gluon radiation $Z \to q\bar{q}(g)$, coloured objects are produced. Due to strong coupling the colour field interacts with such an object in a very short time in the order of $10^{-23}s$. As a consequence, the objects interacting with macroscopic matter are hadrons which are colour singlets. The process which leads to these hadrons is called hadronization. The weak decay processes have a longer time scale which is proportional to $\frac{1}{m^5 \cdot |V|^2}$, where m is the mass of the decaying particle and V the CKM matrix element involved. Before the b-quark decays, a hadron is therefore produced by the process of hadronization. This is only different for the top quark, since it is so heavy. The t quark decays before the strong interaction can create

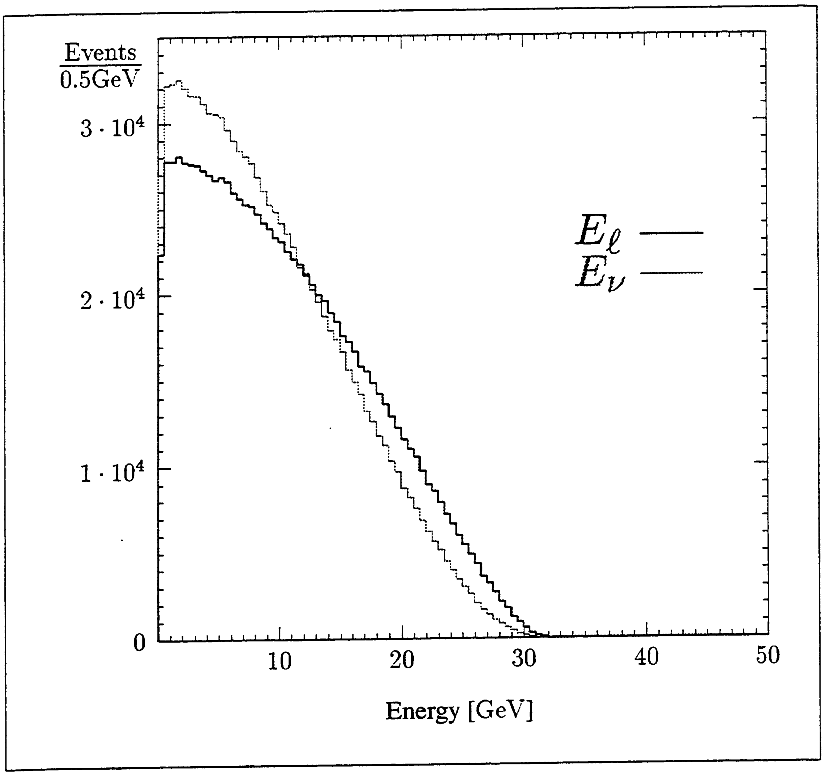

Figure 1.5: The energy spectrum of leptons and neutrinos with V-A×V-A coupling for a given b-hadron energy.

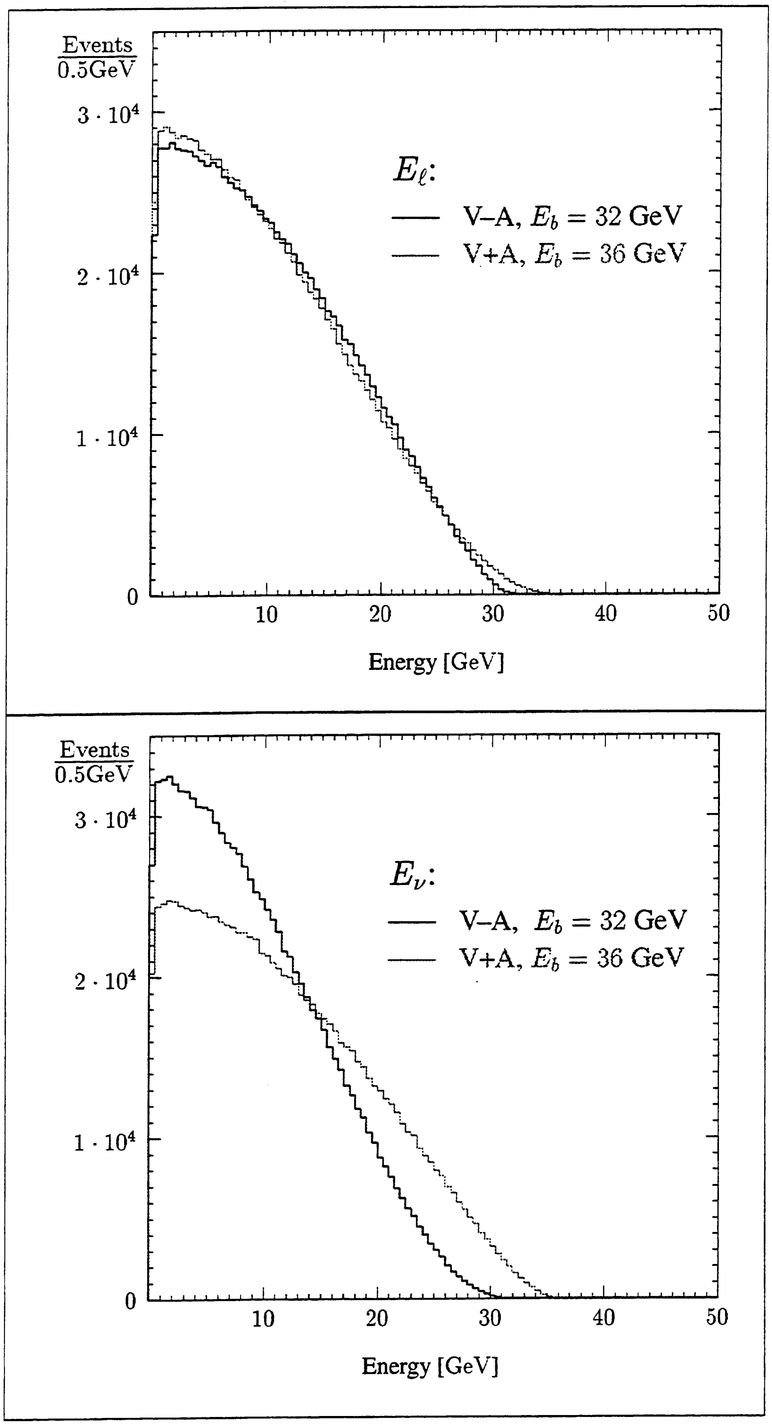

Figure 1.6: The upper plot shows the charged lepton spectrum for a given energy of the b-hadron for different polarisation of the virtual W, adjusted such that the spectra agree. The lower plot shows the corresponding neutrino spectrum, where a clear distinction is seen.

a hadron.

In the hadronization process one can distinguish between hard processes, like gluon bremsstrahlung of quarks and gluon splitting which still are calculable by a pertubative theory, and fragmentation of the quarks into hadrons. The fragmentation processes are soft processes where QCD perturbation theory is not applicable due to the strong coupling.

The only way to perform a full QCD calculation is lattice QCD, where the lattice does the regularization [40]. The problem is the extrapolation to the continuum limit which is a small effect only if the lattice has a very fine spacing. The limited computer resources however lead to lattice spacings which give non negligible theoretical uncertainties on the results. Therefore QCD predictions in the soft regime are done either by lattice calculations or effective models for the given problem. Concerning the fragmentation problem only effective models exist.

In the pertubative regime a shower evolves consisting of quarks generating gluon bremsstrahlung and gluons splitting up into gluon-gluon or quark anti-quark pairs. This evolution is described by the Altarelli-Parisi equations [41]. In the non pertubative regime where the real formation of hadrons begins, different models are used. The two widely used models in analysis performed at LEP are the string fragmentation model and the cluster fragmentation model.

The string fragmentation model stretches colourless strings between partons. Hadrons appear when the strings breaks which happens due to the colour potential between partons. This approach is used by the JETSET [42] [43] Monte Carlo program.

The other approach splits every gluon into quark anti-quark pairs at the end of the parton shower evolution. The quarks are grouped into colourless clusters. The clusters decay into known resonances according to the phase space and spin degeneracy. This ansatz is used by the HERWIG [44] [45] Monte Carlo.

At the end of the hadronization process the known resonances are found. The primary quark, which was produced for example in the neutral current interaction is now part of a hadron. The fragmentation function is the probability density function for the fraction of the primary quark energy, which the hadron containing the primary quark has after its formation. In the heavy quark fragmentation one often uses the Peterson-function [46]

$$f(z) = \frac{1}{z(1 - \frac{1}{z} - \frac{\epsilon}{1-z})^2}\,, \tag{1.28}$$

where z is

$$z = \frac{(E - p_l)_{hadron}}{(E - p_l)_{quark}} \tag{1.29}$$

the ratio of the hadron's energy in the direction of flight of the primary quark to the energy of the primary quark after hard gluon radiation in the same direction. A possible shape of this fragmentation function is shown in figure 1.7.

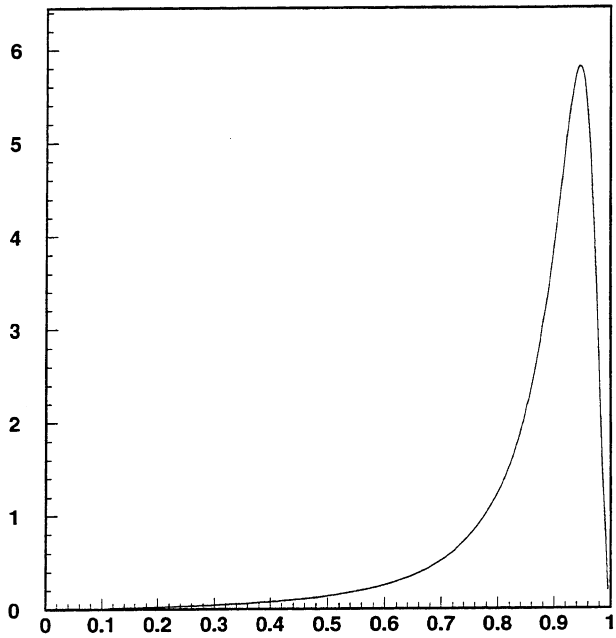

Figure 1.7: The normalised Peterson function for a typical value $\epsilon = 0.003$ used for b-quark fragmentation.

1.4 Consequences for models beyond the Standard Model

The origin of quark mixing is still a mystery of the Standard Model and the related direct CP-violation is still not confirmed. Also the Higgs particle has not yet been found. In particular the Standard Model does not appeal as a complete theory of everything, because:

- It does not include gravitation.
- The so called gauge problem, which means the existence of three different gauge groups with independent couplings [2].
- The model has the so called fermion problem containing for example the hierarchy found in the masses of the fermions. On the other hand the question why there are only three generations, as measured at LEP [15] [3], remains unanswered. Also the apparent absence of a CKM equivalent mixing in the lepton sector adds to this list.
- The quantisation of the electric charge or the weak hypercharge is also problematic. If the weak hypercharge of the Higgs boson (Y_ϕ) is +1, the

[2] Another way to express that would be the arbitrariness of $\sin\theta_W$.

[3] Assuming that the fourth generation neutrinos is light $m_\nu < \frac{m_Z}{2}$.

charge quantization is given by the requirement of gauge anomaly cancellation [47]. But the weak hypercharge of the Higgs boson is arbitrary, if the weak hypercharge of the fermions are expressed in terms of Y_ϕ [48].

Several ansätze were made to go beyond the Standard Model and to overcome some of its weaknesses. Among these are

- grand unification models which in principle simply extend the gauge group and unify couplings at high scales,
- the left right models which especially address CP-violation,
- technicolor which introduces another hidden symmetry,
- supersymmetric models, the most favourite extensions in the recent years,
- and superstrings, which include gravity and supersymmetry.

Most of the models extent also the Higgs sector of the Standard Model. Since all the additional symmetries are not present at the weak energy scale, they have to be broken by some mechanism. Only the minimal supersymmetric model will be studied in more detail here. However, the consequences discussed below will also be true for other models which introduce additional Higgs bosons due to symmetry breaking.

A short description of the term supersymmetry should be given. Supersymmetry defines an equal number of bosonic and fermionic particles in the same multiplet. In the case where there are two pairs of creation and annihilation operators $(a, a^\dagger)$ and $(b, b^\dagger)$ with a being bosonic and b being fermionic, which means

$$[a, a^\dagger] = \{b, b^\dagger\} = 1 \ . \tag{1.30}$$

The general Hamiltonian is

$$H = \omega_a a^\dagger a + \omega_b b^\dagger b \tag{1.31}$$

and with the fermionic operator

$$Q = b^\dagger a + a^\dagger b \tag{1.32}$$

one gets

$$[Q, a^\dagger] = b^\dagger \quad , \quad \{Q, b^\dagger\} = a^\dagger \ . \tag{1.33}$$

So acting with Q on a bosonic state one gets a fermionic one and vice versa. The commutation relation with the Hamiltonian is

$$[Q, H] = (\omega_a - \omega_b)Q \tag{1.34}$$

and for $\omega_a = \omega_b$ the system is supersymmetric and the relation

$$\{Q, Q^\dagger\} = \frac{2}{\omega}H \tag{1.35}$$

is obtained, which means that the algebra closes under anticommutation. This is the definition of supersymmetry. The construction of a field theory from this principle can be found for example in [49]. The consequence is that all known fermions and bosons must have supersymmetric partners which have the opposite statistics. In the minimal supersymmetric model [50] those partners do not decay only to known matter. This is expressed by R-parity conservation, where R-parity is defined as

$$R = (-1)^{3B+L+2S} \tag{1.36}$$

with B the baryon, L the lepton and S the spin quantum number. The known matter has $R = 1$ and the supersymmetric partners have $R = -1$.

Important in the framework of semileptonic b-decays is the fact that the minimal model contains two Higgs doublets which contain two charged Higgs bosons. So there exists a charged current via charged Higgs exchange and this current couples stronger to heavier particles. Consequently the branching ratio of b $\to \tau\nu$X is enhanced relatively to the branching in b $\to$ e(μ)νX [51] from around 0.25 in the Standard Model up to 1.0. The effective Lagrangian for the decay b $\to \tau\nu\mathrm{X_c}$, where $\mathrm{X_c}$ indicates a b $\to$ c transition final state, in this model is [51]

$$\begin{aligned} \mathcal{L} = -V_{cb}\frac{4G_F}{\sqrt{2}}[(\bar{\mathrm{c}}\gamma^\mu(1-\gamma_5)\mathrm{b})\,(\bar{\tau}\gamma_\mu(1-\gamma_5)\nu_\tau) \\ - r^2 m_\tau m_b^Y\,(\bar{\mathrm{c}}(1+\gamma_5)\mathrm{b})\,(\bar{\tau}(1-\gamma_5)\nu_\tau)] \end{aligned} \tag{1.37}$$

with

$$r = \frac{\tan\beta}{m_{H^\pm}} \,. \tag{1.38}$$

The ratio of the vacuum expectation value of the two Higgs doublets is $\tan\beta$. The first term is the Standard Model charged current interaction between the b-c current and the ν_τ-τ current. The second term is the extra contribution from the supersymmetric extension of the Standard Model. Terms proportional m_c^Y are neglected. The Y indicates the running mass of the quarks. The total rate summed over all τ polarisations with this ansatz is

$$\Gamma = \frac{|V_{cb}|^2 G_F^2 m_b^5}{192\pi^3}\left[\Gamma_W + \frac{1}{4}r^4 m_\tau^2 m_b^{Y2}\Gamma_H - 2\mathrm{Re}(r^2 m_\tau m_b^Y)\frac{m_\tau}{m_b}\Gamma_I\right] , \tag{1.39}$$

where Γ_W is the Standard Model W mediated part, Γ_H the charged Higgs mediated part and the Γ_I term represents the interference term. In [51] the terms Γ_H and Γ_I are calculated in terms of Γ_W, $\frac{m_\tau^2}{m_b^2}$, $\frac{m_c^2}{m_b^2}$ and $\frac{2E_\tau}{m_b}$. Assuming that the masses are known, the measurement of partial width thus determines the parameter r.

Consequently a measurement of the branching ratio b $\to \tau\nu$X restricts the parameter space of supersymmetric models and other models with an extended Higgs sector.

Chapter 2

Experimental Apparatus

Experiments on such a big scale as those at LEP are like a set of experiments sharing the same hardware. The hardware of the L3 experiment relevant for this analysis will be described. These are the tracking device and the muon system for event selection and particle identification, the calorimeters for the jet-energy and hence the missing energy measurement. The whole hardware chain starts with the accelerator and ends with the computing resources needed to perform the analysis.

2.1 The accelerator

CERN's Large-Electron-Positron-Collider LEP is an e^+e^--collider located in the Geneva area. The machine is a synchrotron accelarator and storage ring with a circumference of 27 km, shown in figure 2.1, and is between 50 m and 150 m under ground. The machine consists of eight straight and eight curved sections, with the experiments located in straight sections.

In the LEP I phase the machine provided beams up to 55GeV energy per lepton and was operated most of the time on the peak value of the Z resonance at 45.625GeV. Electrons and positrons are injected into LEP with 20GeV energy. The accelerator chain, shown in figure 2.2, consists of the LEP Injector Linac (LIL) linear accelerator producing 600 MeV beams. Then the beam currents are accumulated in the Electron Positron Accumulator (EPA) which afterwards hands them over to the Proton Synchrotron (PS). At the PS the beams get accelerated up to 3.5GeV and are then injected into the Super Proton Synchrotron (SPS). The SPS accelerates then the beams to 20GeV.

Each beam is built from 4 or 8 bunches[1] of electrons or positrons. Each bunch contains approximatively 10^{10} leptons giving a total current from 200 to 300 μA per bunch. The beam spread at the interaction points is roughly 20 μm in the direction normal to the ring and 150 μm in the radial direction. With these parameters a luminosity up to $23.1 \cdot 10^{30}$ cm^{-2}s^{-1} until the end of 1994 could be obtained [52]. The bunches can collide at eight points. At four collision points the experiments L3, ALEPH, OPAL and DELPHI are situated, at the other points electrostatic separators are placed.

[1] In the 1995 running period a bunch train scheme has been implemented, dividing a bunch in up to 4 bunchlets, to increase the luminosity.

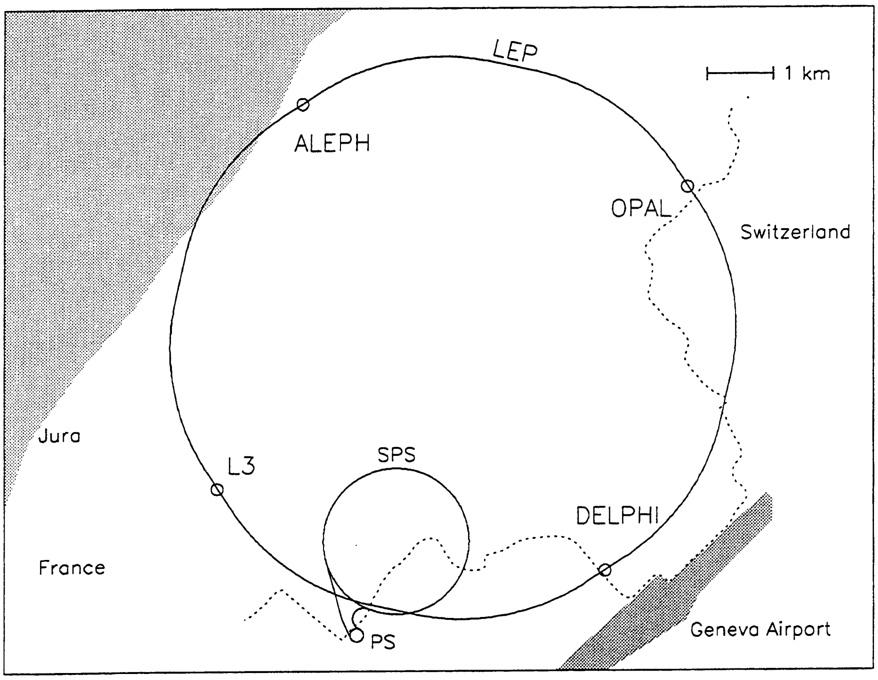

Figure 2.1: The location of the LEP ring and its four experiments.

The machine performed excellently and delivered an integrated luminosity of 159,69 pb^{-1} until the end of 1994 [52]. In the LEP II phase the machine will be able to deliver up to 192GeV center of mass energy, which will enable physicists to see the three boson coupling of a Z with a $W^{\pm}$ pair directly. Also it will substantially extend the mass range for the search of new particles, in particular supersymmetric particles.

2.2 The detector

The measurements presented in the following are performed with the L3 detector. A complete description of this detector is given in [53]. The L3 detector emphasises in its design the measurement of electrons, photons and muons with a very high precision. Also jets are measured with an excellent energy resolution. As all modern collider experiments L3 is made of several subdetectors which are ordered cylindrically around the beampipe, the so called barrel detector elements. It starts with a central tracker, surrounded by an electromagnetic and hadronic calorimeter and the outer most layer is a large volume muon chamber system. To cover the whole solid angle, so called endcap detectors are installed in the forward and backward direction. All detectors are embedded in a solenoid magnetic field of 0.5T. The magnet has an inside radius of 5.93 m and a total length of 11.9 m. The whole detector has a size of roughly 14 m length and 12 m diameter, an overview is given in figure 2.3.

The parts of the detector which are specially relevant in this analysis are described

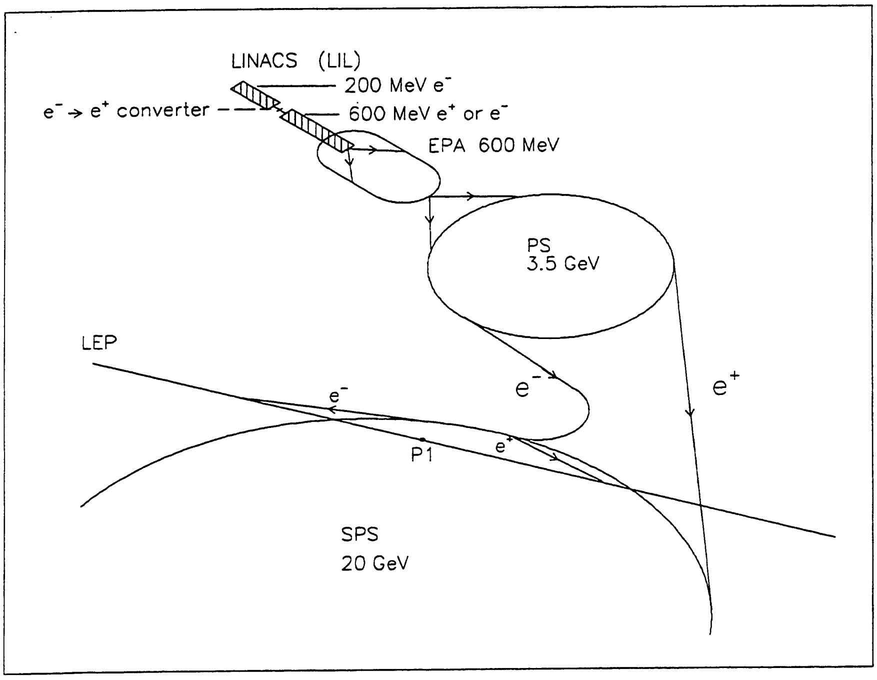

Figure 2.2: The LEP injector chain.

below. Besides these there are other components like the scintillator detector for triggering purposes and the luminosity monitor.

The coordinate system of L3, which is used throughout this analysis, is either cartesian or polar. In the cartesian system the z axis goes along the beampipe, the y axis goes upwards transverse to the plane of the LEP ring and the x axis points towards the center of LEP. The polar system defines r and ϕ as the radial distance and the azimuth angle in the transverse plane with respect to the beam axis and θ as the polar angle with respect to the e-beam axis.

2.2.1 The tracking system

The actual setup consists of a silicon microvertex detector SMD, and a time expansion chamber TEC. Mounted on the TEC is a cathode strip chamber to measure the z coordinate. In forward and backward direction along the beampipe at the end of the TEC is also a forward tracking chamber FTC. The setup used until 1992 is shown in figure 2.4.

The TEC is the heart of the tracking system. Its size is roughly 1 m in length and 1 m in diameter, with a lever arm for the momentum measurement of a track of 31.7 cm. It is made out of two electrically divided parts, the inner TEC and the outer TEC. The outer TEC consists of 24 and the inner TEC of 12 sectors. A sector consists of anode wires spanned in z direction, two grids left and right from the anode, and at the edge of each sector a plane of cathode wires, also spanned in z direction. The space between the anode and one of the two cathodes of a

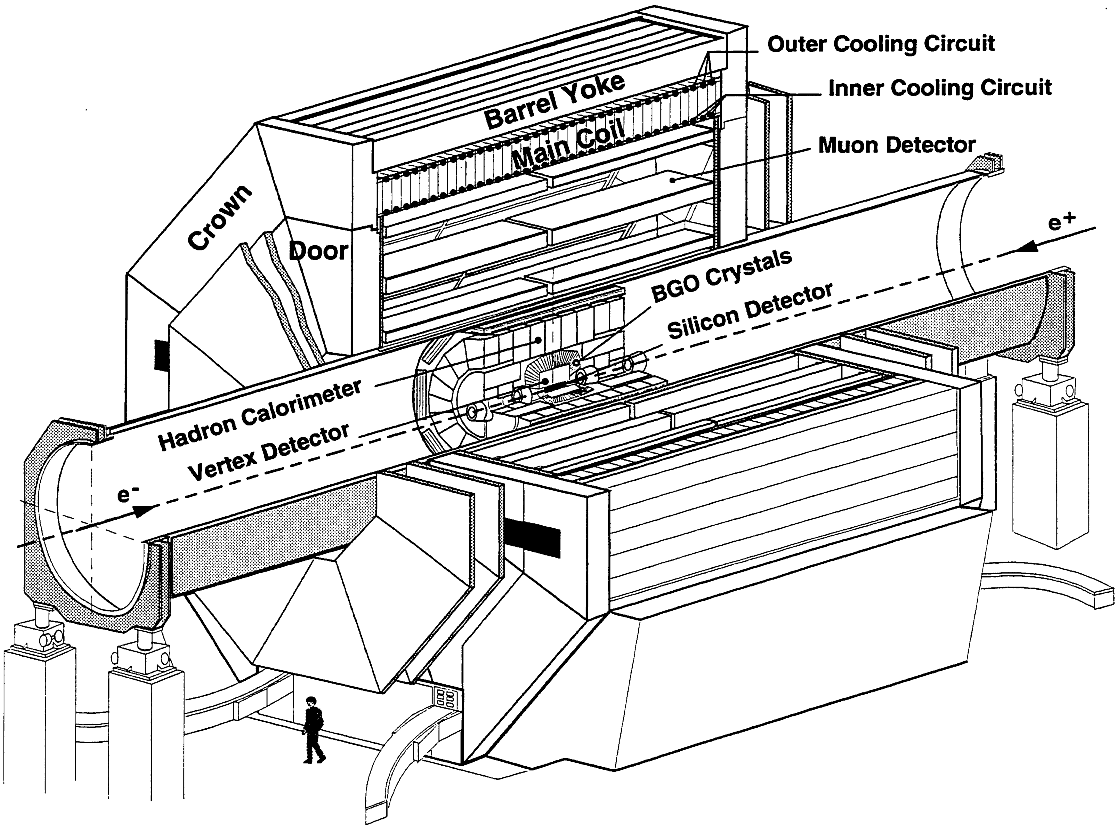

Figure 2.3: An overview of the L3 detector

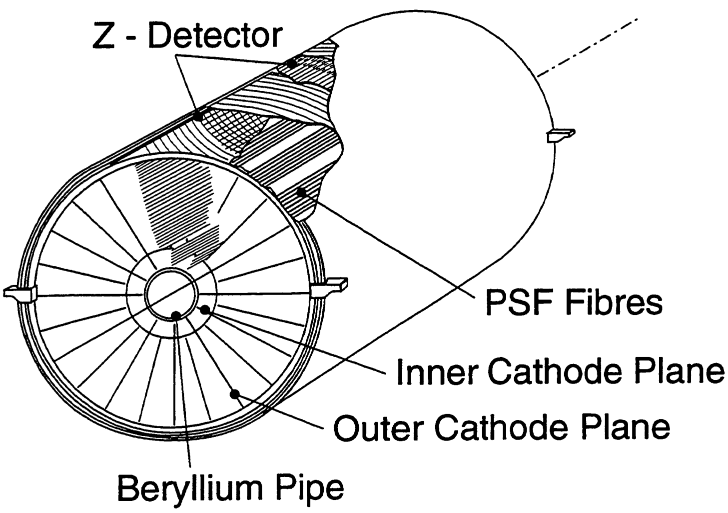

Figure 2.4: The TEC with its subcomponents.

sector builds a halfsector. Between the cathode and the grid is a drift region with slow drift velocity which provides a very high resolution in space, due to the long drifttime and the linear behaviour of the drifttime to distance relation over large areas of the detector.

This is achieved by using a mixture of 80 % CO_2 and 20 % isobutan as a gas with a low longitudinal diffusion and a nearly negligible Lorentz angle of 2.35°. The drift velocity in this area of the chamber is around 6 $\frac{\mu m}{ns}$. In the space between grid and anode there is a strong electric field providing the necessary gas amplification of the signal. Due to the strong acceleration in this region, the resolution for hits degrades and so this is also called the detection gap. The method to use a gas with slow drift velocity, small diffusion and a linear drifttime to distance relation, where the distance is measured with a precise time measurement, is called the time expansion principle.

An outer sector contains 54 anodes, which are measuring r and ϕ, while a inner sector has 8 such anodes. From the anodes in the outer TEC, 9 are read out on both sides to allow a z measurement using the charge division principle. In the inner TEC there are 2 such wires. Since the electrons can drift to the anode from both sides, the basic design can not distinguish whether the track is left or right from the anode. Two features enable this distinction. The inner sector is twice as large in azimuth as the outer one. So the combination of the inner and outer sector resolves the ambiguity as can be seen in figure 2.5. Groups of 5 grid wires in the outer sector are coupled to form a left right LR signal. There are 14 LR signals for each outer halfsector. These signals are also used to resolve the ambiguities. An inner sector and two outer sectors are called a segment. A segment showing the described setup is shown in figure 2.5.

In the region with linear drifttime to distance relation the TEC provides an resolution of 50 μm in the outer TEC and 60 μm in the inner TEC. The double track resolution is roughly 600 μm. The resolution neglecting the multiple scattering error is given by the Glückstern formula [54]:

$$\frac{\sigma_{p_t}}{p_t} = \frac{\sigma_{r\phi}}{0.3BL^2} \cdot \sqrt{\frac{720}{N+4}} \cdot p_t \ , \tag{2.1}$$

where B is in tesla, L in m, and p_t in $\frac{\text{GeV}}{\text{c}}$ is the transverse momentum with respect to the beam axis. The theoretical resolution in the linear area would be $1.15\% \cdot p_t$. The real average resolution including the nonlinear parts and the multiple scattering for high momentum tracks ($p_t \approx 45$GeV) is $1.8\% \cdot p_t$ and the distance of closest approach to the primary vertex is measured with an error of 109 μm [55].

Since 1993 the tracking was upgraded with a silicon microvertex detector, it provides useful data since 1994 and is improving the overall tracking performance by about a factor of two.

2.2.2 Calorimeters

The calorimetry in L3 is made of a bismuth germanate oxide crystal calorimeter, BGO, to measure electromagnetic showers, and a sandwiched hadron calorimeter

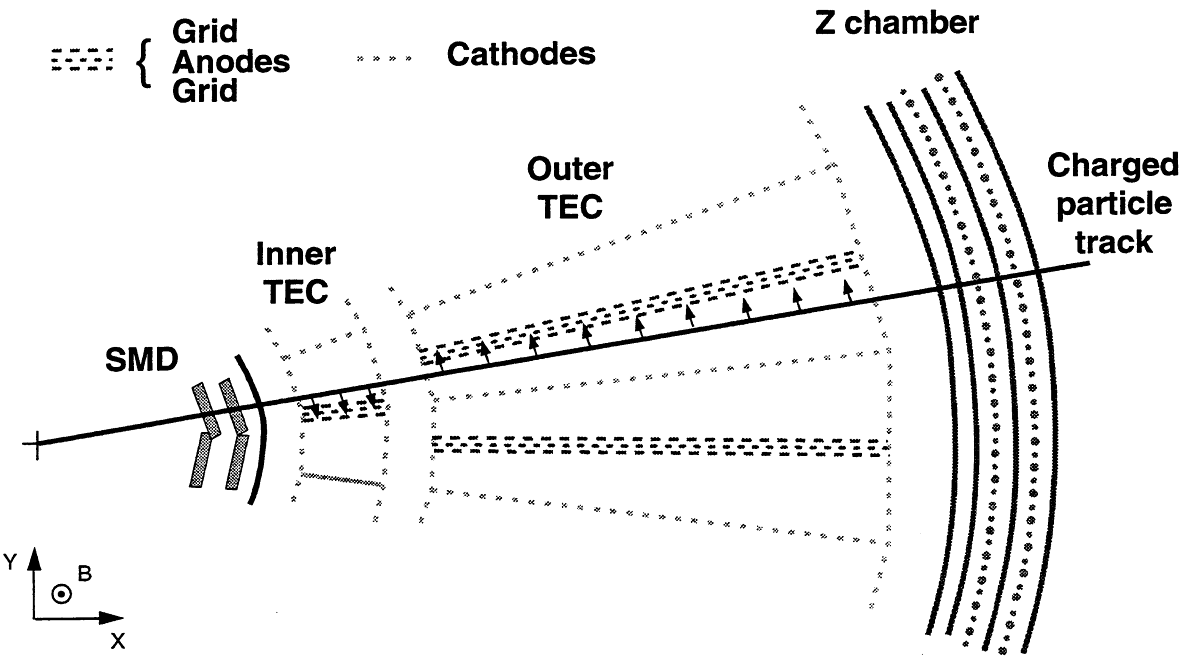

Figure 2.5: A segment of the TEC with the corresponding SMD and Z-chamber elements. The arrows indicate the drift direction of electron clouds coming from the track.

consisting of depleted uranium plates as absorber and proportional wire chambers as active elements.

The barrel BGO surrounding the central tracking system consists of two half barrels with 24 rings, which contain each 160 crystals, covering the range $|\cos\theta| < 0.74$. The crystals have a surface of $2 \times 2\text{cm}^2$ pointing towards the interaction region and a length of 24cm. Figure 2.6 shows the geometry of a crystal. Xenon lamps are used to calibrate the transparency of the crystals. The length of the crystal corresponds to 22 radiation length and about one nuclear interaction length. The endcap detectors sit behind the FTC and cover the range up to $|\cos\theta| < 0.98$. Including the endcaps the BGO consists of a total of 10752 crystals. The resolution for electromagnetic showers is $\frac{2\%}{\sqrt{E}} + 1\%$, where E is in GeV [56].

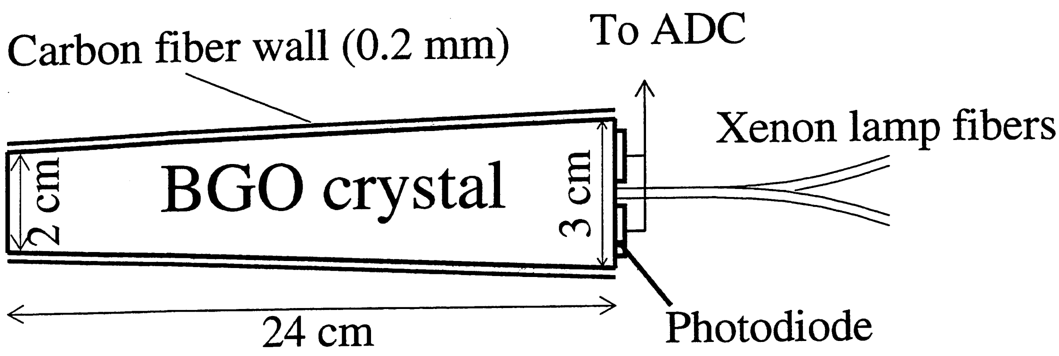

Figure 2.6: View on a BGO crystal of the electro-calorimeter

The hadron calorimeter has 55 mm thick uranium plates as absorbers. The energy is measured by the charge seen in the wire chambers between the absorber plates. In total it has about 6 to 7 nuclear interaction length, seen from the beam interaction point. The calorimeter covers the barrel region $|\cos\theta| < 0.82$ and with its endcaps up to $|\cos\theta| < 0.995$. As shown in figure 2.7 the hadron calorimeter barrel has 9 modules in z direction, where the 3 inner ones are long and have 10 radial segments and the outer ones are short and have 8 radial segments. In ϕ there are 16 modules, giving a total of 144 modules. In a module the sense wires of the active layer are grouped into towers which cover typically $2°$ in ϕ and in θ. The resolution of the hadron calorimeter is roughly $\frac{55\%}{\sqrt{E}} + 5\%$ where E is also in GeV.

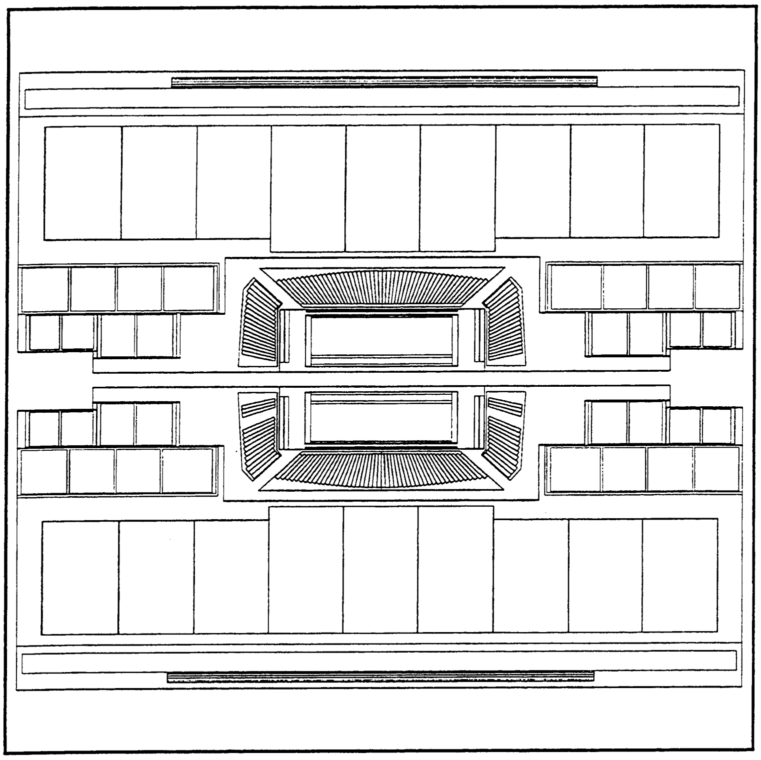

Figure 2.7: An overview of the parts of the detector which are inside the support tube. The modules of the hadron calorimeter and the crack between BGO barrel and endcap can be seen.

2.2.3 The muon system

The muon system is built out of very large multi wire proportional chambers with a wire plane of 5.6 m length. The chambers are ordered in octants. An octant is shown in figure 2.8. It consists of 5 precision (P) chambers ordered in 3 layers, which are measuring the r and ϕ coordinate. In the middle layer the track is measured with 24 wires in r in the outer and the inner layer with 16. In total a P chamber contains 320 signal wires and 300 wires for field shaping, cathodes and guard wires. The z-coordinate is measured in Z chambers which are mounted on the top and on the bottom of the inner and outer P chambers. So there are two layers providing z information with each two sets of chambers. Each measurement in the P chamber is done with a 250 μm accuracy per wire.The multiple sampling improves the resolution for a point taken for each layer and measures the slope at that point. The measurements in the z is done with a 500 μm precision per layer.

The momentum measurement is based on a sagitta measurement. With 3 points the resolution is given by [57]

$$\frac{\sigma_p}{p} = \frac{\sigma_s}{s} = \frac{\sqrt{\frac{3}{2}} \cdot \sigma_x \cdot 8}{0.3BL^2} \cdot p \,, \tag{2.2}$$

where B is in tesla, L in m and p in $\frac{\text{GeV}}{\text{c}}$. With the values given above, this allows the measurement from muons with 45GeV momentum with a resolution of 2.5% [58].

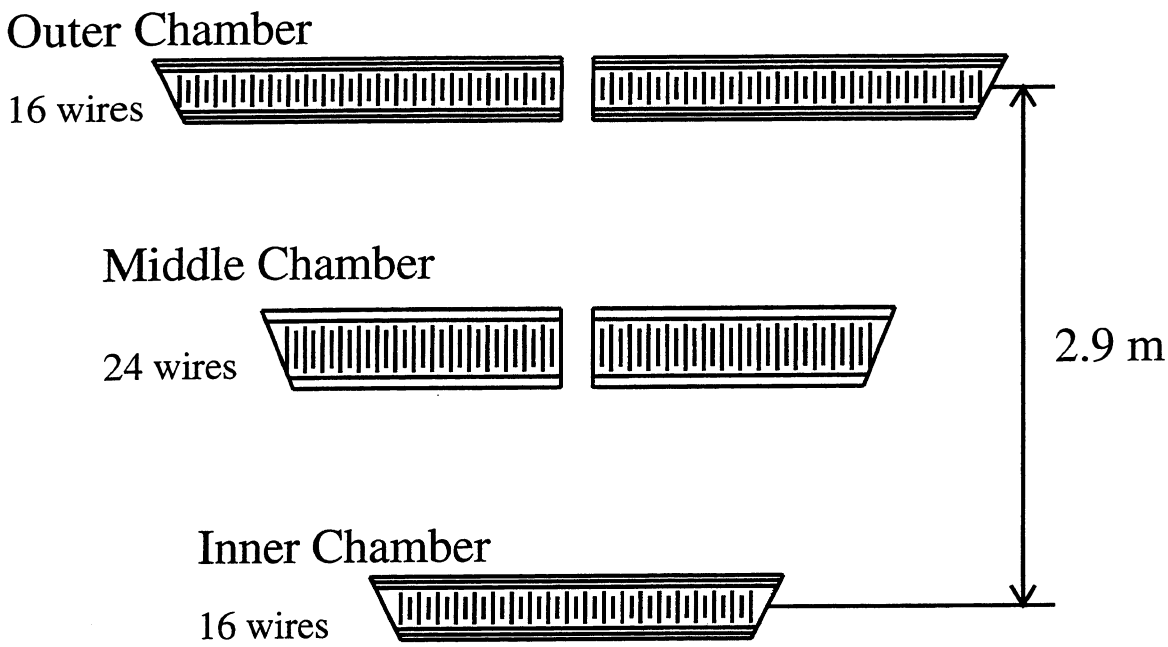

Figure 2.8: r-ϕ view of an octant of the muon system.

2.3 Data processing

Data handling is a main task to get physics results out of an experiment. The data processing chain begins with the online part, goes through the so called production, where the reconstruction of the basic properties of the event is performed, to the physics analysis.

The online processing is the part starting with the readout of the detector up to the point where the interesting events are written on an offline medium like a magnetic tape. The readout starts with the beamgate signal as level zero trigger. The beamcrossing time is 22 μs in the 4×4 mode and half as long in the 8×8 mode corresponding to a rate of 45 kHz or 90 kHz respectively.

It is not feasible to read out all the several 10^4 channels of the detector with this rate. Only the interesting values get propagated. For example the signals of the TEC get digitised in flash analog to digital converter FADC modules with 1024 channels with 6 bit for each channel. Instead of propagating roughly 1 kB of timing information for each TEC anode, the center of gravity, pulsheight and spread of a hit gets propagated. Therefore each FADC has its so called data reduction processor DRP, where these quantities are calculated from the

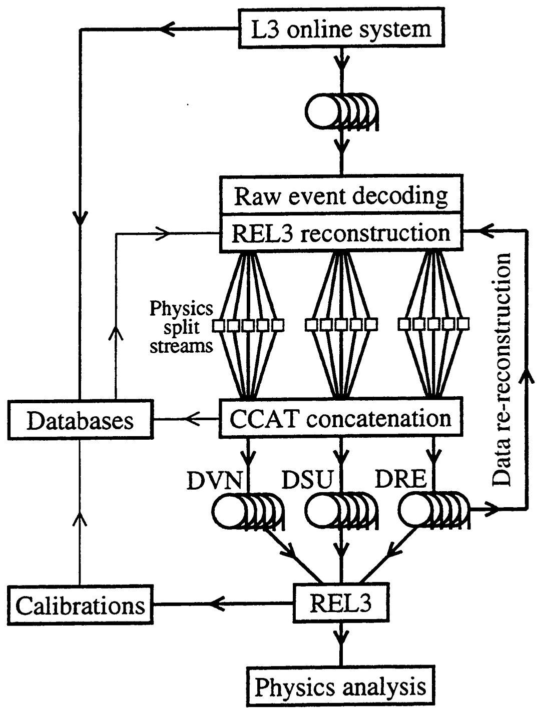

Figure 2.9: The event dataflow up to the point where the physics analysis starts.

raw FADC timing distribution. Also in this first stage of the digital readout electronics, the information is buffered until a trigger decision is made.

This leads to the other step to be done in parallel, proper triggering. The trigger of the L3 experiment has 3 stages. In level 1 the rate of positive decisions is $\approx$ 20Hz, in level 2 around $\approx$ 10Hz and after level 3 1 to 10 Hz. In the different steps of the trigger the event gets more and more reconstructed to do the trigger decision. This is performed by dedicated electronics. Like in the case of the FADC, the event is buffered in the readout electronics of the detectors and after a negative decision of the trigger the buffers are discarded. In the case of a positive trigger decision, the information of the readout of the subdetectors is collected by an event builder. In the case of a hadronic event, around 370 kB are then finally written to tape. This tape is called data acquisition DAQ tape. All slowly changing parameters of the data taking like high voltage, temperature and others are written to a database.

Then starts the data production as shown in figure 2.9 which provides fully reconstructed events. This production means the procedure of the reconstruction of DAQ tapes and the storage of the reconstructed quantities in the different formats as mentioned in figure 2.9 as DRE, DSU and DVN. After this production step the data are accessible to the different tasks of analysis. The data production is also protocoled in the database. The DRE is an extensive format from which a full reconstruction of the event is possible. It is used for calibration purposes and a rerun of the production if necessary. The DSU is a format where only some subdetectors can be completely reconstructed. It is also used for calibration, but

Format	$\approx$ Size per hadron [kB]	Structure and I/O
DAQ	370	ZEBRA, FZ
DRE	155	ZEBRA, FZ
DSU	27	ZEBRA, FZ
DVN	5	ZEBRA, FZ
DST	2.5 (5) [a]	COMMON block, C access to operating system

Table 2.1: The different data formats used.

[a]The smaller number is with data compression as described in the text.

it is important for the low level understanding of the reconstructed objects. The DVN contains only reconstructed quantities and is made for analysis. The reason to have multiple formats is simply the optimisation of the running time of the computing jobs.

All the reconstruction and analysis tasks up to this step are using REL3, the L3 reconstruction software, which relay on ZEBRA [59], a memory management system which implements abstract data types into the FORTRAN 77 framework. Part of the ZEBRA package are also the FZ package for sequential and the RZ package for direct access I/O.

A separate analysis software package was developped for the studies presented here, since it was easier to adapt to the computing environment used. Another production step was added into the chain, where the reconstructed tapes have been transformed into the so called DST format. Since the analysis software still relays on the FORTRAN written CERN libraries, FORTRAN is used as implementation language. The data are accessed by a common block structure. The I/O package which handles the DST is written in C. Since the whole analysis is performed on UNIX workstations, this enables using the features of the operating system. These are piped I/O and TCP/IP socket connections. The first one is used to pack the data with standard compression tools[2], the second one enables the use of a client/server model to access the tape drives of a workstation from a remote side. A summary of the size of the individual data formats is shown in table 2.1

Until 1995 the official L3 data production was done on VM mainframe machines for the I/O operations and multiprocessor UNIX workstations for the CPU needed. Since 1995 the production moved to a multiprocessor UNIX mainframe. The production had to process around 2 to 3 million events and roughly double the amount of Monte Carlo events. Counting for the several data streams and formats, this leads to a throughput of around 1-2 terabyte a year only for the data coming directly from the experiment. For the production of the DST and for the final analysis, UNIX workstations are used. The DST production runs over the DSU format. This leads to a yearly amount of data to handle which is around 50 to 100 gigabyte as input and 5 to 10 gigabyte as output. For the Monte Carlo data the numbers are roughly 50% higher. The data are finally stored on exabyte high density tapes and also as much as possible on disk.

[2]The gzip/gunzip package of the GNU-software foundation

The UNIX workstations used were an IBM RS/6000 AIX cluster containing 12 to 16 machines. Most of the data production is done by network. The data from the production are staged on the mainframe, and these staging disks are mounted as NFS filesystems. The infrastructure in the beginning was a bridged ethernet thin wire network. The maximal transfer rate was 10 Mbaud. This was not sufficient for the production of such an amount of data. To cope with this, the cluster was divided in short ethernet segments with up to six machines and then connected through dedicated gateway machines to the backbone using FDDI, which has a maximal transfer rate of 100 Mbaud. This makes it possible to perform a production run in roughly a week. The turnaround times, for a job running over the whole data set of either experimental data or Monte Carlo data, are between 5 to 10 hours or 20 to 40 events per second, where these rates include the time needed for network I/O.

Chapter 3

Event classification

The goal of this analysis is to measure quantities in $Z \rightarrow b\bar{b}$-events. The first step must be the selection of hadronic events $Z \rightarrow q\bar{q}(g)$. In these events $Z \rightarrow b\bar{b}$, so called b events, are selected. The class of events where the Z decays to other flavours are anti-selected. They build the class of non b-events. The later are especially important to cross-check the background for the b decays studies. To identify b and non-b events three techniques are used: (i) the b tagging with leptons, (ii) a classification using the decay length and (iii) an anti-b tag using the momentum of the leading particle.

3.1 Hadron selection

In hadronic events, $Z \rightarrow q\bar{q}(g)$, the primary quarks and hard gluons, which are sometimes radiated from the quarks, produce jets. These jets are collections of charged and neutral particles, mainly hadrons. They are a result of the fragmentation process, where the strong force creates the colourless singlets, and contain sometimes also leptons as decay products of hadrons in the jet. Therefore hadronic events are characterised by their high multiplicity in tracks and in energetic clusters. This multiplicity is the main criterion for the selection. If there is no semileptonic decay, these events deposit the center of mass energy E_{CM} in the detector, which could lead to another good criterion for the selection. In this analysis, however, semileptonic decays are from special interest.

The main backgrounds are t-channel photon exchange, where $e^+e^- \rightarrow e^+e^-q\bar{q}$ $q\bar{q}$ production and $Z^0 \rightarrow \tau^+\tau^-(\gamma)$where the τ decays to hadrons. In the case of t-channel photon exchange, the so called two photon-background, energy is carried away through the beam-pipe by the outgoing electrons. As a result, an energy imbalance is seen along the beam-direction. The energy imbalance of the events with semileptonic decays is more seen in the plane perpendicular to the beam. Another characteristic is that the jets from two photon events mainly have a direction close to the beam-pipe.

To classify the events, an event is divided in two hemispheres through the plane normal to the thrust at the vertex. The thrust T is defined by:

$$T = \max \left[\frac{\sum_i |\mathbf{p}_i \cdot \hat{\mathbf{n}}|}{\sum_i |\mathbf{p}_i|} \right] , \tag{3.1}$$

where $\mathbf{p}_i$ are the particle momenta and $\hat{\mathbf{n}}$ is the normal vector which maximizes T and defines the thrust axis. It is a quantity which expresses the direction and the spread of the monetum flow. The energy imbalance longitudinal and transverse to the beam direction is also used to classify the event.

The following criteria are used to select Z $\rightarrow$ hadrons events:

- The fraction of energy seen in the event must be between 0.4 and 2.0 times E_{CM}. The distribution of the visible energy fraction is shown in figure 3.1 together with the Monte Carlo prediction for signal (MC hadrons) and background. The Monte Carlo describes the distribution especially in the region where the background can be found. There is a minor disagreement for values above 1.4.

- There have to be at least 13 energetic clusters in the calorimeters, each one with an energy of more than 150 MeV. The distribution of the number of clusters for each event can be seen in figure 3.2. The Monte Carlo estimates the number of events in the range, where the background is found, slightly higher than what is seen in the data. The excess in the data seen for large number of clusters could be due to noise.

- The energy for each hemisphere is required to be larger than 0.1 times E_{CM}.

- The longitudinal energy imbalance has to be less than 0.5 times E_{CM}, and the transverse imbalance must be less than 0.9 times E_{CM}. The distributions of these two quantities is shown in figure 3.3 and they are well described by the Monte Carlo.

- More than 5 tracks in the event are required. The distribution of the number of tracks for each event can be seen in figure 3.4. This criterion is chosen against Z $\rightarrow \tau^+\tau^-(\gamma)$, therefore only signal (MC $\rightarrow$ q$\bar{\text{q}}$) and the τ-background is shown. The histograms are not accumulative, however, since high multiplicity range is nearly background free a disagreement for large number of tracks between data and Monte Carlo can be seen.

These are the so called basic criteria for the hadron selection.

Since one goal of the analysis is the measurement of missing energy in b decays, the detector must be as hermetic as possible. Therefore the events are accepted only in the homogeneous part of the detector. The absolute value of the cosine of the angle between the energy flow of a hemisphere and the beam is required to be smaller than 0.7. Additionally, at least one hemisphere has to have this value smaller than 0.65. A good energy measurement in the event requires that there is no more than 2GeV of identified noise in the electromagnetic calorimeter. The cuts described above are very similar to the analysis of the cross-section Z $\rightarrow$ q$\bar{\text{q}}(\gamma)$ in [60].

In the 1992 period of data taking a ring, corresponding to 160 crystals out of roughly 11000, in the electromagnetic calorimeter did not work. For data of this period the thrustaxis and the missing energy should not point into the direction of this ring. Also no more than 5.0GeV should be seen in the forward backward calorimeters. The last two criteria ensure that the particles do not partly escape in the forward direction or into cracks.

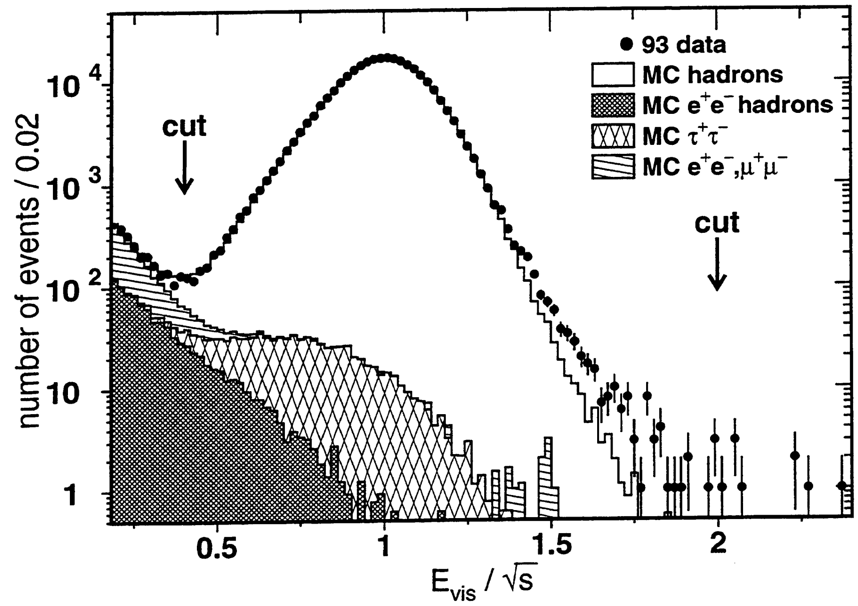

Figure 3.1: The visible energy relative to the beam energy.

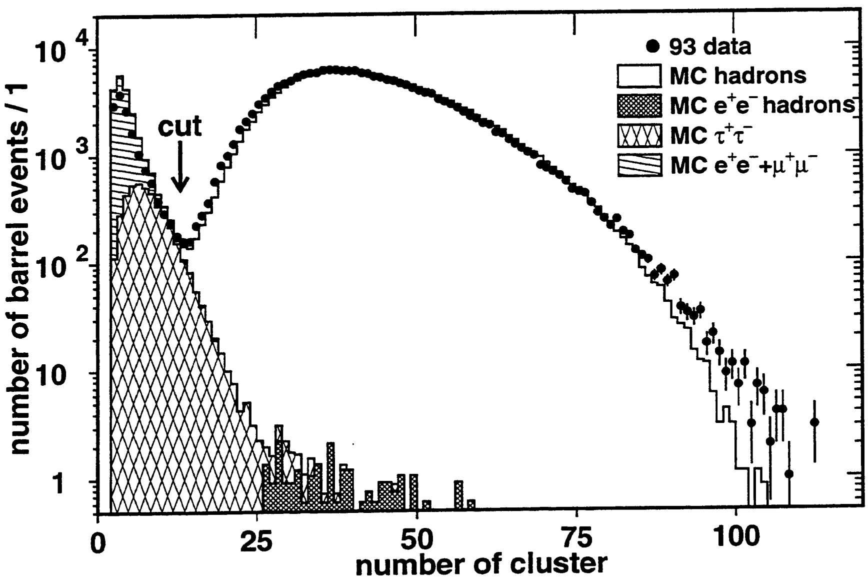

Figure 3.2: The number of calorimetric clusters for different event sources.

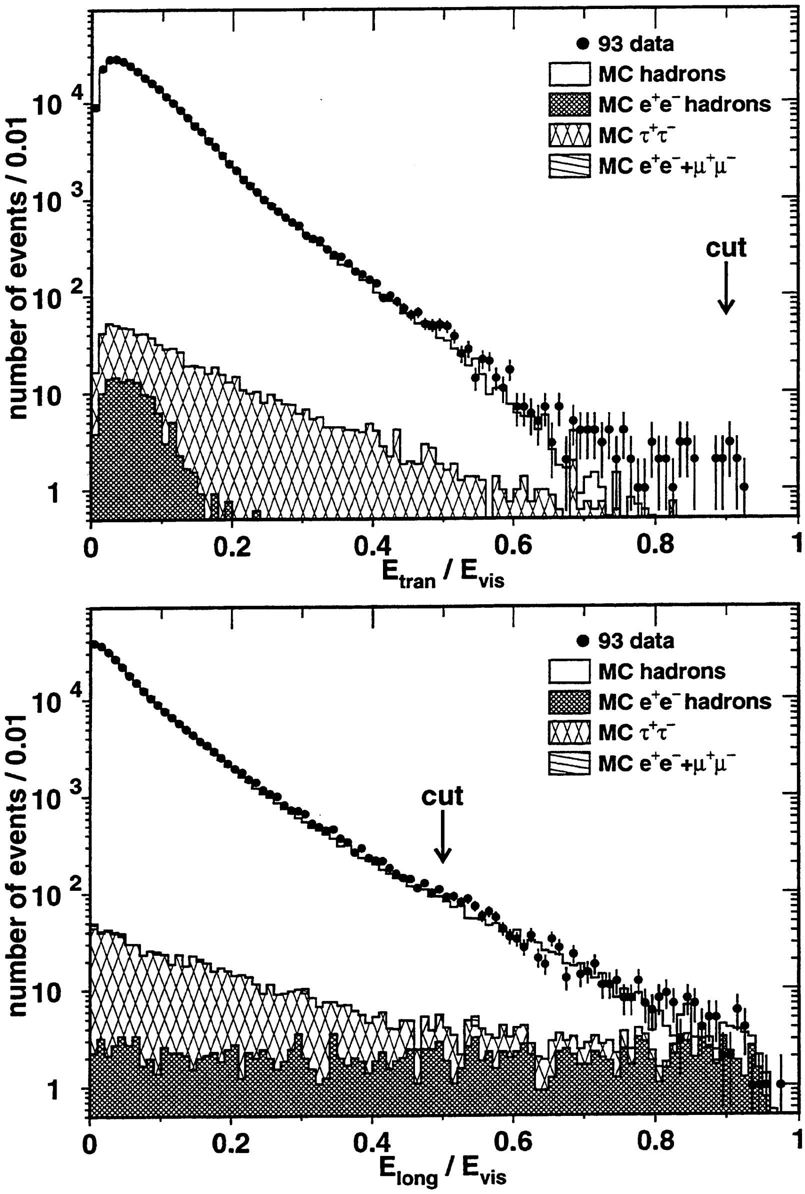

Figure 3.3: The relative energy balance. In the upper plot the transversal balance and in the lower plot the longitudinal balance are shown.

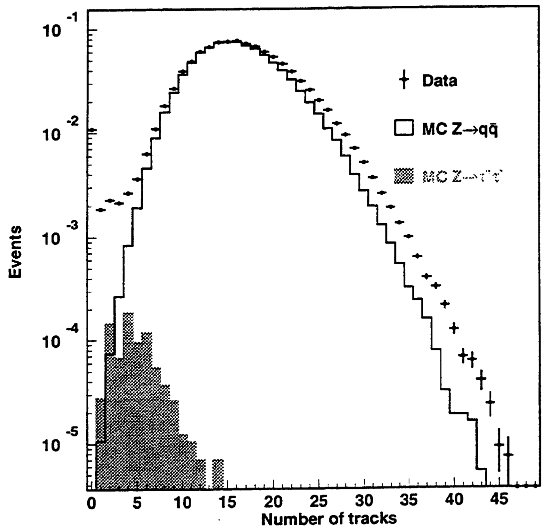

Figure 3.4: The number of tracks after applying the energy cuts in the barrel and $|\cos\theta| < 0.7$. Only the events with more than 5 tracks are accepted. This criterion removes roughly half of the remaining $\tau\tau$-events. The Monte Carlo distributions are shown separately.

Background sources involving missing energy should be further reduced compared to other measurements in hadronic Z decays. For example the cross-section measurement [60], where these backgrounds are statistcally not important. To reduce remaining Z $\rightarrow\tau^+\tau^-(\gamma)$background, the number of tracks with a momentum transverse to the beam greater than 150 MeV and a distance of closest approach to the fill vertex of less than 1mm is counted. The distribution of this number of tracks for each event is shown in figure 3.5. Analog to figure 3.4, in figure 3.5 only the signal and the Z $\rightarrow\tau^+\tau^-(\gamma)$background is shown. An improvement in the description by the Monte Carlo can be observed, comparing the high multiplicity side with the one in figure 3.4. Events are accepted with:

- more than 10 such tracks,
- if they have less than 10 tracks, but more than 10 calorimetric clusters in at least one hemisphere. The discrimination can be seen in the distribution of the number of clusters of one hemisphere versus the other hemisphere in figure 3.6.
- If the conditions above are not fulfilled, but the event has not three tracks per each hemisphere, the event is also accepted. The distribution of the number of tracks of one hemisphere versus the other hemisphere is seen in figure 3.7.

To reduce the remaining two photon background for events with less $0.7E_{CM}$ it is required that the missing energy transverse to the beam is either greater than $0.5E_{CM}$, or greater than the energy missing in beam direction.

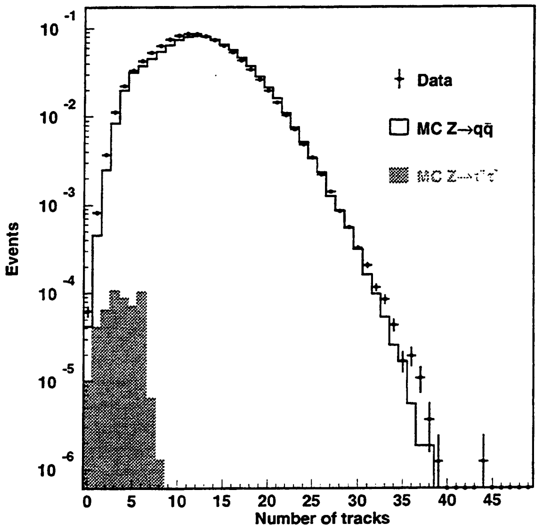

Figure 3.5: The number of tracks before the additional criteria against Z $\rightarrow\tau^+\tau^-(\gamma)$are applied. The track quality is slightly tightened, so that also number of tracks below 5 are in the distribution. The remaining $\tau\tau$-background cluster below 10 tracks for each event. The Monte Carlo distributions are shown separately.

In total, 900k hadronic events are selected with the basic criteria from the 1991 and 1992 data taking period. In the five flavour Monte Carlo are 1.1M. The samples do not correspond to the same luminosity. 402k events are then selected in the data, and 497k events in the Monte Carlo, where the biggest loss in the efficiency is due to the restricted acceptance. The background fraction estimated from the Monte Carlo is $< 10^{-5}$ for $Z^0 \rightarrow \tau\tau$-events and $\gamma\gamma$-events.

This study is concentrated on neutrino measurement inside jets, where the neutrino is seen as missing energy $E_\nu \approx E_{Beam} - E_{Jet}$. This relation is only valid for two jet like events. Since there is no sharp criterion to define a jet, first the jet definition in this framework should be introduced. A geometrical criterion is used, which is a cone with a halfangle of 20° around the cluster with the highest energy deposit, where then all particles in the cone form the jet. This is reiterated for the remaining clusters. These jets are further combined, if

- jets are in the same hemisphere defined by the thrust axis,
- the invariant mass of the jets is less than 25GeV, and
- the angle between the jets is less than 90°.

The two jets sample where the analysis is performed requires that the event has exactly one jet in each hemisphere. This final sample contains 346k events in the data and 424k in the Monte Carlo.

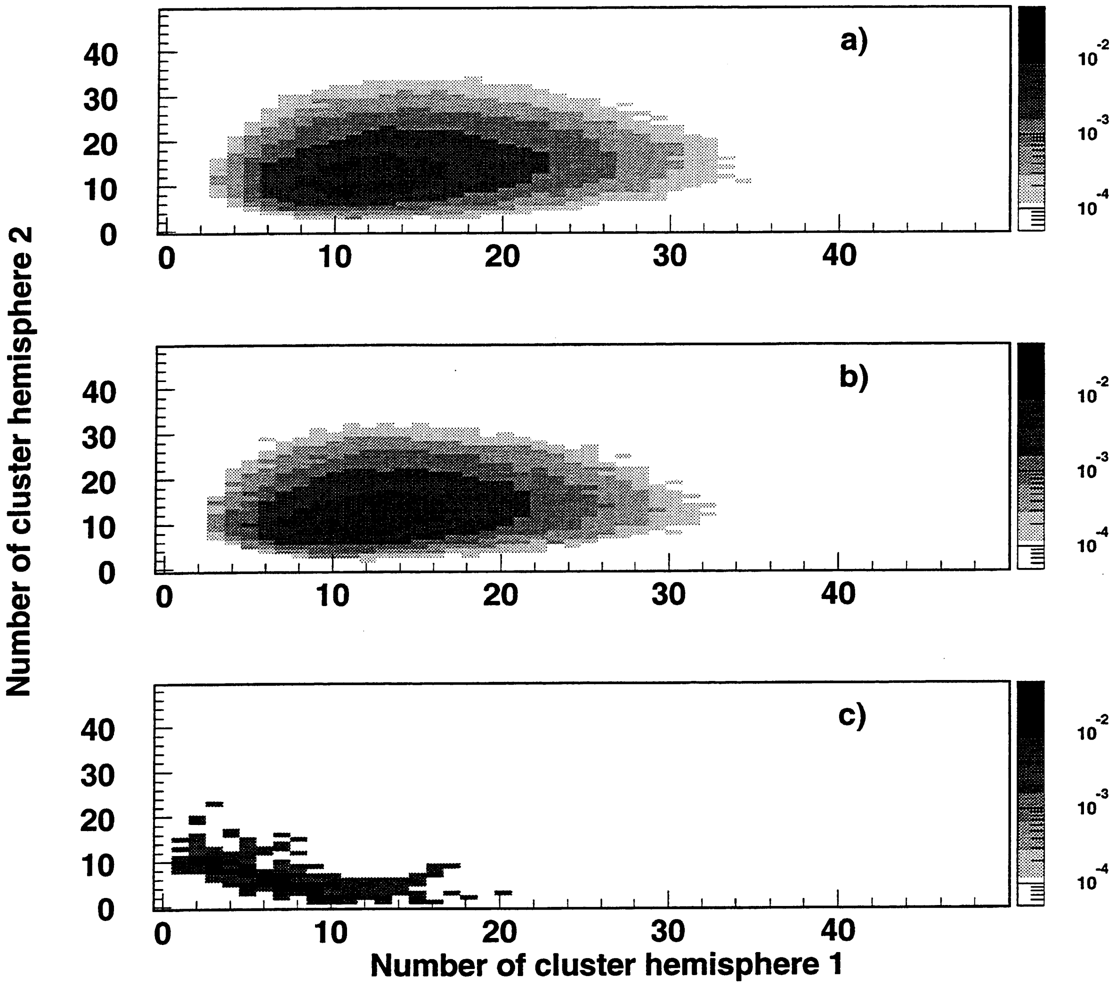

Figure 3.6: Correlation of the number of cluster in the two hemispeheres for events with less than 10 good tracks. The gray scale indicates the event fraction, for data (figure a), Z $\rightarrow$ q$\bar{\text{q}}$ Monte Carlo (figure b) and Z $\rightarrow$ $\tau\bar{\tau}$ (figure c). All distributions are normalised.

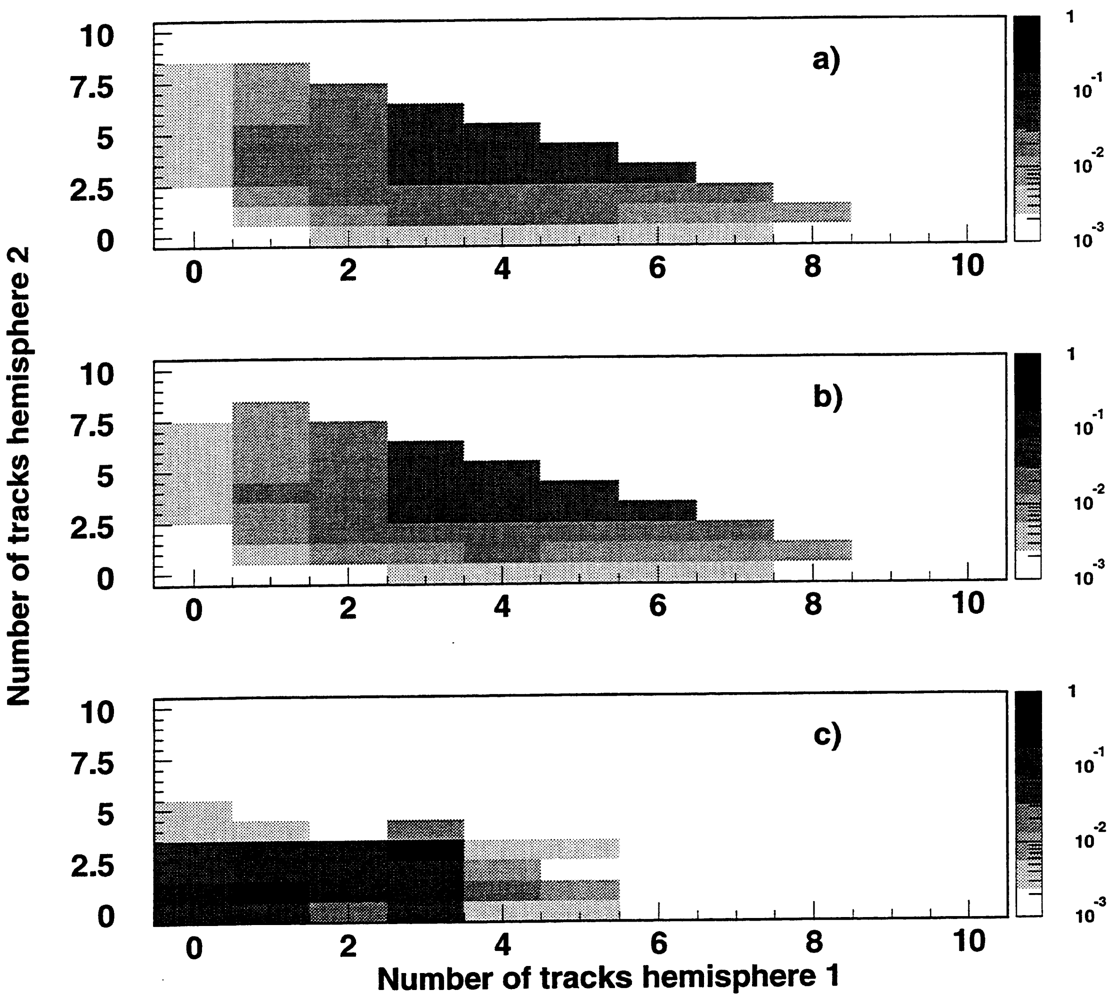

Figure 3.7: The correlation of the number of tracks in the two hemispeheres of the remaining events before the three tracks against three tracks cut. Again the gray scale indicates the event fraction, where data (figure a) and Z $\rightarrow$ q$\bar{\text{q}}$ Monte Carlo (figure b) and Z $\rightarrow \tau\bar{\tau}$ Monte Carlo (figure c) are normalised.

3.2 B-tagging with leptons

A well established method is the identification of b-decays with electrons and muons which have a large transverse momentum to the direction of flight of the b-hadron, due to the high mass of the b-quark. Here only the identification of the electron and muon candidates will be discussed. Their spectra, and the final differentiation will be presented in detail in context with the measurement of the branching ratios in chapter 5.

In the L3 detector electrons can be characterised by an electromagnetic shower in the calorimeter associated with a track. The shower shapes of particles in the calorimeters will be discussed in more detail in chapter 4.1.1. The conclusion is, that an electromagnetic shower is narrow in the electromagnetic BGO-crystal calorimeter without activity in the hadron calorimeter behind. This leads to the following criteria for electron identification:

- To quantify the narrowness of the shower in the electromagnetic calorimeter the ratio of the energy deposit in the nine central crystals, E9, over the energy in the 25 central crystals, E25, is used after corrections which assume an electron. This corrections will also be discussed in chapter 4.1.1. The distribution of the ratio E9/E25 is shown in figure 3.8. The correction for causes the ratio to be greater than one especially for minimum ionising particles. A ratio of greater than 0.95 is required for electron candidates. The number of crystals associated to the shower has to be between 10 and 40, the distribution is shown in figure 3.9. This criterion removes also minimum ionising particles from the sample.

- The candidate has to have an energy deposit of at least 3GeV in the BGO. The distribution of the energy deposit of the candidates in the BGO calorimeter is shown in figure 3.10. To fulfil the condition of no hadronic activity in the shower, the energy deposit due to shower leakage into the hadron calorimeter in a cone of 50 mrad behind the BGO should be lower than 2GeV. The corresponding energy distribution in the hadron calorimeter can be seen in figure 3.11.

- The track pointing to the shower has to match the shower's position in a azimuthal angle of 4 mrad $+ \frac{8\,\mathrm{mrad}}{E_{BGO}}$, where E_{BGO} is taken in GeV.

- The electron is inside a jet where lot of tracks and π^0 and hence γ activity is found, also an isolation criterion is required. There should be no other track in a cone of 5mrad. The distribution of the isolation angle is shown in figure 3.12.

- Since the electron is very light ($m_e \approx 511$keV), the momentum of the track should be the same as the energy which is measured. As a last criterion to enhance the purity, the measured transverse momentum with respect to the beam of the electron candidate should be consistent with the measured transverse energy within three standard deviations. The position of the

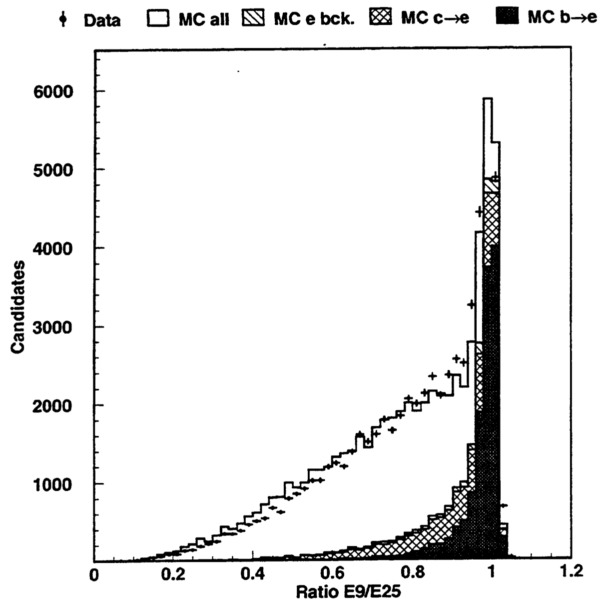

Figure 3.8: The energy ratio E9/E25 is shown. The candidates where the ratio is larger than 0.95 are accepted.

cluster is used to associate a direction to the measured energy. The distribution of the absolute difference between these quantities is shown in figure 3.13 and good agreement between data and Monte Carlo is found.

In figures 3.10 to 3.13 all criteria are applied except the one of the quantity shown. Background sources are also electrons from charm decays and other non b electrons. The latter consist of electrons from c or b hadrons decaying to $\tau \rightarrow$ e and also electrons from γ conversion, these are referenced as MC e-background in the figures. The Monte Carlo describes the ratio E9/E25 very poorly in the signal region, the distribution of the number of crystals is shifted in the data towards lower values compared with the Monte Carlo. The spectra of the candidates in the BGO as well as in the hadron calorimeter shows an overestimation of the number of candidates by the Monte Carlo for low energy values. Since all criteria are applied, the samples shown in the distributions are relatively clean. Therefore a lower efficiency in the data compared with the Monte Carlo for low energetic electron candidates is indicated.

The performance of the tracking system degrades outside the barrel region, because the number of hits which can built a track is reduced due to the geometry. Also the BGO calorimeter has a gap between barrel and end-cap region, which is visible in the distribution of the cosine of the polar angle θ in figure 3.14. Therefore the candidates are only taken from the very homogeneous barrel part of the detector, and for the angle θ between the direction of the center of gravity of the electromagnetic shower and the beam direction $|\cos\theta|$ less than 0.72 is required.

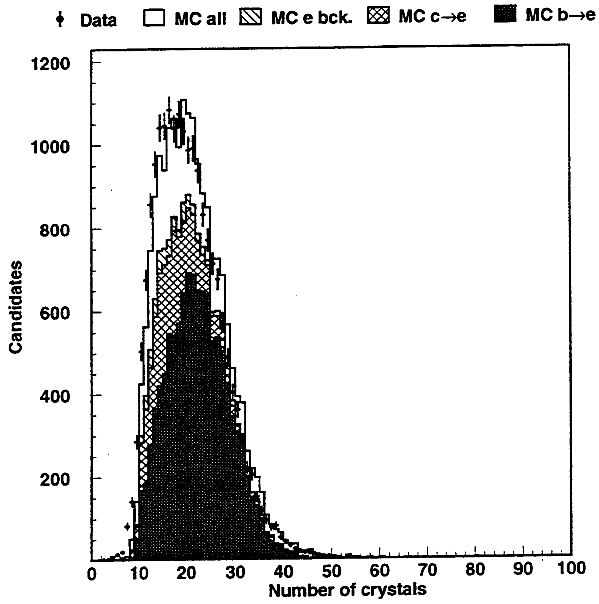

Figure 3.9: The number of crystals associated to a cluster is shown. For electron candidates between 10 to 40 crystals are required.

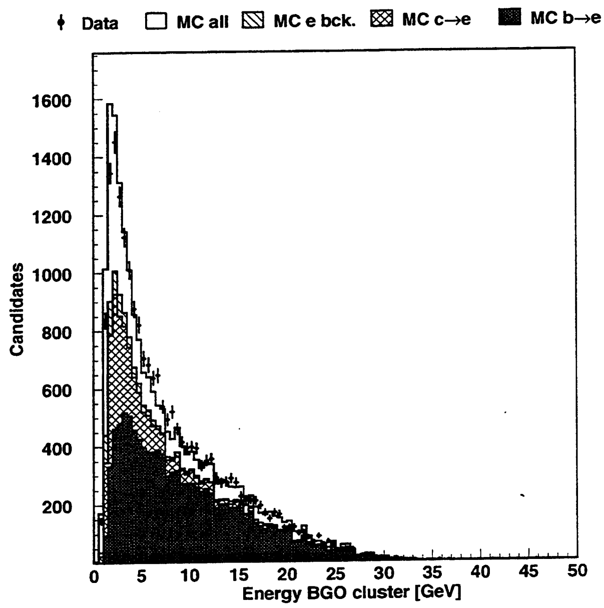

Figure 3.10: The energy of the BGO clusters is shown. Clusters with more than 3GeV are accepted.

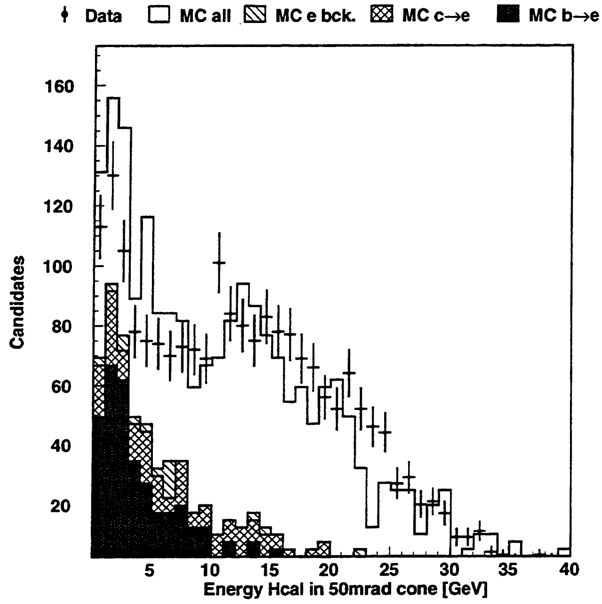

Figure 3.11: The energy in the cone of 50mrad behind the BGO in the hadron calorimeter is shown. Clusters with less than 2GeV in the hadron calorimeter are accepted. Candidates releasing all their energy in the BGO are not shown.

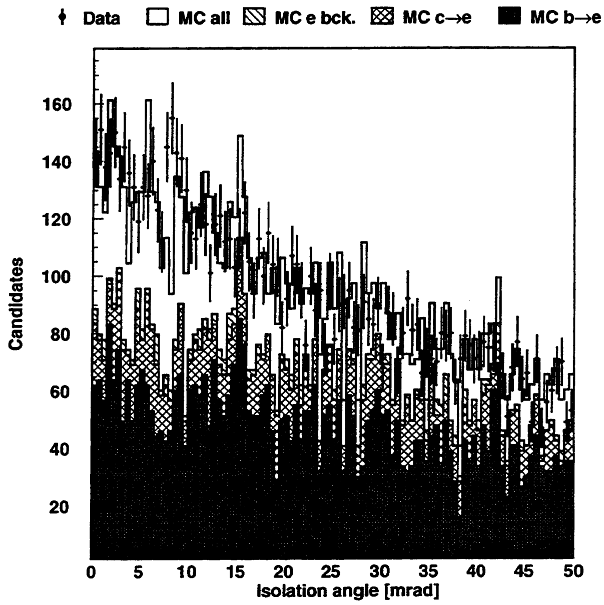

Figure 3.12: The distribution of the angle of the candidates track to the nearest neighbouring track is shown. Candidates with an angle of more than 5 mrad are accepted.

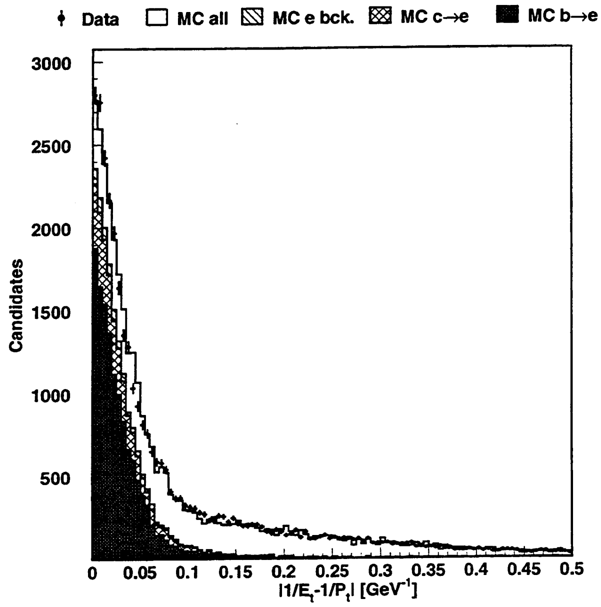

Figure 3.13: The absolute difference of the inverse p_t with respect to the beam and the inverse transverse energy E_t is shown. This expresses the difference in the expected curvature predicted by the calorimeter and the curvature measured by the tracking system for a massless particle. The clusters with less than 0.055GeV^{-1} are accepted.

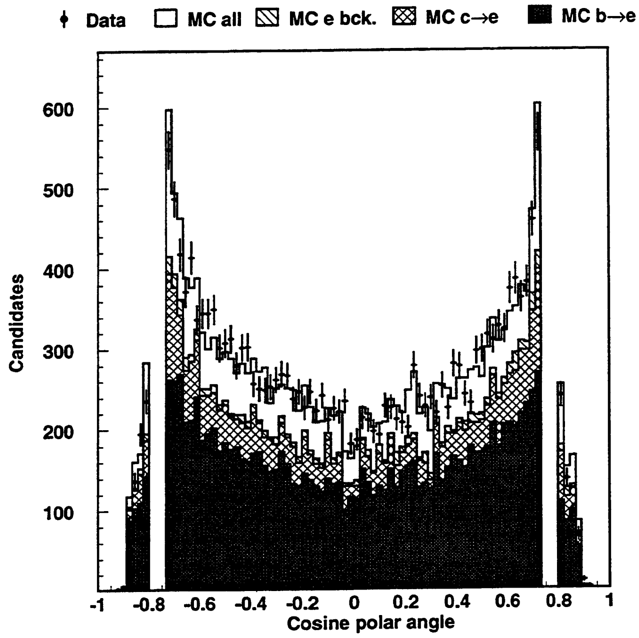

Figure 3.14: The $\cos\theta$ distribution of the electron candidates. They are only accepted if $|\cos\theta| < 0.72$.

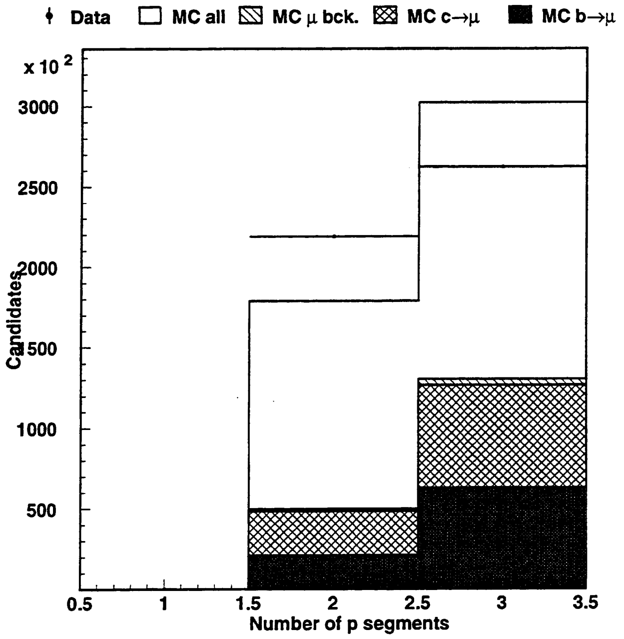

Figure 3.15: The number of r-ϕ measuring segments on muon tracks. Tracks are built if at least two segments have fired.

Muon candidates are identified in the muon system. The main background for muons coming from the interaction in the experiment are muons from the decay of hadrons and punch through of hadronic showers through the muon filter into the muon system. With a very high probability these tracks do not point to the interaction vertex of the beam collision. The criteria to select muon candidates are as follows:

- First quality criteria are required, the candidate's track has to have at least signals in two layers in the plane orthogonal to the beam and one parallel to the beam. The first criterion is performed automatically by the L3 reconstruction program, since tracks are only build, if at least two r-ϕ layers give a signal.
- Then the track should come from the vertex. The distance of closest approach, DCA, with respect to the vertex in the r,ϕ plane should be smaller than 100 mm taking into account multiple scattering in the calorimeter. This distance should also be smaller than three standard deviations of the estimated multiple scattering error.

The distributions of the variables used in these criteria are shown in figure 3.15, 3.16 and 3.17. The distribution of the number of r-ϕ segments shows that the data have much more doublets than triplets than predicted by the Monte Carlo. In the DCA distributions in the data a small excess for low values of DCA can be observed.

To classify an event as a b event, we require, that at least one hemisphere contains an electron candidate with a momentum of more than 3GeV and a transverse

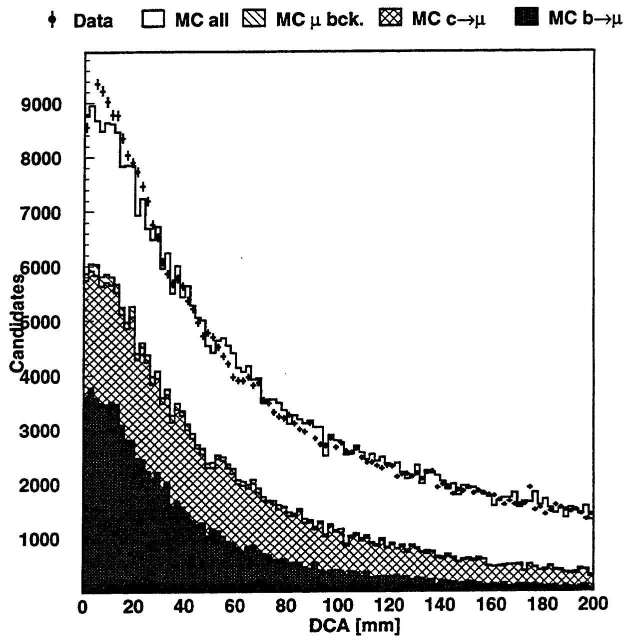

Figure 3.16: The distribution of the distance of closest approach (DCA) to the vertex. This is extrapolated back through the calorimeters taking into account the multiple scattering. Tracks are accepted if DCA is less than 100 mm.

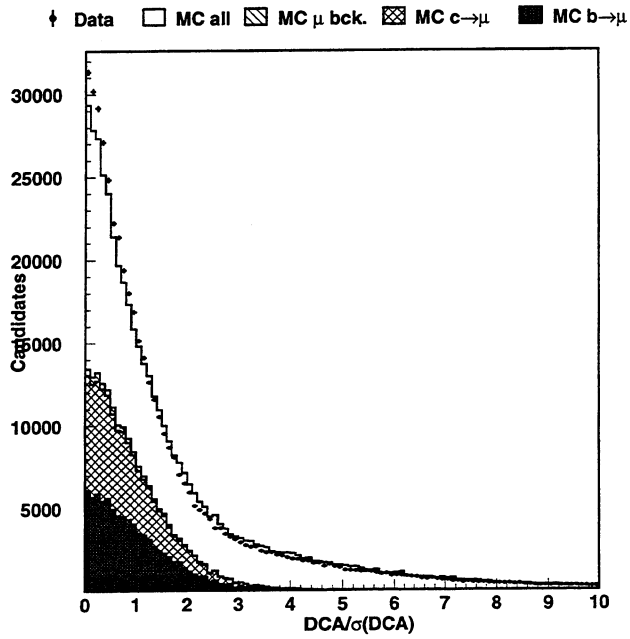

Figure 3.17: The distance of closest approach at the vertex divided by its error is shown. It takes into account the error due to the extrapolation through the calorimeter. Only tracks with less than three standard deviations are accepted.

momentum with respect to the nearest jet of more than 1.4GeV. In the case where a muon candidate is found instead of an electron a momentum of more than 4GeV and again a transverse momentum with respect to nearest jet of more than 1.4GeV is required. These samples will be called the electron and muon sample respectively, depending on whether the sample is tagged with electrons or muons. The combined electron and muon sample will be called the lepton sample. The b purity of the lepton sample is 83% according to the Monte Carlo.

3.3 Tagging with the event distance

This tag uses the fact that b-hadrons, due to their long lifetime of 1.5 ps and the boost corresponding to an average energy of roughly 32GeV in a LEP I experiment, have a decay vertex separated from the primary vertex. A so called total distance of the event is constructed to quantify the probability that such a separated decay vertex exists.

To construct this distance, the event is separated into two hemispheres by the plane going through the primary vertex orthogonal to the thrust axis. In each hemisphere up to 3 high quality tracks with the largest impact parameter are used to calculate a distance per hemisphere. This distance is the impact parameter projected on the thrust axis weighted by the transverse momentum with respect to that axis. The sum of the single hemisphere distances gives the total distance of the event.

High quality tracks in this framework means tracks with well measured distance of closest approach from the vertex. To assure this, it is required that the tracks have at least one hit in the inner tracking chamber and are in the high resolution region of the tracking device. This excludes the region of an angle of 15 mrad around an anode or cathode plane except where the anode of the inner chamber is aligned with the anode of the outer chamber. There the exclusion angle is 30 mrad. Also a minimal track momentum of 500 MeV is required. To suppress background from γ conversion, the distance of closest approach should be smaller than 1.2 mm. Since the intercept of the track with the thrust axis gives the position of a secondary vertex, a minimal angle of 75 mrad between thrust axis and track is required.

These tracks with the algorithm described above give two tags:

- the b-enriched lifetime tag with a total distance greater than 3.5 mm which has about 59.4% b purity, where the purity is measured in the data with the seen prompt leptons in this sample,
- the b-depleted anti-lifetime tag with a total distance less than 0.0 mm which has about 10% b purity.

The total distance distribution is shown in figure 3.18, where also the two samples are indicated. On the positive tail of the distribution the data favour more higher values of the distance, especially in the signal region of the lifetime tag, and there is a depletion on the negative tail up to -5 mm.

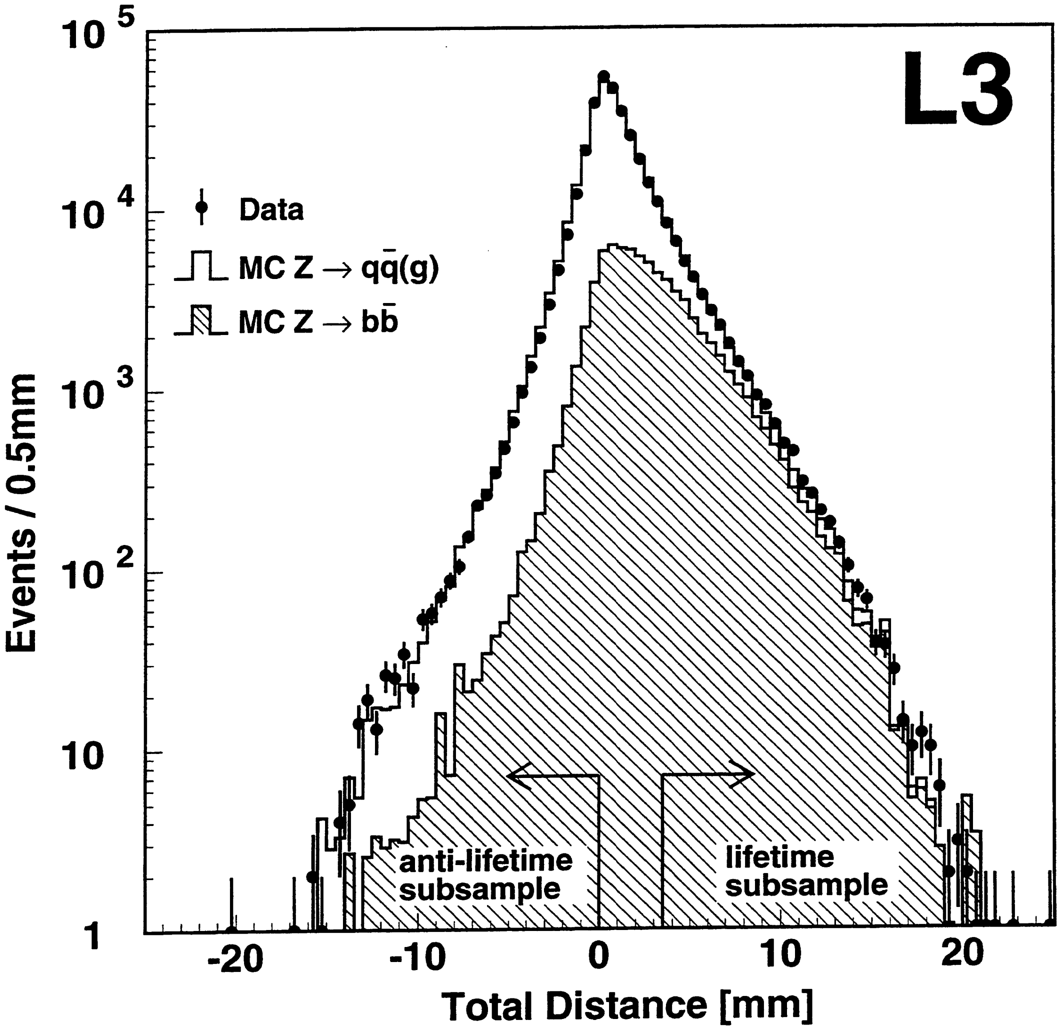

Figure 3.18: The total distance of the events.

The b purity of the lifetime sample predicted by the Monte Carlo is 60.8%. The small misdiscription of the lifetime sample by the Monte Carlo causes a high systematic uncertainty in the purity, because the background has a high share. Since the purity is an essential ingredient for the neutrino branching ratio measurement, it is estimated with the charged leptons, after the measurement of the branching ratio of b hadrons into electron and muons as described later on.

The lepton candidates are counted in the lifetime sample. The ratio of the events with lifetime tag and high $p_\perp$-lepton over the number of high $p_\perp$ leptons gives

$$f^{\tau_b l} = \frac{N^{\tau_b l}}{N^l} = P^l \epsilon_b^{\tau_b} + (1 - P^l)\epsilon_u^{\tau_b} , \tag{3.2}$$

where τ_b denotes the lifetime tag, l the lepton tag, ϵ_b the efficiency to see b-events, ϵ_u the efficiency to see non-b events and P the b purity. Monte Carlo predicts a b purity of $\approx 95\%$ for the sample tagged with the lifetime criterion and a lepton tag. Neglecting the background, the ratio of the data over the Monte Carlo leads to

$$\frac{f^{T_b l}_{Data}}{f^{T_b l}_{MC}} = \frac{\epsilon^{T_b}_{b\ Data}}{\epsilon^{T_b}_{b\ MC}} , \tag{3.3}$$

if the purity in the lepton sample P^l is also taken from the Monte Carlo. Thus the comparison of the fraction of events tagged with the lifetime criterion and the lepton tag determines b efficiency of the lifetime tag. If the background efficiency $\epsilon^{T_b}_u$ for the lifetime tag is taken from the Monte Carlo, also the purity of the lifetime tag is determined, since in general the b purity P is given by

$$P = \frac{R_b \epsilon_b}{R_b \epsilon_b + (1 - R_b)\epsilon_u} . \tag{3.4}$$

Thus determing the efficiencys of the lifetime tag determines also its b purity.

The systematics of this method to determine the purity are discussed. One source is of course the systematics due to the neglected background, but this error is small. It can be estimated by the first order of the ratio on the left side of equation 3.3 using equation 3.2. It can be written as

$$\frac{b' + x}{b + x} = \frac{b'}{b} + \frac{b - b'}{b^2} x , \tag{3.5}$$

where $b' = P^l \epsilon^{T_b}_{b_{Data}}$ and $b = P^l \epsilon^{T_b}_{b_{MC}}$ are the b-event fractions and $x = (1 - P^l)\epsilon^{T_b}_b$ is the background fraction. Numerically the first order correction can be estimated to be less than 0.1%. Another systematic of this method is the dependency of this ratio from the branching ratio b $\rightarrow$ e(μ)νX. A different branching ratio would result in a different purity P^l than predicted. Given the measured uncertainty of this branching ratio, as described later, the error is even less than 0.1%. The statistical error of the combined lifetime and lepton tagged sample is of the order of 2.5% relatively. This is the dominant error, and it is taken as error of the determination of the purity by this method. So a value of 59.4$\pm$1.5% is obtained.

3.4 High x tag

Particles containing the primary quark in Z $\rightarrow$ q$\bar{\text{q}}$ decays carry a large fraction of the beam energy. In the case of u, d and s pairs many of these particles decay so late, that they are visible in the tracking device or give a single cluster in the calorimeter.

This can be used to obtain a tag to suppress events containing b-quarks. The relative energy fraction of the particle compared to the beam energy $x = \frac{E_{particle}}{E_{beam}}$ is used. Therefore this kind of tag is called high x tag, which was first used by the HRS collaboration [61]. In the analysis presented here the following criteria are used for the high x tag:

- The tag requires a track with x greater than 0.6 and an associated calorimetric cluster with x greater than 0.50,
- or a π^0 candidate with x greater than 0.5 in a single electromagnetic cluster.

The remaining b contribution is about 10%.

Chapter 4

Jet-energy measurement and calibration

The measurements presented are using missing energy in a jet, thus it is important to have a good jet-energy measurement. There are two items which have to be addressed. First the energy response of different detector modules is studied and second the energy scale has to be determined. In most calibrations in e^+-e^- experiments the scale is simply the beam energy. Here another approach is taken, which will be discussed in the second section of this chapter.

4.1 Detector response to jets

4.1.1 Response to single particles

The L3 detector has two stages for the calorimetry as described earlier. The energy of electrons and photons is mostly absorbed in the BGO calorimeter, the energy of hadrons in the hadron calorimeter. The dominant process in the BGO is a shower caused by bremsstrahlung and pair production. The particles of the shower ionise lattice atoms and hence create electron hole pairs in the crystal. These pairs interact with the so called activator atoms in the crystal. Such an atom then goes into an excited state. This state decays and produces light [57]. The amount of light produced by a shower is proportional to the energy deposit.

In the hadron calorimeter the dominant process is nuclear interaction with the nuclei of the absorber material. In this interaction of the incoming particle also charged particles are produced. When these particles cross an active layer, the charged particles ionise the gas. The charge is collected at the anodes and its amount is proportional to the energy deposit in this layer. The particles again come into an absorber layer and produce again multiple nuclear interactions. In the following active layer again the charge of the ionised gas is proportional to the energy deposit in this layer.

The BGO has 22 radiation length and one nuclear interaction length. The hadron calorimeter has 6 to 7 nuclear interaction length, depending on the particle's path. The showers in the BGO initiated by the dominant processes are called electromagnetic showers and the showers in the hadron calorimeter are called

Energy Measurement

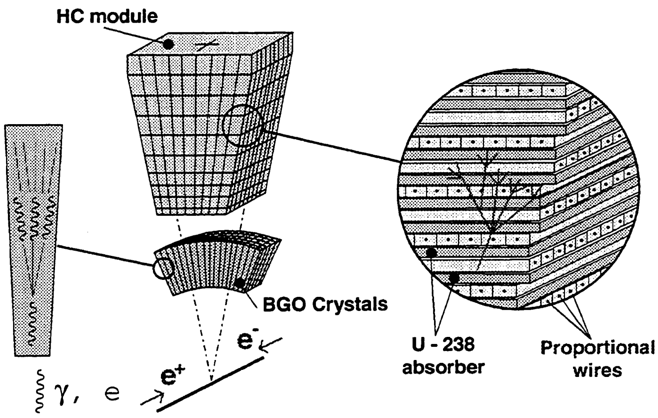

Figure 4.1: A scheme of the energy measurement and the two stages of the calorimeter. The electromagnetic showers are indicated in the left picture. The hadronic showers are indicated in the right picture.

hadronic showers. The showers and the two stages of the calorimeter are shown on figure 4.1.

In the following the responses of the calorimeter components to an incoming particle are demonstrated in the Monte Carlo using isolated single particles between 5 and 10 GeV. This corresponds roughly to the energy of high energetic particles in jets at our center of mass energy. To get such a sample $Z \rightarrow \tau^+\tau^-$ Monte Carlo events are taken. The 1-prong decays are divided into electron, muons and hadronic particles in the above defined energy range, to be independent as much as possible from the spectrum of the different species in the τ decay. Events with initial state bremsstrahlung and bremsstrahlung of the τ lepton are vetoed on the generator level.

The different shower types can be described by some typical variables.

- The energy in the BGO or the energy in the 9 central crystals, E9, respectively.
- The ratio of E9 over the sum of the 25 central crystals, E25, which was already shown in chapter 3.2.
- The number of crystals in the shower.
- The energy in the hadron calorimeter associated to the BGO cluster in a 50 mrad cone.
- For charged particles, namely the electron identification, also the matching between the track and the center of gravity of the energy deposit of the shower is a good variable. The matching is the difference in ϕ between track and the center of gravity of the shower. The ϕ of the track is taken at the entry point into the BGO.

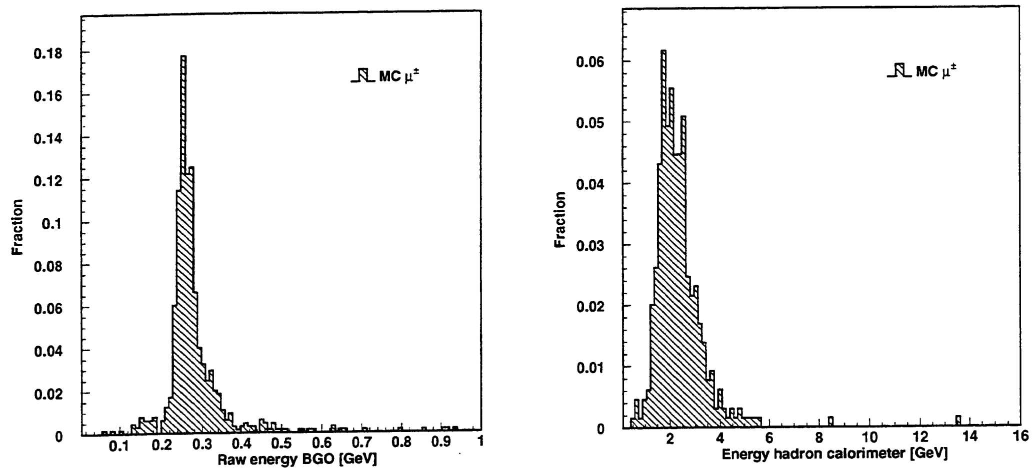

Figure 4.2: The energy deposit of muons in the BGO and in the hadron calorimeter. The input energy is between 5 and 10 GeV. Seen is the peak of minimum ionising particles between 220 and 240 MeV in BGO and roughly 2.5GeV in the hadron calorimeter.

The first class of particles to be discussed are the muons. They are minimum ionising in the BGO as well as in the hadron calorimeter. In figure 4.2 the normalised distributions of the measured raw energy in the BGO and the hadron calorimeter is shown. The energy deposit is between 220 and 240 MeV in the BGO and roughly 2.5GeV in the hadron calorimeter. Minimum ionising means also that these particles occupy normally only a few crystals, in 72.5% of the cases one crystal and in 93.1% less equal two crystals. So the ratio E9/E25 is one or in the case that a correction to these energy is applied as discussed below greater than one.

The next class are the pure electromagnetic showers. As an example electrons are taken. These particles produce a shower by bremsstrahlung and pair production, as described above, only in the BGO, since after 22 radiation length normally the whole electromagnetic shower is absorbed. Around 75% of the energy is deposited in the central crystal, 93% in the central 9 and 96% in the central 25 [62], if the impact is at the center of the central crystal. A correction for a shifted impact point is applied. To quantify the shift, the ratio of the energy of the central crystal E1 over E9 is taken. This correction is obtained using test beam data [56] and is only valid for purely electromagnetic showers. It corrects E9 and E25 to $E9_{corr}$ and $E25_{corr}$ and is the reason, why the ratio E9/E25 can become greater than one. All figures presented here are obtained with $E9_{corr}$ and $E25_{corr}$, the index will be dropped in the following.

The distribution of the energy sums E1, E9 and E25 already indicates that electromagnetic showers are narrow. This is quantified with the ratio E9/E25 being near one. The normalised distribution of this quantity is shown in figure 4.3. The two electrons outside the peak could be due to the small gap between the barrel halfs. Figure 4.4 shows the normalised distribution of the number of crystals

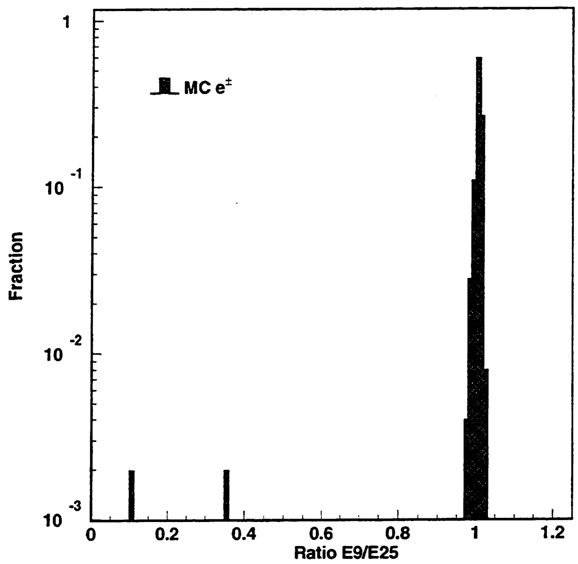

Figure 4.3: The ratio E9/E25 of the electron clusters, which peaks around 1.0.

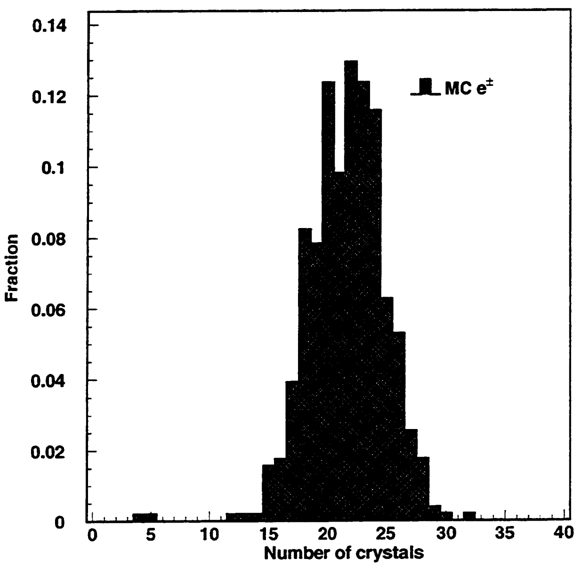

Figure 4.4: The number of crystals in an electromagnetic shower.

for each electron cluster in the BGO. It shows that even though the shower is narrow concerning the energy deposit, still in the average 20 to 25 crystals are in the cluster. This is due to the very low threshold energy (50 MeV) required to register meaningful energy deposit in a single crystal. The advantage of the low threshold is that also low energetic photons ($\approx 100 MeV$) can be measured.

The more complicated case is the incoming hadron. There exists three different shower types,

- minimum ionising in the BGO and full shower in the hadron calorimeter,
- charge exchange with a nucleus in the BGO and the decay of the remaining π^0 into photons, producing an electromagnetic shower,
- nuclear interaction with a nucleus of a BGO molecule, which then produces a hadronic shower already in the BGO and also in the hadron calorimeter.

The BGO has one nuclear interaction length, as a consequence only roughly one third of the incoming hadrons belong to the first class of minimum ionising particles in the BGO. The charge exchange reaction can happen anywhere in the crystal, so also this class has not to have the shower maximum and spread at the same place as an electromagnetic shower. Therefore we will only distinguish here between minimum ionising hadrons in the BGO and those which interact with the BGO material.

Figure 4.5 shows the normalised E9/E25 distribution of these showers. The distribution is broad. Around one, one finds the hadrons which produce similar showers as the electrons and photons due to charge exchange when entering into the crystal. Especially the values greater than one are produced by minimum ionising particles. Finally the tail of the distribution is produced by showers due to either charge exchange later on in the crystal or nuclear interaction. For hadrons without a shower in the BGO, which could be due either to the crack between BGO barrel and BGO endcap or the small crack at $|\cos\theta| = 0$, the ratio is set to zero.

The number of crystals, the normalised distribution is shown in figure 4.6, also shows the two classes. The minimum ionising particles are peaking sharply at one crystal for a cluster and then a second broad distribution with a maximum between 10 and 20 crystals is visible. If the distribution is integrated from zero to 5 crystals, roughly one third of the hadrons are in the peak, which is the expected behaviour. For hadrons without a shower in the BGO, the number of crystals is zero.

The spread of the energy measurement is also broad; this is visible in the distribution of the raw energy seen in the hadron calorimeter in figure 4.7. The raw energy is the energy as measured from detector online without any additional correction. This distribution is normalised to the number of all incoming hadrons in the sample. So the integral of the fractions shown in the figure represents 42% of the incoming hadrons, the shower of other particles are already stopped in the BGO. Remind that the input energy for these examples is between 5 and 10 GeV, the rate of stopped showers in the BGO for hadrons is energy dependent.

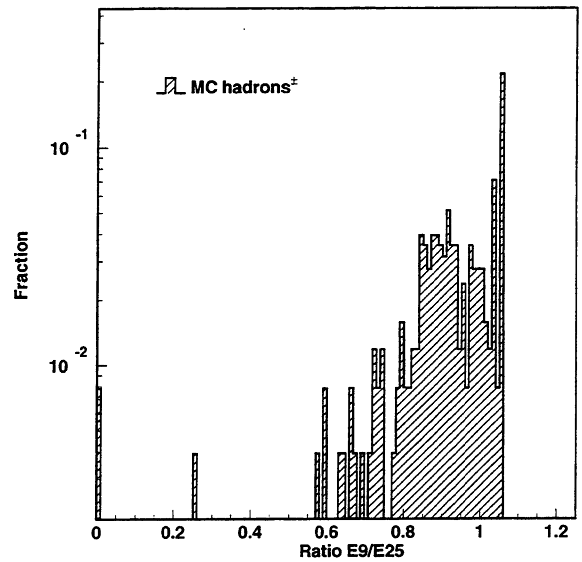

Figure 4.5: The ratio E9/E25 of clusters due to incoming hadrons.

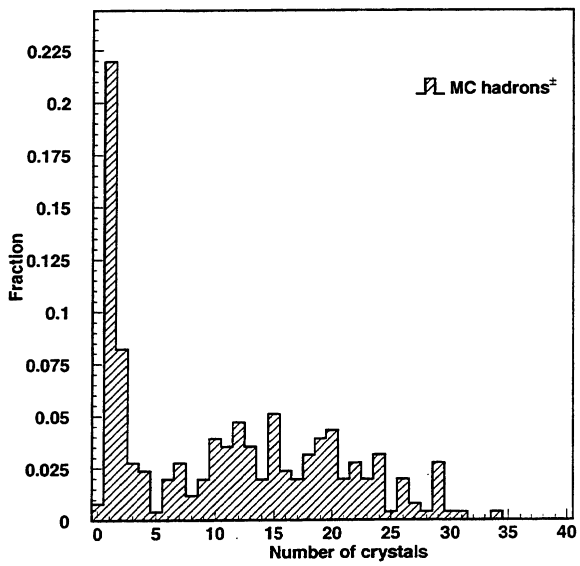

Figure 4.6: The number of crystals for each cluster of incoming hadrons.

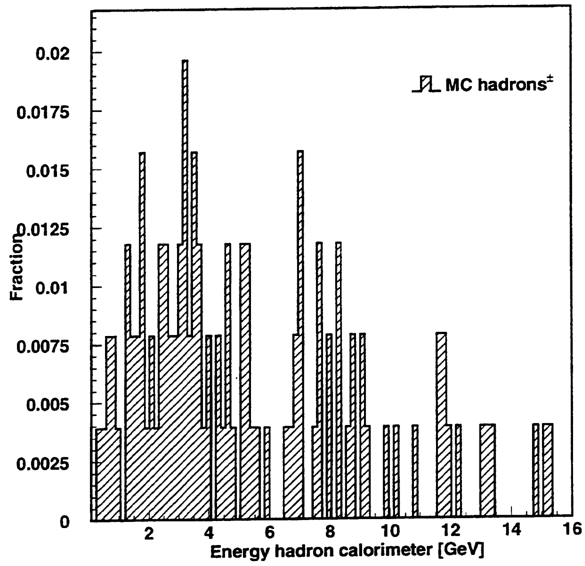

Figure 4.7: The raw energy deposit for each cluster of incoming hadrons.

How well data are described by the Monte Carlo was already shown in the previous chapter 3.2 in context with the electron identification. In the distribution of E9/E25 in figure 3.8 agreement between data and Monte Carlo can be seen, with a misdescription only in the peak bin. Especially the tail indicates a reasonable description of the shower shapes by the Monte Carlo. The distributions of the energy deposit in figure 3.10 and 3.11 show a good description of the response with a slightly lower efficiency for small energies.

4.1.2 Noise reduction

The first step which is done before the jet energy calibration is the identification of noise. As the jet energy is the integral of the particle energies, the noise is a small contribution to the overall resolution. As the aim is however also to measure large missing energy where noise gains in importance, it should be kept to the lowest level possible.

Since the hadron calorimeter is made of uranium plates which emit noise due to their natural radioactivity, the amount of noise is included in the simulation. In the electromagnetic calorimeter, noise is in principal taken out by the reconstruction. High energy noise is rare and is created mainly by hadrons starting to shower directly in front of the photodiodes. Low energy noise is taken out by pedestal subtraction and due to the pattern recognition which only starts to build clusters when at least one crystal has more than 50 MeV. If a noisy crystal has more energy than this threshold, a whole noise cluster can be built. The source of this noise is the readout electronics.

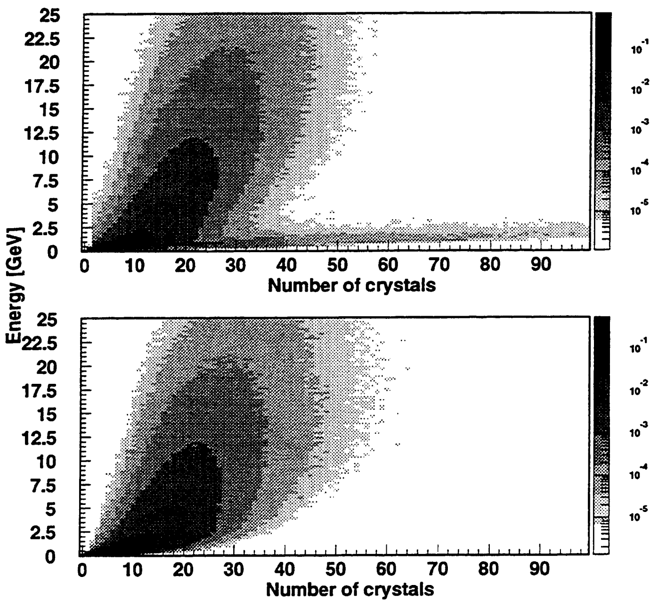

Figure 4.8: Low energy noise in the BGO, seen in the comparison between Data (upper plot) and Monte Carlo (lower plot). The gray scale indicates the normalized number of events.

The low energy noise in the BGO can sum up to 2 GeV. It can be identified by comparing data and Monte Carlo, which does not include this noise. This is visible in the distribution of the energy deposit in the BGO of the cluster in dependence on the number of crystals in the cluster, figure 4.8. In this distribution the noise is seen for large numbers of crystals (> 30) and low energy (< 1GeV), where the data show a tail which is not present in the Monte Carlo distribution. The following criteria are used for the identification:

- The number of crystals is larger than $20 + 10 \cdot E$, where the energy E is the energy of the BGO cluster in GeV,
- or the number of crystals is greater than $30 + 10 \cdot E_9$, where E_9 is the energy of the 9 central crystals of the cluster in GeV,
- or there is less than 500 MeV in the central cluster and the number of crystals is greater than 25 and the energy in the surrounding 8 crystals is less than 200 MeV.

Figure 4.9 shows the distribution of the energy of the 8 crystals surrounding the most energetic crystal in dependence on the total number of crystals in the cluster. In the distribution the most energetic crystal has less than 150 MeV. For the data the distribution is populated, while for the Monte Carlo the distribution is essentially empty. The data clusters are therefore identified as noisy. Similar distributions can be observed in the case of more energy in the central area of the cluster, if one takes the average energy further away from the central crystals. This leads to a further classification of clusters:

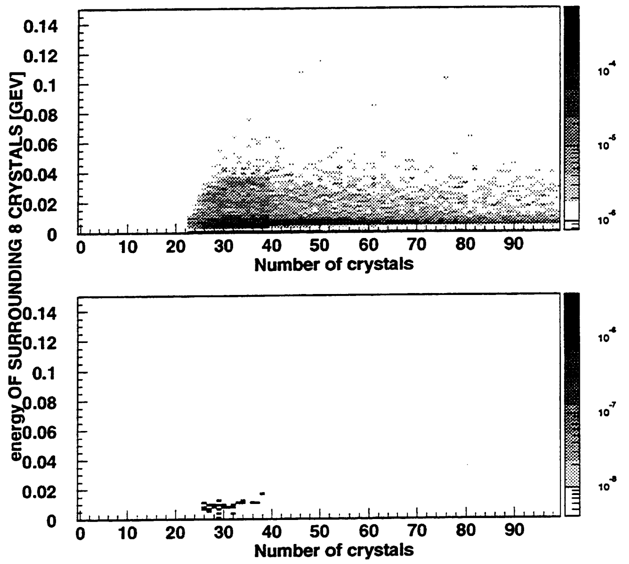

Figure 4.9: The average energy of the 8 crystals surrounding the most energetic crystal. The data are shown in the upper plot and the Monte Carlo in the lower plot. The gray scale indicates the normalised number of events.

- If the central crystal contains less than 150 MeV and the average energy in the surrounding 8 crystals is less then 35 MeV, the whole cluster is classified as noise.

- If the central crystal has more than 150 MeV and the 16 crystals which surround the central 9 have an average energy less than 35 MeV, a minimum ionising particle is assumed and the central one is kept as cluster.

- If the central crystal has more than 150 MeV and the 16 crystals surrounding the central 9 have an average energy more than 35 MeV, the cluster is assumed to be a soft electromagnetic shower. If the average energy in the crystals surrounding the central 25 crystals is less than 35 MeV, they are cut out, because they are identified as noisy.

High energy noise in the BGO can fake an unphysical shower shape for true electromagnetic clusters. Such showers are identified by comparing the ratio E1/E9 of the energy of the central crystal, E1, over the energy of the 9 central crystals, E9, which indicates the shower shape, with the energy in the central crystal E1. As can be seen in figure 4.10, the combination of high values of this ratio with high values of the energy in the central crystal is overpopulated if one compares data and Monte Carlo. If the ratio exceeds 0.96, the cluster is classified as noise.

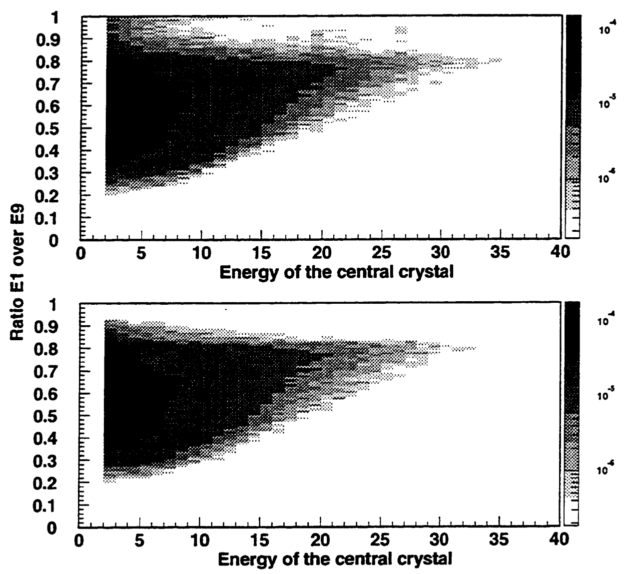

Figure 4.10: The ratio of the energy in the central crystal over the energy in the 9 central crystals versus the energy in the central crystal. For values larger the 0.96 in the ratio an excess in the data can be seen.

4.1.3 Jet energy calibration

The hadron calorimeter must be corrected for geometrical effects like the different amount of cracks and passive material in dependency of the azimuthal angle θ. The first correction is applied using muons, which are minimum ionising particles for the hadron calorimeter, as discussed above. The $|\cos\theta|$ dependency of the calorimeter response is calibrated out with the requirement that dimuon events give, as function of $|\cos\theta|$, always the same average energy deposit per path length in the hadron calorimeter. However the geometrical structure can still be seen in the weighted energy distribution of the clusters in $|\cos\theta|$, as shown in the upper plot of figure 4.11. There the module structure is seen for example at $\cos\theta \approx \pm 0.2$ and also at the edge of the barrel.

Up to this stage including the noise corrections and in the discussion of the showers in chapter 4.1.1 only particles or single clusters have been treated. All corrections from this point on are on a jet by jet basis. In the calibration process all jet energy spectra are fitted with a Gaussian function in the bulk and high energy tail between 40 and 65 GeV, to obtain the energy scale and the resolution of the jets independently of the neutrino spectrum. Therefore all quoted mean energies or scales and standard deviations of the mean or scale should be read as mean and sigma of a Gaussian fit between 40 and 65 GeV if not stated otherwise.

Such a fit to the energy distribution of jets in two jet like events is shown in figure 4.12. The high tail of distribution which is the part above the peak value is only caused by the resolution of the detector. It can be seen that in this case the resolution is highly gaussian, since the data are well fitted up to 60GeV by the gaussian function. The low tail where a "shoulder" comes out of the gaussian

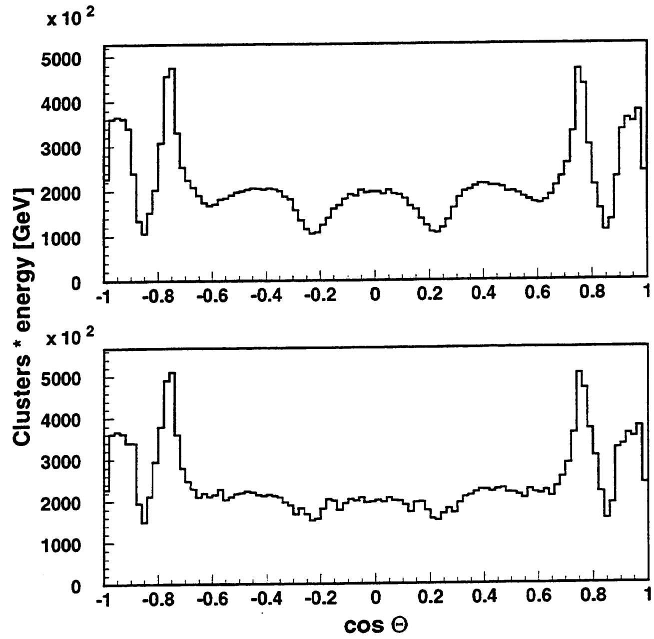

Figure 4.11: The energy weighted clusters in cosine of the polar angle θ. At $\approx \pm 0.2$ the boundary of the modules can be seen also at larger values the boundaries to the outer modules and the transition from the barrel to the endcaps. The upper plot is before the additional $|\cos\theta|$ correction, the lower plot is with the additional correction.

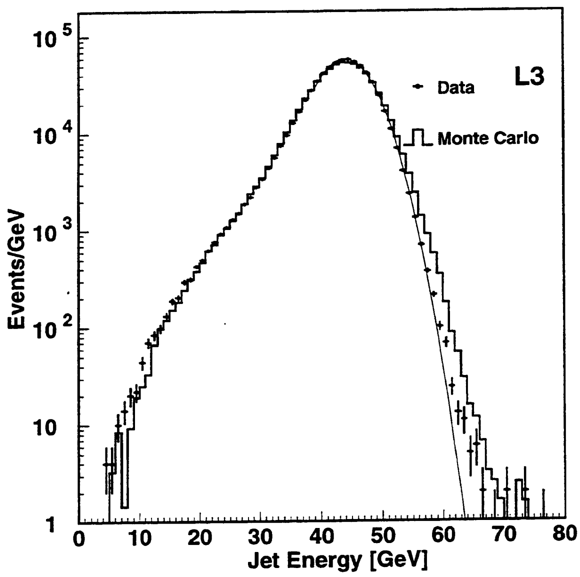

Figure 4.12: The visible energy spectrum for each jet in the two jet sample, note the difference in the resolution as seen on the high side of the spectrum. A gaussian fit in the range between 40 and 65 GeV to the data is also shown.

	Data		MC	
	$+\cos\theta$	$-\cos\theta$	$+\cos\theta$	$-\cos\theta$
$\mid\cos\theta\mid$	$<E>$ [GeV]	$<E>$ [GeV]	$<E>$ [GeV]	$<E>$ [GeV]
0.00-0.05	43.89 ± 0.028	43.90 ± 0.04	43.63 ± 0.045	43.63 ± 0.043
0.05-0.15	43.87 ± 0.017	44.00 ± 0.018	43.73 ± 0.031	43.85 ± 0.028
0.15-0.30	43.69 ± 0.020	44.01 ± 0.027	43.98 ± 0.028	44.07 ± 0.026
0.30-0.45	43.97 ± 0.014	44.19 ± 0.013	43.82 ± 0.023	43.91 ± 0.022
0.45-0.65	43.72 ± 0.015	43.93 ± 0.013	44.08 ± 0.023	44.23 ± 0.022
0.65-0.73	42.79 ± 0.040	42.92 ± 0.037	43.65 ± 0.042	43.88 ± 0.040

Table 4.1: The average energy per jet and $\cos\theta$ for data and Monte Carlo after the calibration process. The average was taken by fitting the high part of the visible energy spectrum between 40 and 65 GeV and taking the mean of the gaussian as average. The error is the error of the fit. It is visible that the Monte Carlo reproduces well the geometrical dependency of the response.

distribution is due to neutrinos. The fit range covers not only the high tail but also roughly one standard deviation into the low tail, such that a nearly neutrino independent determination of the mean of the gaussian can be determined. This mean quantifies the average energy deposit, if no neutrino is present, and therefore the scale of the energy response.

On this jet by jet basis, first geometrical corrections are applied. Since the BGO has a very homogenous response all the geometrical corrections can be applied to the energy measured in the hadron calorimeter. It is then also independent from the actual ansatz, how to combine the two measurements in the BGO and in the hadron calorimeter for a jet, which are described later on.

Before the calibration process handles the remaining $|\cos\theta|$ dependence the energy response in the 16 ϕ modules of each ring is equalized. This is done with the requirement that the average energy deposit of jets in the calorimeter is independent of ϕ. After this correction a final correction in $\cos\theta$ is performed. The requirement is that the energy scale of the energy distribution is the same for the same $\cos\theta$ range in data and Monte Carlo. This is shown in table 4.1. As can be seen in this table the calibration is stable up to 200 MeV difference between data and Monte Carlo in each $\cos\theta$ range. Consequently the remaining inhomogenity of the response is within the error described by the Monte Carlo. The energy weighted distribution of the clusters after these corrections can be seen in the lower plot of figure 4.11. Compared with the upper plot which contains only the corrections obtained from the muons only, an improvement is visible especially at the module boundaries.

At this stage the detector components are corrected for cracks, dead material, noise and the jets are measured as a whole in the calorimeter system. A parametrisation for the jet energy would then be

$$E_{Jet} = \alpha E^{raw}_{BGO} + \beta E^{raw}_{hcal} \tag{4.1}$$

where β is a function of ϕ and θ containing the corrections described before and α is an average correction which absorbs the average electromagnetic energy

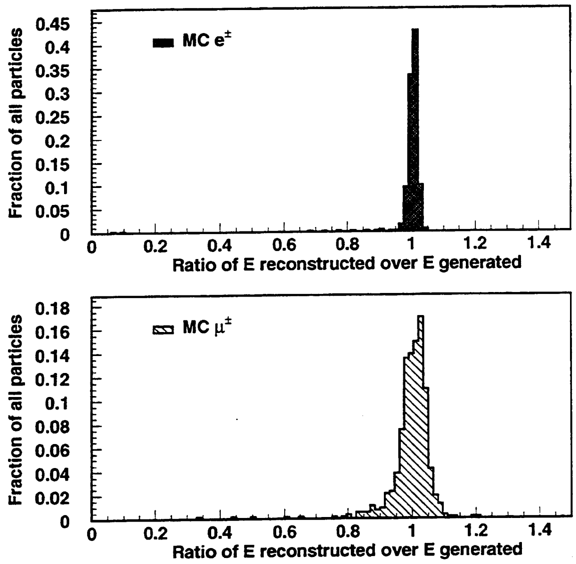

Figure 4.13: The resolution in the BGO and the muon chamber for electron and muons respectively. This is again made with the single particle sample between 5-10 GeV. With a gaussian fit a resolution of 1.3% for the electrons and 3.5% for the muons is obtained.

deposit of the jet as well as the average hadronic energy deposit in the BGO. This ansatz was used in several analysis in L3 without the additional ϕ and θ correction obtained with jets. The factors α and β are also called G-factors and for the old method documented in [63] and [64].

The calorimeter should give then a homogeneous response. However, the energy dependence of the response remains uncorrected, since for low energetic jets which contain also low energetic particles the share of the energy deposit in the BGO increases relative to the deposit in the hadron calorimeter. Also the full use of the excellent resolution in the BGO and the muon chambers has not yet been made. In the figure 4.13 the ratio of reconstructed energy of the single particles over the generated energy range is shown for the Monte Carlo electron and muon sample described in subsection 4.1.1, which demonstrates the good resolution of detector components for electron, photons and muons. The theoretical resolution would be between 3.2 and 3.5 GeV/jet for two jet like events taking the values given in the detector chapter 2 obtained from test beam data and identifying correctly all particles. This depends on the fraction of π^0 and η in the jet, since only the photons from the decays are measured.

To achieve the goal of making best use of BGO and muon chambers, the step to be done is the subtraction of well measured isolated electromagnetic cluster and well measured muons from the jet, so that only the remaining energy measurement has to be corrected for sharing between BGO and hadron calorimeter. The ansatz is

$$E_{Jet} = E_{\gamma} + E_{\mu} + \alpha' E_{BGO}^{remaining} + \beta' E_{hcal}^{remaining} \,, \tag{4.2}$$

which is a refined form of equation 4.1.

The quantities of equation 4.2 will be explained in more detail. For every well measured muon candidate the average energy loss $< E_{\mu}^{loss} >$ of a minimum ionising particle in the hadron calorimeter is subtracted from the energy measured in the hadron calorimeter, and the momentum measured in the muon chambers is used to obtain its energy. The sum of all well measured energies of muon candidates is E_{μ} and the remaining energy in the hadron calorimeter is

$$E_{hcal}^{remaining} = E_{hcal}^{raw} - n_{\mu} < E_{\mu}^{loss} > \tag{4.3}$$

Using a ratio of E9 over E25 larger than 0.95 and asking for at least 4 crystals to distinguish between electromagnetic showers and hadronic showers for isolated clusters, the electromagnetic energy E_{γ} is subtracted. So an amount of remaining energy $E_{BGO}^{remaining}$ in the BGO is left over. The total remaining energy $E_{total}^{remaining}$ which is the sum of $E_{BGO}^{remaining}$ and $E_{hcal}^{remaining}$ is used to parameterise the correction needed to obtain the jet energy. This leads then finally to equation 4.2.

$$E_{Jet} = E_{\gamma} + E_{\mu} + \alpha' E_{BGO}^{remaining} + \beta' E_{hcal}^{remaining} \ ,$$

where the corrections α' and β' are functions of $E_{total}^{remaining}$ and β' contains also the ϕ and θ corrections. The first two terms represent the precise measured energy from BGO and muon chambers, the last two terms represent the real hadronic part of the jet. That this correction is dependent of the remaining total energy should compensate for the different energy share in the two detectors for low energetic jets.

With this ansatz a resolution of 4.6 GeV/jet in the Monte Carlo for two jet like events is obtained. For the data the resolution is found to be 4.2 GeV/jet. The visible energy spectrum of data and Monte Carlo is compared in figure 4.12. The different resolution is seen in the high tail of the distribution.

Figure 4.14 compares this new method with the old ansatz presented in 4.1. The comparison is done for two jet like events. In contrast to figure 4.12 the distribution of the visible energy of the whole event and not for each jet is shown. The mean of both distributions is adjusted to E_{CM}. How to chose the scale for this measurement is described in the next section. Clearly the new method gives a narrower distribution which shows gaussian behaviour which can be seen by the line indicating the fit result.

4.2 Energy scale determination

Since the neutrino energy is seen as missing energy in a hemisphere, a jet energy calibration should be chosen such as to correctly reproduce the visible energy with its scale. This reduces biases in the spectrum after applying selection cuts to the events. The correctness of the scale guarantees also that the calibration is independent of the average neutrino energy and the amount of cracks in the detector.

As a constraint to obtain the correct scale, a condition is chosen such that the average missing energy equals the average generated neutrino energy in the Monte

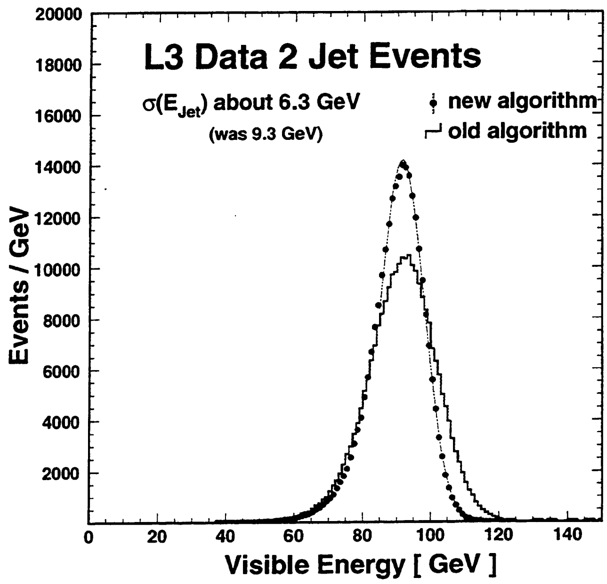

Figure 4.14: The visible energy spectrum of the whole event. Shown are the distributions for the new method and the old method. The line through the dots indicates the result of a gaussian fit, which is performed to the high tail of the distribution in the range between 84 and 106.5 GeV.

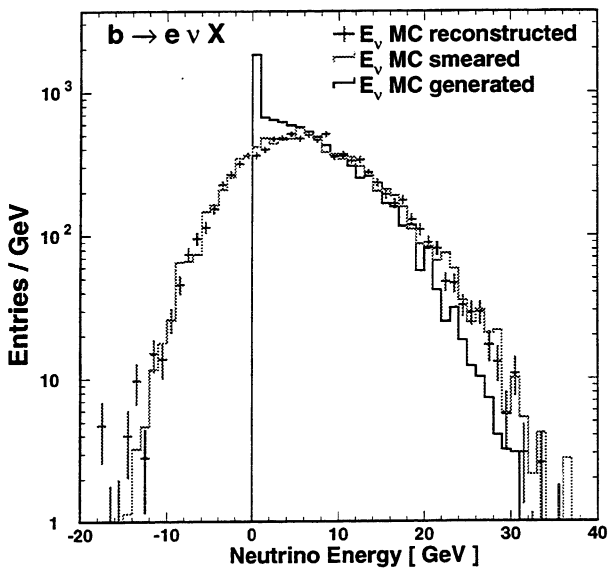

Figure 4.15: Comparison of the generated missing energy spectrum, with gaussian smeared one and the reconstructed spectrum for tagged b $\rightarrow e\nu X$ candidates.

Carlo. As shown in figure 4.12 the high tail of the distribution, which determines the resolution, is gaussian.

If the resolution is purely gaussian, the generated spectrum smeared with a gaussian resolution function should be in agreement with the reconstructed missing energy spectrum in the Monte Carlo. That this is the case can be seen in figure 4.15 after the scale was chosen with the constraint given above. Here the missing energy spectrum of electron tagged Monte Carlo hemispheres, the reconstructed energy, is compared with the gaussian smeared generated neutrino energy. The generated spectrum is also shown. The remaining background events produce a peak at zero energy in the generated neutrino spectrum. The smeared spectrum is produced with a σ of 4.6 GeV obtained from the fit to the Monte Carlo jet energy spectrum shown in figure 4.12. This smeared spectrum describes the reconstructed one well. The conclusion is that the missing energy spectrum with the chosen scale reproduces the neutrino spectrum with the given gaussian resolution.

The data are then calibrated relatively to the scale obtained in the Monte Carlo. This could be done with a 10 MeV precision. The calibration is checked with the b depleted and b enriched samples described in chapter 3. Comparing data

Sample	Monte Carlo [Gev]	Data [Gev]	ΔE(Data-Monte Carlo) [MeV]
2–Jet	43.95 ± 0.006	43.96 ± 0.005	$+10 \pm 8$
lifetime	43.51 ± 0.021	43.66 ± 0.029	$+150 \pm 36$
lepton	43.25 ± 0.047	43.30 ± 0.051	$+50 \pm 69$
anti-lifetime	44.25 ± 0.011	44.22 ± 0.010	-30 ± 15
high X	44.32 ± 0.028	44.33 ± 0.038	$+10 \pm 47$

Table 4.2: The result of mean energy obtained by the Gaussian fits between 40 and 65 GeV for the different samples in data and Monte Carlo.

and Monte Carlo, the uncertainty in the determination of the energy scale is estimated. For the b-depleted samples the energy scales agree within 30 MeV and for the b-enriched sample within 150 MeV for the high statistics lifetime sample and within 50 MeV for the high purity lepton sample as shown in table 4.2 and the distributions in figure 4.16 and figure 4.17. respectively. Note that the fit should not be sensitive to the differences in the low energetic tail of the spectra and should take into account the different resolutions seen in the distributions.

The difference observed in the b-enriched samples could be due to the differences in the charm sector or in a different flavour dependent detector response between data and Monte Carlo. Since the neutrino measurements will be done in the lifetime enriched sample and the reason for this discrepancy is not yet clear, 150 MeV are taken conservatively as a systematic error on the energy scale.

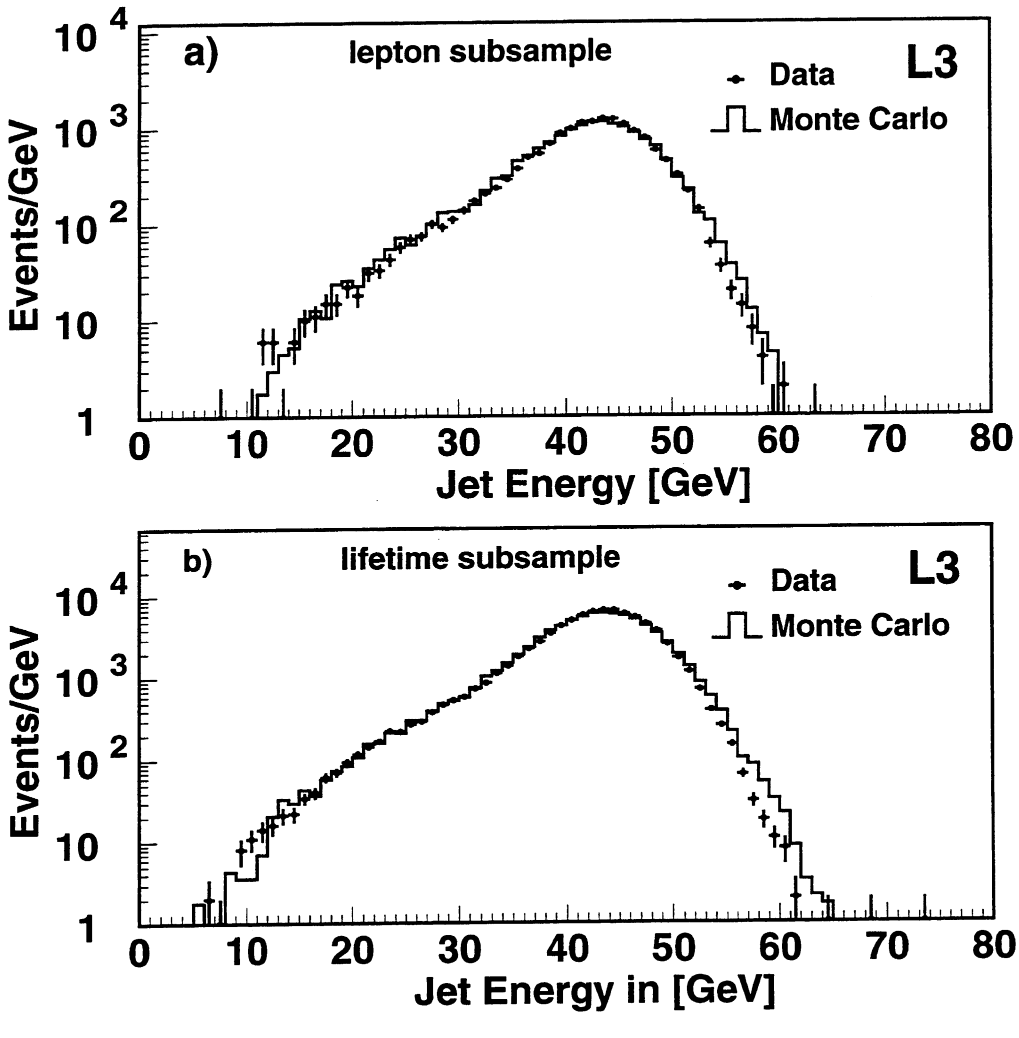

Figure 4.16: The visible energy spectrum of the b-enriched samples in data and Monte Carlo. Like in the full two jet sample the difference in the resolution is visible on the high side, so the agreement on the low energetic side means a relative higher fraction of low energy events in the data compared with the Monte Carlo.

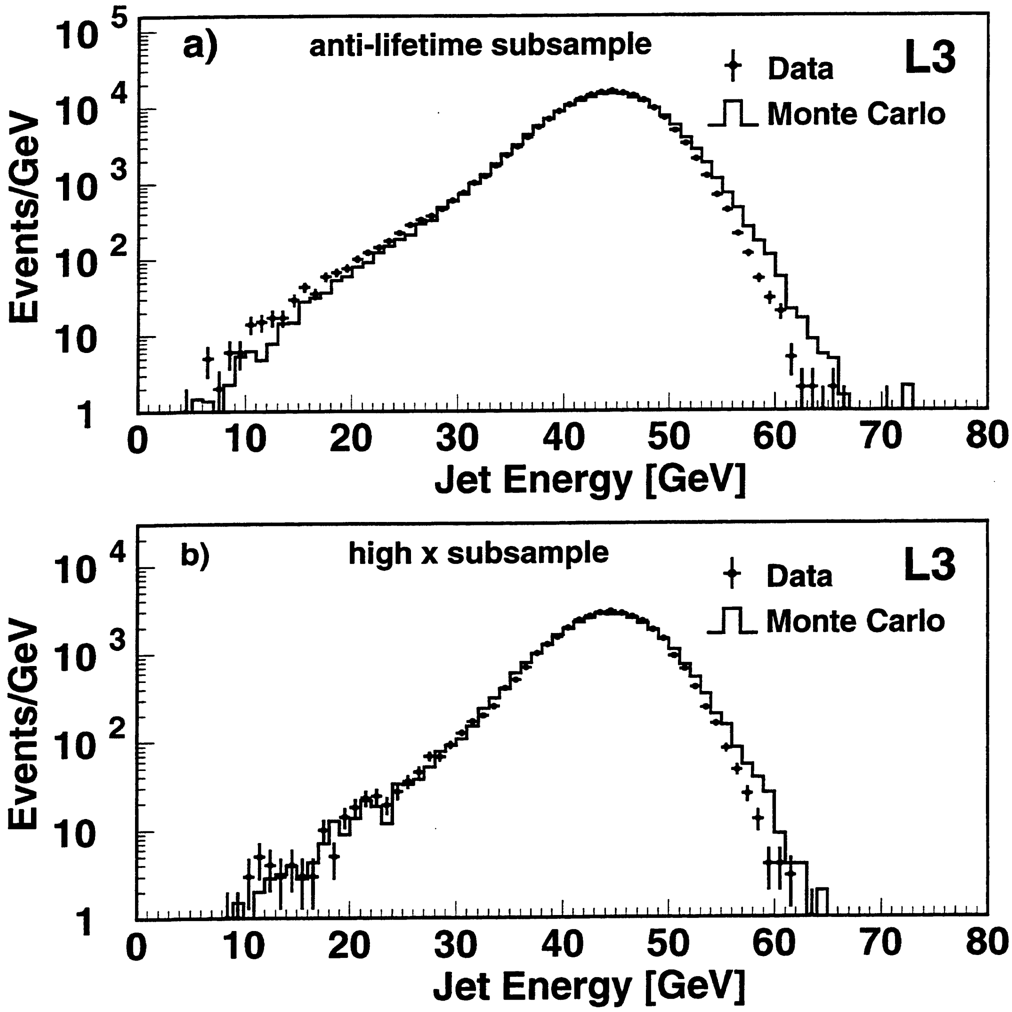

Figure 4.17: The visible energy spectrum of the b-depleted samples in data and Monte Carlo. Especially in the anti-lifetime sample (a) the enhancement of the low energetic tail in the data is clearly visible. Since this should not be due to b-jets, it is concluded that the Monte Carlo does not describe correctly the low energy background. This is also a reason why in the measurements, described later, the background is determined mostly with the data.

Chapter 5

Measurements and Results

As stated already before, the neutrino energy is measured in a two jet sample using the relation $E_\nu \approx E_{beam} - E_{Jet}$. This relation assumes that the jet in each hemisphere is coming from the primary quark, and since on the Z-pole initial state radiation can be neglected, each quark has the beam energy. Therefore all measurements are made using the two jet sample, where the jets are defined as stated in chapter 3.1.

In the beginning of this chapter the common Monte Carlo parameters for all measurements and the fragmentation scheme used with its systematics will be presented. In the following section the branching ratio b $\rightarrow$ eνX and b $\rightarrow$ $\mu\nu$X is studied. Since the number of electron and muon candidates are counted, it is a direct measurement of the branching ratio in contrast to the measurement using the missing energy. In principle this measurements could also be done without the restriction of a two jet sample, but it is performed with this requirement to be comparable with the b $\rightarrow$ νX measurement. Another reason is, that the results are also used in the b $\rightarrow$ $\tau\nu$X measurement, which is again a missing energy analysis using two jet events. The effect of this restriction is discussed separately. Then the measurement of the decay structure, i.e. the polarisation of the virtual W, is presented. There the neutrino momentum spectrum of the data is compared with the neutrino spectrum predicted by different models. According to the method proposed in [39] the charged lepton spectrum for all models in question is adjusted to the one given by the data. The neutrino momentum is given by the missing energy on the lepton tag side, and is interpreted as the electron neutrino and muon neutrino spectrum respectively. Finally, the inclusive neutrino branching ratio will be presented, which is in contrast to the V–A test, a measurement independent of the presence of a charged lepton. But, under the assumption that for each neutrino a charged lepton is produced, also an indirect test of the total branching ratio b $\rightarrow$ $\ell^\pm\nu$X is provided. This measurement is repeated taking the measurements of the branching ratio b $\rightarrow$ eνX and b $\rightarrow$ $\mu\nu$X as an input to obtain b $\rightarrow$ $\tau\nu$X.

5.1 Monte Carlo parameters and fragmentation function

The Monte Carlo events are generated using JETSET7.3 [42] [43] with the parton shower approximation for gluon radiation and string fragmentation. The detector is simulated using a GEANT based description of the L3 experiment [65]. The weak decays of c and b-hadrons are simulated such that the experimental charged lepton spectra and branching ratios are reproduced [22] [66] [67] [68]. A (V+A)$\times$(V–A) structure is used for the decays c $\to \ell\nu$X. The exclusive branching ratios for $D^0 \to K(K^*)\ell\nu$ are 3.8%(2.4%) for the three body decay and 0.8 % for the multibody decays, the corresponding values for the exclusive D^+ decays are 9.8%(6.2%) and 2% respectively. The semileptonic branching ratio of b-hadrons into charged leptons is 10.45% with the different decays of $B \to D, D^*$ and D^{**} taken to represent 2.0%, 5.3% and 3.0%, respectively. The fraction of $b \to u\ell\nu$ is 0.15%.

The events are simulated using the Peterson fragmentation function [46], the ACCMM-model [29] and the string fragmentation algorithm, as stated above. The fragmentation parameter is adjusted such that the average relative energy of the weakly decaying b-hadron is $\bar{x}_E = 0.72$ of E_{Beam}. This value gives the best description of the lepton spectra in the data, as explained below.

The average momentum of the electron candidates in the data is with $\bar{x}_E = 0.72$ 180 ± 110MeV lower than in the Monte Carlo. For the muon candidates the average momentum is 180 ± 80MeV higher. The correlation is such that a 450MeV increase of the average b-hadron momentum gives an increase of 80 ± 20MeV in the average lepton momenta. If one tries to adjust the average momentum with the help of the branching ratio $b \to \ell\nu$X, the average momentum changes by -20 ± 10MeV for electron candidates and $+40 \pm 10$MeV for muon candidates with a 10% relative increase of the branching ratio. So the central value is stable against changes in the branching ratio, since it would increase the discrepancy between electron and muon candidates.

The uncertainty of the average energy $\bar{x}_E$ is given by the best description of individual lepton spectra, instead of the best average for both electron and muon spectrum. The electron spectrum is softer and provides a lower bound, the muon spectrum is harder and provides an upper bound. This leads to a value of $0.72 \pm 0.02 \cdot E_{beam}$. This value is somewhat larger than the one obtained recently from multiparameter fits to the p and $p_\perp$ of the electron and muon candidates, which is 0.70 [69]. The estimated uncertainty covers the value, but taking this as central value leads to a poorer description of the momentum spectra. The change in the decay model, as for example the ISGW-model [30] is also infolded in the estimate of the fragmentation function, since the net effect would be a harder or softer lepton spectrum, which can not be disentangled from the systematics of the fragmentation.

5.2 Direct measurement of the semileptonic branching ratio $\mathrm{B} \to \mathrm{e}(\mu)\nu\mathrm{X}$

In this section a measurement of the branching ratio of b-hadrons into prompt electrons and muons is described. The branching ratio is determined comparing the number of candidates in data and Monte Carlo for the studied process. Subtracting the background fraction[1]

$$n_{back} = \frac{\text{all background jets}}{\text{all hadron jets}} \tag{5.1}$$

given by the Monte Carlo from the fraction of lepton candidates

$$n_{\ell-\text{cand}} = \frac{\ell - \text{candidate jets}}{\text{all hadron jets}} \tag{5.2}$$

in the data, the fraction of prompt $\mathrm{b} \to \ell\nu\mathrm{X}$-jets

$$n^{Data}_{\ell-\text{jets}} = n^{Data}_{\ell-\text{cand}} - n_{back} \tag{5.3}$$

in the data is obtained. The branching ratio is then

$$Br(\mathrm{b} \to \ell\nu\mathrm{X})_{Data} = \frac{n^{Data}_{\ell-\text{jets}}}{n^{MC}_{\ell-\text{jets}}} Br(\mathrm{b} \to \ell\nu\mathrm{X})_{MC} \tag{5.4}$$

where $n^{MC}_{\ell-\text{jets}}$ is obtained analog to equation 5.3. In this method the efficiencies are estimated by the Monte Carlo and all excess observed is classified as signal.

The results are cross-checked with the lepton independent b-enriched and b-depleted tags. For the number of b-jets the Monte Carlo assumes the Standard Model value for $\mathrm{R_b}$ of 0.216.

5.2.1 Measurement with electrons

As described earlier in chapter 3.2, the electron candidates have a momentum larger than 3GeV. The criterion chosen to distinguish the $\mathrm{b} \to \mathrm{e}\nu\mathrm{X}$ candidates from the background is the $p_\perp$ criterion. The transverse momentum with respect to the nearest jet, $p_\perp$, has to be larger than 1.4GeV. It has to be assured that the remaining background is controlled by the Monte Carlo and the obtained result is independent of the cut chosen.

The transverse momentum spectrum for the electron candidates with a momentum of more than 3GeV is shown in figure 5.1a). This spectrum shows a significant enhancement relative to the Monte Carlo for low values of $p_\perp$. In the b-depleted sample, as seen in figure 5.1c) and table 5.1, this enhancement is even more pronounced. It is much less visible in the b-enriched lifetime sample, as seen in 5.1b). It is thus concluded that the enhancement is due to an underestimation of the background by the Monte Carlo, and that this deviation is not present in the

[1] The cascade decay $\mathrm{b} \to \mathrm{c} \to \ell\nu\mathrm{X}$ is part of the background, since only the prompt branching ratio $\mathrm{b} \to \ell^\pm\nu\mathrm{X}$ is measured.

$p_\perp$ in GeV	2–Jets	$(\frac{N_{candidates}}{N_{hadrons}})_{Data}/(\frac{N_{candidates}}{N_{hadrons}})_{MC}$ lifetime	anti-lifetime	high X
0.0-0.7	1.36 ± 0.07	1.04 ± 0.13	1.46 ± 0.16	1.57 ± 0.47
0.7-1.4	1.02 ± 0.03	1.03 ± 0.06	0.97 ± 0.07	0.85 ± 0.15
1.4-2.1	1.01 ± 0.03	1.06 ± 0.06	0.90 ± 0.07	0.76 ± 0.16
≥ 2.1	1.05 ± 0.03	0.96 ± 0.05	1.03 ± 0.06	0.87 ± 0.14

Table 5.1: Ratio Data vs. MC showing the $p_\perp$ dependency of the number of electron candidates for the different subsamples.

	Data	Monte Carlo		Data
$p_\perp$ [GeV]	$N_{e^\pm}/N_{had} \times 10^3$	$N_{e^\pm}/N_{had} \times 10^3$	purity b$\rightarrow e\nu X$ [%]	Br[%]
0.0–0.7	2.09±0.08	1.54±0.06	28.5	9.55±1.28
0.7–1.4	6.14±0.13	5.98±0.12	48.3	11.01±0.32
1.4–2.1	6.11±0.13	6.04±0.12	73.3	10.61±0.31
≥ 2.1	9.32±0.16	8.92±0.15	78.3	11.05±0.27
≥ 1.4	15.43±0.21	14.96±0.19	76.3	10.89±0.20

Table 5.2: The observed number of electron candidates per hadronic event in the data and in the Monte Carlo and the resulting Br(b$\rightarrow$ eνX) with the statistical errors are given for different $p_\perp$ values. A $p_\perp$ cut of 1.4 GeV is used to extract the final semileptonic branching ratio. For the Monte Carlo, with an input branching ratio of 10.45%, the purity of correctly identified semileptonic b–decays is also given.

signal region $p_\perp \geq 1.4$GeV. If this conclusion is true, it should be possible to correct the background in this range.

Using the anti-lifetime subsample a correction for the electron candidates with a $p_\perp$ below 0.7 GeV is obtained. The correction assumes that all excess seen here is due to non-b background events. A correction factor c is then given in the anti-lifetime subsample by

$$c = 1 + \frac{n^{Data}_{\text{e-cand}} - n^{MC}_{\text{e-cand}}}{n^{MC}_{\text{non b}}} \tag{5.5}$$

where the n are again fractions normalised to the number of hadronic jets. The corrected Monte Carlo predicted background fraction is then the fraction of b-background events plus c times the non-b fraction. With this correction the branching ratio in the range of $p_\perp < 0.7$ is 9.55 ± 1.28.

An overview of the values obtained for the different $p_\perp$ ranges can be found in table 5.2. For higher values of $p_\perp \geq 0.7$GeV, no evidence in the subsamples is found that the background might be false estimated with the Monte Carlo. Therefore in table 5.2 only the first bin is corrected. The corrected value for low $p_\perp$ is consistent with the other $p_\perp$ ranges. The main sources of systematic errors for this measurement are thus the fragmentation function, the uncertainty of the background, which includes the variation of $p_\perp$ and the two jet definition, which will be discussed later.

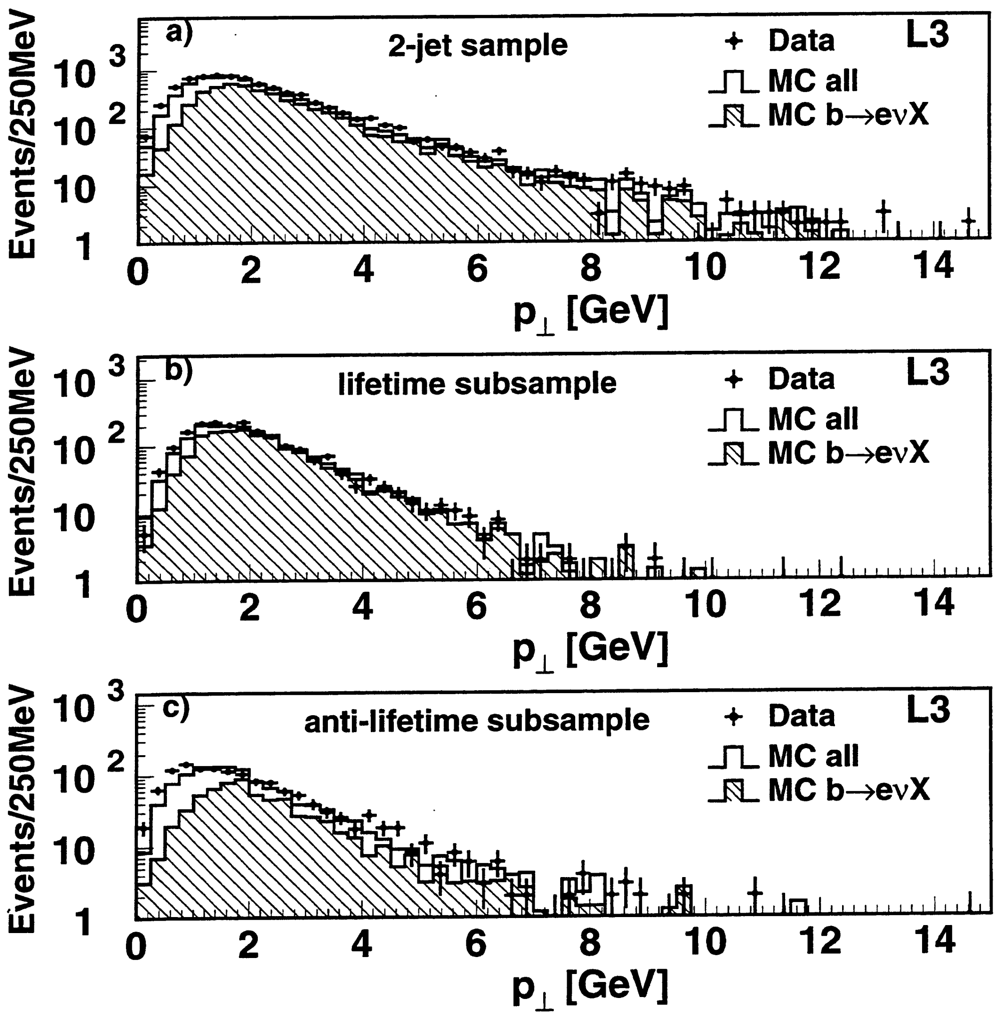

Figure 5.1: (a) The spectrum of $p_\perp$ with respect to the jet direction for the electron candidates in the two–jet sample, (b) in the b enriched lifetime sample and (c) in the b depleted anti-lifetime sample. The corresponding Monte Carlo distributions are also shown, together with the contribution of correctly identified semileptonic b–decays using a branching ratio of 10.45%. For low $p_\perp$ an enhancement in the data of the 2–Jet sample is observed which is not present in the b-enriched lifetime sample but even more pronounced in the b-depleted anti-lifetime sample.

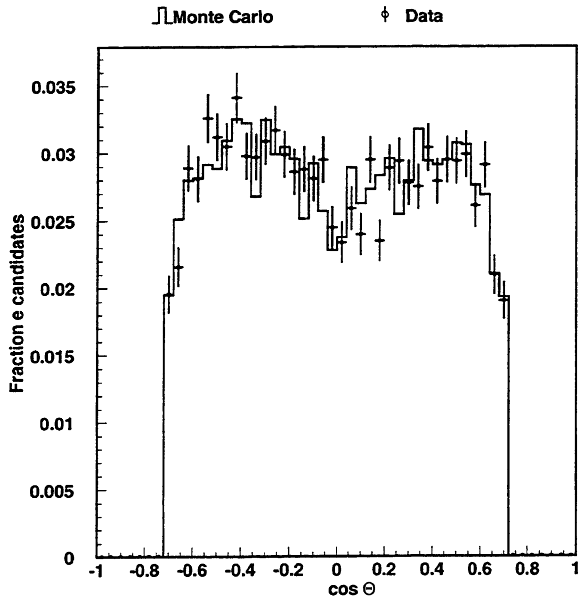

Figure 5.2: The $\cos\Theta$ distribution of the electron candidates. The observed asymmetry is due to a defective ring in the BGO during 1992 data taking.

Error source	Δ Br(b$\rightarrow$eνX) in %
selection efficiency	0.13
$p_\perp$ dependenc	0.28
semileptonic c-hadron decays	0.13
b-hadron momentum $< X_E >_b = 0.72 \pm 0.02$	0.25
two jet definition	0.29
total systematic error	0.51

Table 5.3: Estimated systematic errors for the branching ratio measurement of the high $p_\perp$ electrons.

The uncertainty due to semileptonic c-decays is estimated by a relative variation of $\pm 10\%$ of the decay branching fraction in the Monte Carlo. In figure 5.2 and 5.3 the description of the efficiency as a function of ϕ and $\cos\Theta$ is shown. These distributions are found to be in agreement with the Monte Carlo, the asymmetry seen in the $\cos\Theta$ distribution is due to a ring in the BGO which was not working during the 1992 data taking period. The error on the selection efficiency is quantified by a variation of the selection criteria, described in the event classification chapter 3.2. The systematic error due to the $p_\perp$ dependence is given by the variation seen when comparing the two subranges $1.4\text{GeV} \leq p_\perp < 2.1\text{GeV}$ and $p_\perp \geq 2.1\text{GeV}$ corresponding to the range where the central value is obtained. The errors are listed in table 5.3.

The momentum spectrum of the final sample in two $p_\perp$ ranges is shown in figure 5.4. The overall spectrum is well described. Only for low values of p a small discrepancy between data and Monte Carlo remains, which is more pronounced

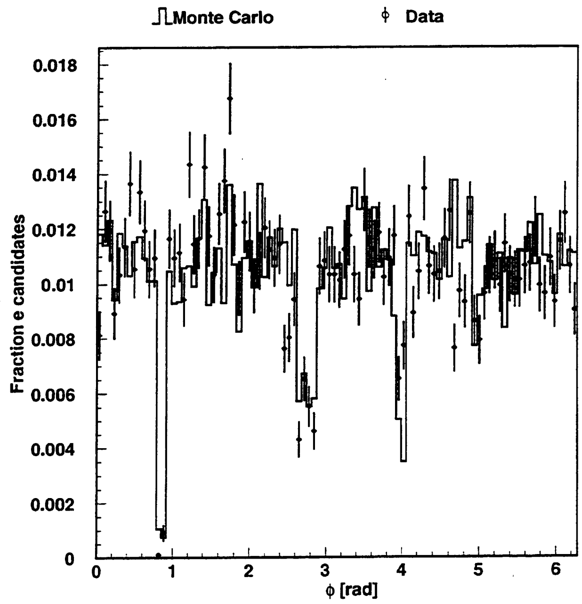

Figure 5.3: The ϕ distribution of the electron candidates. The distribution shows also the regions of the TEC chamber, where high quality tracks are only formed with reduced efficiency mainly due to grounding problems at the grids.

for the high $p_{\perp}$ range. Cutting out this region $p <$ 6GeV the central value for the branching ratio would decrease by 0.1%. The final result for the Br(b→eνX) obtained with the electron candidates with more than 1.4 GeV transverse momentum is

$$\mathrm{Br}(\mathrm{b} \rightarrow \mathrm{e}\nu\mathrm{X}) = 10.89 \pm 0.2 \pm 0.51\%$$

where the first error is statistical and the second one systematic.

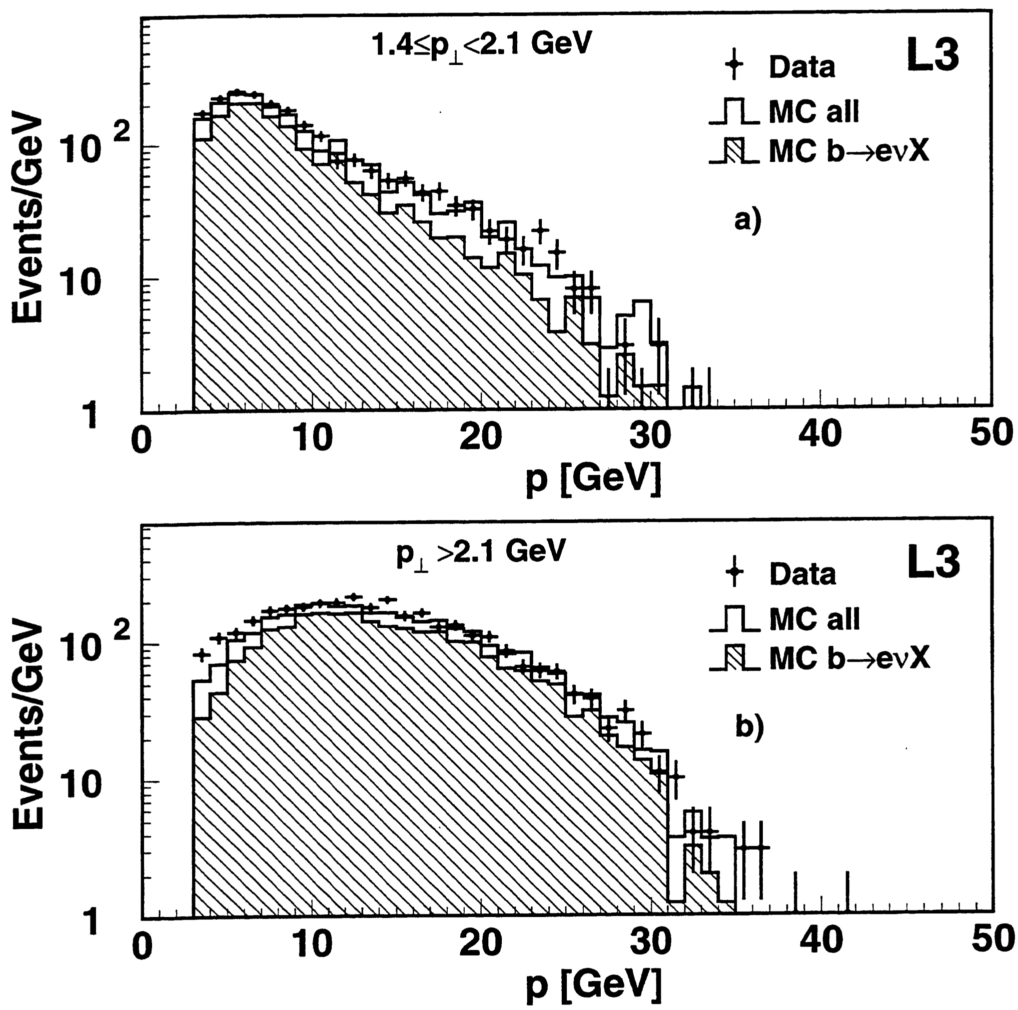

Figure 5.4: The momentum spectrum of the electron sample in two $p_\perp$ ranges corresponding to the final sample. The Monte Carlo distributions are normalised to the total number of hadrons in the data 2–jet sample.

5.2.2 Measurement with muons

Muon candidates have to have a momentum larger than 4 GeV as described in chapter 3. Like in the electron case, the criterion used to separate b $\rightarrow \mu\nu$X candidates from background is $p_\perp > 1.4$GeV. The $p_\perp$ spectrum of the muon candidates is shown in figure 5.5a). This spectrum is well described by the Monte Carlo also for the lifetime tagged b-enriched subsample, as shown in figure 5.5b) and for the b-depleted subsamples in figure 5.5c).

More quantitatively this is seen in table 5.4. In the lifetime subsample and in the anti-lifetime subsample the ratio of the fraction of candidates relative to all hadrons in data and Monte Carlo is stable within the errors. The conclusion is that the background in this measurement is well described by the Monte Carlo. However, in the spectra as well as in the table a small tendency towards an increase in the number of observed candidates for higher $p_\perp$ can be seen. In the discussion of the fragmentation function it was already argued, that the muon candidates appear to have a harder momentum spectrum compared with the Monte Carlo, which could explain the observed effect.

	$(\frac{N_{candidates}}{N_{hadrons}})_{Data}/(\frac{N_{candidates}}{N_{hadrons}})_{MC}$			
$p_\perp$ in GeV	2–Jets	lifetime	anti-lifetime	high X
0.0-0.7	0.987 ± 0.016	0.97 ± 0.04	0.99 ± 0.03	1.02 ± 0.09
0.7-1.4	0.975 ± 0.016	1.02 ± 0.03	0.96 ± 0.03	0.91 ± 0.09
1.4-2.1	1.000 ± 0.021	1.00 ± 0.04	1.05 ± 0.05	0.75 ± 0.10
≥ 2.1	1.040 ± 0.019	1.03 ± 0.04	0.94 ± 0.04	0.87 ± 0.11

Table 5.4: Ratio of data vs. MC showing the $p_\perp$ dependence of the number of muon candidates for the different subsamples.

The systematics are estimated for the same sources as in the electron channel. The geometrical acceptance has been studied by comparing the angular distribution of the muons in data and Monte Carlo. The angular distributions are shown in figure 5.6 and found to be well described by the Monte Carlo. An additional inefficiency of the muon chamber is then estimated to be $5 \pm 1.5\%$ for 1992 data and $3\pm1\%$ for 1991 data relative to the simulation of a perfectly working detector. Figure 5.6 shows the distributions after applying those additional inefficiencies. These estimates agree with independent studies performed with muon pairs [70].

As in the case of electrons, the proportion of semileptonic c-hadron decays is varied by 10%. As an uncertainty of the $p_\perp$ definition the difference between the branching ratio obtained in the high $p_\perp$ region above 2.1 GeV and between 1.4-2.1 GeV is taken. The stability against the $p_\perp$ criterion is quantified in table 5.6. The only significant deviation with respect to the central value is the range between 0.7 and 1.4 GeV. Since no deviation is observed in the lifetime subsample, but it is also observed in the two b-depleted sample as seen in table 5.4, it is concluded that this deviation is again due to a background misdescription. The selection efficiency is again estimated varying the criteria given in chapter 3.2.

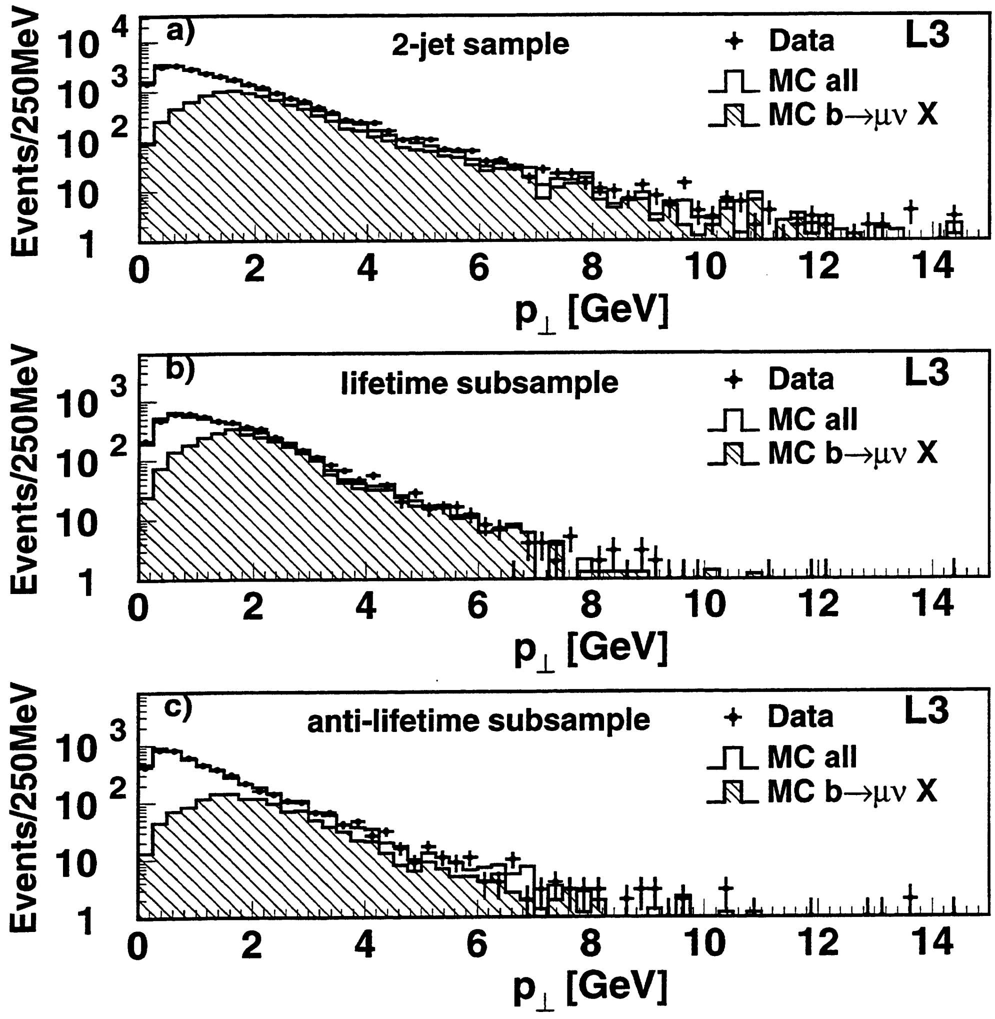

Figure 5.5: (a) The spectrum of $p_\perp$ with respect to the jet direction for the muon candidates in the two–jet sample, (b) in the b enriched lifetime sample and (c) in the b depleted anti-lifetime sample. The corresponding Monte Carlo distributions are also shown, together with the contribution of correctly identified semileptonic b–decays using a branching ratio of 10.45%. Good agreement can be observed for the signal and background enriched samples.

Error source	Δ Br(b$\rightarrow$ $\mu\nu$X) in %
selection efficency	0.20
$p_\perp$ dependency	0.31
semileptonic c-hadron decays	0.26
b-hadron momentum $< X_E >_b = 0.72 \pm 0.02$	0.25
two jet definition	0.28
total systematic	0.59

Table 5.5: Estimated systematic errors for the branching ratio measurement of the high $p_\perp$ muons.

Further sources of systematic errors are the fragmentation function and the two jet definition. The systematic errors are listed in table 5.5.
The momentum spectrum of the final sample in the range $1.4 \leq p_\perp < 2.1$GeV and $p_\perp \geq 2.1$GeV is shown in figure 5.7. While the lower $p_\perp$ range is well described by the Monte Carlo a small discrepancy for low momenta in the large $p_\perp$ range remains. As in the case of electrons, the final result given below would only decrease by 0.1% if the muon candidates with momenta above 6GeV would be used. The final result obtained for the branching ratio yields

$$\text{Br}(\text{b} \rightarrow \mu\nu\text{X}) = 10.82 \pm 0.15 \pm 0.59\% \tag{5.6}$$

where the first error is statistical and the second one systematic.

	Data	Monte Carlo		Data
$p_\perp$ [GeV]	$N_{\mu^\pm}/N_{had} \times 10^3$	$N_{\mu^\pm}/N_{had} \times 10^3$	purity b$\rightarrow$ $\mu^\pm\nu$X [%]	Br[%]
0.0–0.7	21.09±0.25	21.36±0.22	9.2	9.88±0.42
0.7–1.4	20.47±0.24	20.99±0.22	29.3	9.57±0.15
1.4–2.1	12.46±0.19	12.41±0.17	61.8	10.51±0.22
$\geq$ 2.1	15.90±0.21	15.29±0.19	71.2	11.03±0.20
>1.4	28.36±0.29	27.71±0.26	67.0	10.82±0.15

Table 5.6: The observed number of muon candidates per hadronic event in the data and in the Monte Carlo. The resulting semileptonic branching ratio Br(b$\rightarrow$ $\mu\nu$X) with the statistical errors are given for different $p_\perp$ values. A $p_\perp$ cut of 1.4 GeV is used to extract the final semileptonic branching ratio. For the Monte Carlo with an input semileptonic branching ratio of 10.45%, the purity of correctly identified semileptonic b–decays is also given.

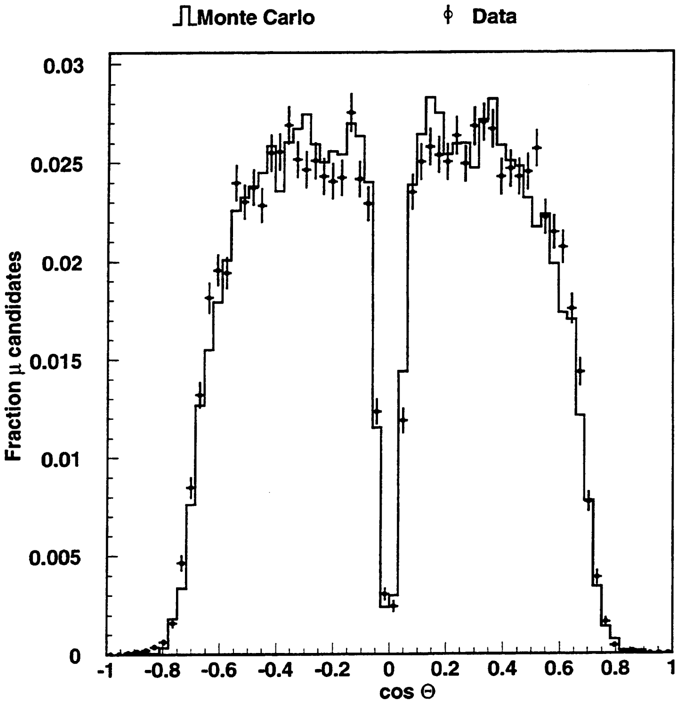

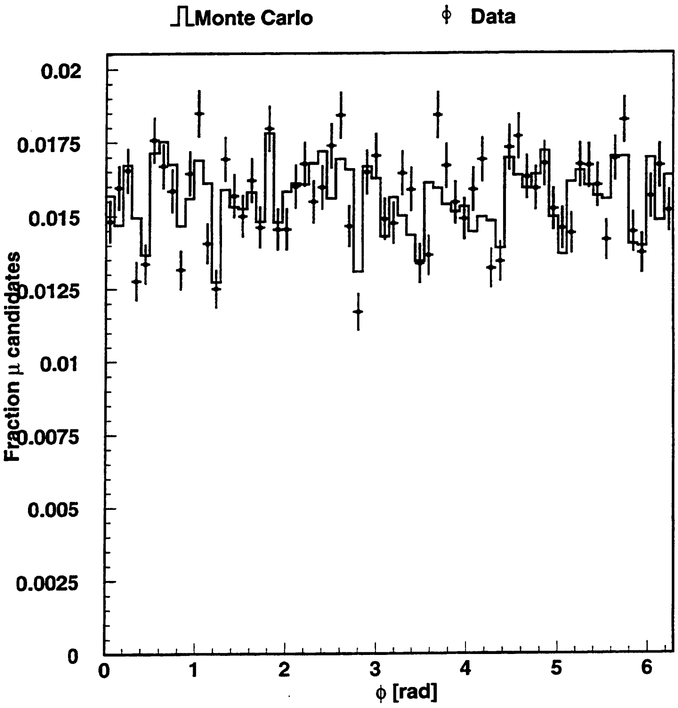

Figure 5.6: The description of the muon acceptance by the Monte Carlo is shown. The histogram is the Monte Carlo, the crosses are the data. The bottom plot shows the angular distribution in azimuth, the top plot the distribution in the polar angle.

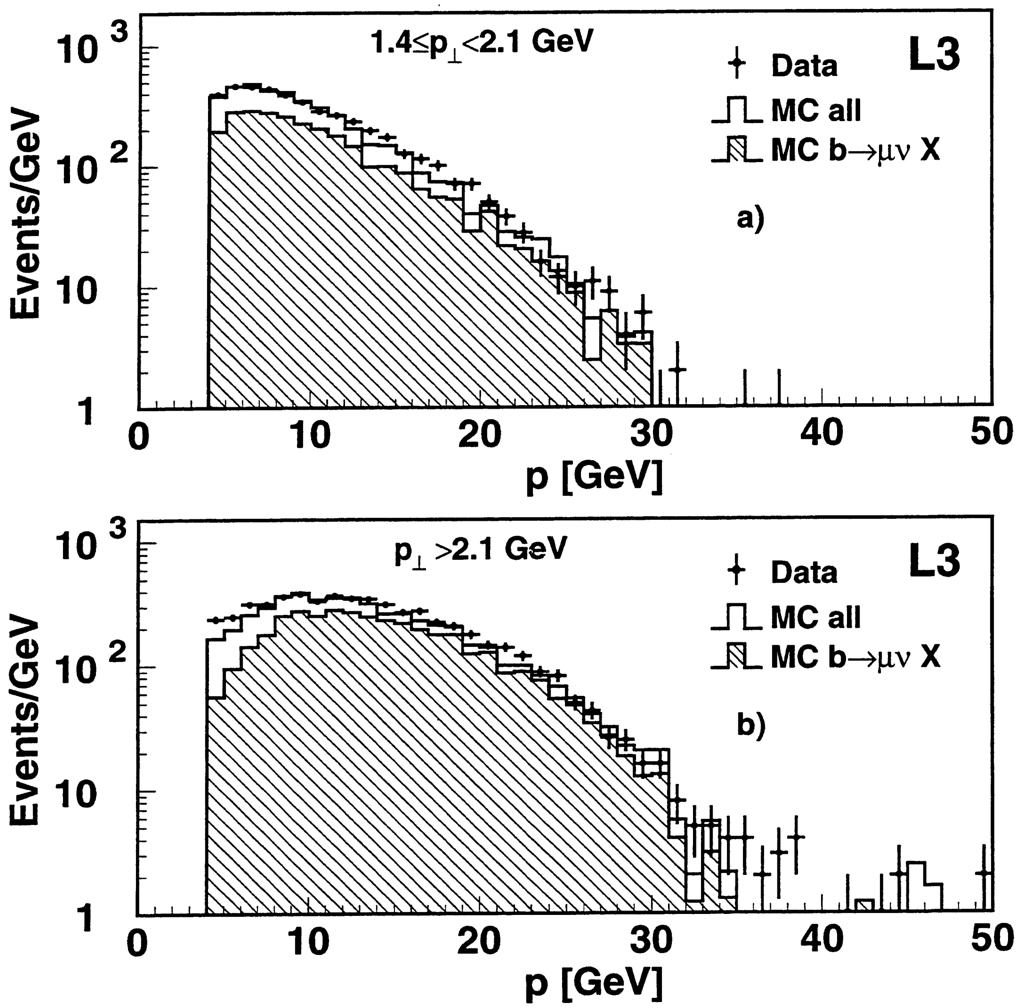

Figure 5.7: The momentum spectrum of the final muon sample in two $p_\perp$ ranges is shown. The Monte Carlo distributions are normalised to the total number of hadrons in the 2–jet sample.

5.2.3 Systematic uncertainties related to the two jet sample

The analysis of the branching ratios discussed in the previous section is performed using the two jet data sample. This is different from previous analysis [71]. The effect of the two jet selection is thus especially studied.

Since the jet mass is the main criterion to form jets and thus the two jet sample, the dependence on that mass is discussed. To classify the event as close as possible to the two jet criterion, the classification is done taking every hemisphere as a jet. Then the mass of the hemisphere is calculated. The hemisphere with the larger mass is called the "fat" jet. The classification is done by the mass of the "fat" jet, and the sample integrated up to a mass of 25 GeV corresponds to more than 95% the two jet sample. The small difference is for example due to three jet events, where a pair of jets would fulfil the mass criterion but not the angular criterion to build a single jet. This event would not be classified as two jet event.

By removing the two jet criterion and repeating the analysis a value of $11.0 \pm 0.2\%$ for electrons and $11.1 \pm 0.2\%$ for muon candidates is obtained. This is consistent within the errors with the measurement in the two jet data sample. However, if one takes into account the small increase of the event sample by removing the two jet criterion, which is essentially the events with a mass of more than 25 GeV, shown in the "fat" jet mass distribution of figure 5.8, the high mass range must have apparently a much higher branching ratio. Since the branching ratio should be independent of the jet mass, the efficiencies are wrongly described by the Monte Carlo or the number of b-jets is different as predicted by the Monte Carlo.

This could be due either to a wrong description of the detector in the Monte Carlo, the GEANT/GHEISHA part of the simulation [65], or to a physics problem. A physics problem could be also an implementation problem inside JETSET, but it should be sensitive to physics parameters.

The effect is studied with the different subsamples to check flavour dependencies. In table 5.7 the normalized fraction of hadrons for each mass range for different b-hadron contents is compared between data and Monte Carlo. The normalization is performed to the total number of tagged events and corrects therefore a global tagging efficiency difference between data and Monte Carlo. But the normalized fractions should be sensitive to flavour dependent differences.

As seen from the table 5.7, the Monte Carlo underestimates the number of "fat" jets with increasing b-purity and increasing mass compared with the data and overestimates for b-depletion and increasing mass.

This effect could be interpreted as misdescription of the $p_\perp$ of the b-hadron relative to the direction of flight of the primary b-quark. Since a different $p_\perp$ would be due to differences in the gluon radiation, the b-jet and the nearby gluon jet could build a combined jet with a higher mass, depending on the jet definition. The jet-axis of the combined jet would be displaced from b-hadron flight-axis. This leads to a jet-mass dependence of the Monte Carlo estimated tagging efficiency for all tags sensitive to the $p_\perp$ with respect to the nearest jet. If it would be a detector effect it could be due to a wrong description of the flavour dependence of the response, which here means especially a different response to different jet

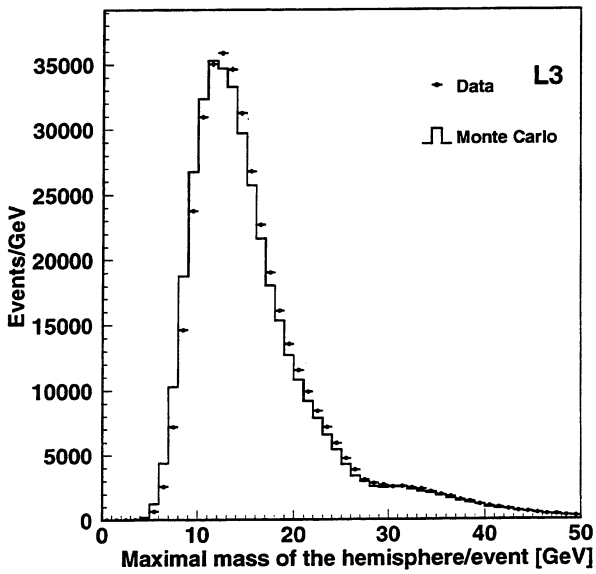

Figure 5.8: The mass of the "fat" jet.

energy densities. As this is not understood the effect is treated as a systematic error on the analysis.

One bound is coming from the removal of the two jet requirement, and the other is coming from a correction of the observed systematics. Using the lifetime sample as a b-sensitive sample and the anti-lifetime sample as a background sensitive sample a correction is estimated. The fraction of lifetime tagged events normalised to the number of hadrons is given by

$$n_{\mathcal{T}_b} = \epsilon_b^{\mathcal{T}_b} R_b + (1 - R_b)\epsilon_u^{\mathcal{T}_b} \ , \tag{5.7}$$

where ϵ_b is the b tagging efficiency and ϵ_u is the tagging efficiency for light quarks, R_b is the fraction of b-events of all hadronic Z-decays. Similarly, for the anti-lifetime sample the fraction of anti-lifetime tagged events is given by:

$$n_{\text{anti}-\mathcal{T}_b} = \epsilon_b^{\text{anti}-\mathcal{T}_b} R_b + (1 - R_b)\epsilon_u^{\text{anti}-\mathcal{T}_b} \tag{5.8}$$

Now R_b can be calculated using both equations:

$$R_b = \frac{\epsilon_u^{\text{anti}-\mathcal{T}_b} n_{\mathcal{T}_b} - \epsilon_u^{\mathcal{T}_b} n_{\text{anti}-\mathcal{T}_b}}{\epsilon_u^{\text{anti}-\mathcal{T}_b}\epsilon_b^{\mathcal{T}_b} - \epsilon_u^{\mathcal{T}_b}\epsilon_b^{\text{anti}-\mathcal{T}_b}} \tag{5.9}$$

With this ansatz R_b is calculated for each mass range and the fraction of Monte Carlo predicted tagged events is estimated using this R_b. This correction leads to a nearly flat distribution of the branching ratio with respect to the jet-mass. This can be seen in table 5.8, where the ratio of data to Monte Carlo with and without the corrected R_b is given. In contrast to table 5.7 the ratio here is not normalised to the global fraction of tagged jets. The branching ratio obtained

sample	high x	anti-lifetime	lifetime	μ	e
MC b-Purity	10%	11%	59%	78 %	86%
$m_{\text{Fat Jet}}[GeV]$	$\left(\frac{N^i_{tagged}N_{hadrons}}{N^i_{hadrons}N_{tagged}}\right)_{Data}$		/ $\left(\frac{N^i_{tagged}N_{hadrons}}{N^i_{hadrons}N_{tagged}}\right)_{MC}$		
0.0-10.0	1.08	1.05	0.93	0.86	0.81
10.0-15.0	1.03	1.02	1.01	0.96	0.96
15.0-20.0	0.98	0.99	1.04	0.98	1.05
20.0-25.0	0.94	0.97	1.03	1.11	1.07
$\geq$ 25.0	0.95	0.97	1.07	1.14	1.23

Table 5.7: The ratios of the fractions of tagged "fat" jets per mass range (i) of all hadrons normalised to the integrated fraction of tagged "fat" jets of data over Monte Carlo. These ratios should be independent of the overall tagging efficiency difference between data and Monte Carlo and reflect differences in the shape of the mass distribution in dependency of the b-purity.

	Electrons			Muons		
$m_{fat-jet}$ [GeV]	n_e	R_{raw}	$R_{corr.}$	n_μ	R_{raw}	$R_{corr.}$
$<$ 10.0	673	0.84±0.04	0.96±0.05	1248	0.91±0.03	1.02±0.04
10.0–15.0	2494	1.00±0.03	1.00±0.03	4609	1.00±0.02	1.00±0.02
15.0–20.0	1547	1.10±0.04	1.01±0.04	2903	1.07±0.03	1.00±0.03
20.0–25.0	771	1.16±0.06	1.08±0.06	1320	1.12±0.05	1.05±0.05
$>$ 25.0	657	1.28±0.08	1.07±0.07	1137	1.34±0.06	1.17±0.05

Table 5.8: Observed number of events N_ℓ in the data with high $p_\perp$ electron (n_e) or muon candidates (n_μ) for $p_\perp > 1.4$GeV and for the different mass bins of the "fat" jet in the data. The ratios between the fractions R= $N_\ell/N_{hadrons}$ in the data and the Monte Carlo are given for the raw Monte Carlo, R_{raw}, and the b–flavour purity corrected Monte Carlo, $R_{corr.}$. For all numbers only the statistical errors are given.

in the full sample is then $10.6 \pm 0.2\%$ for electrons and $10.8 \pm 0.15\%$ for muons. This leads to a lower bound for the systematic uncertainty.

The integrated sample, where the mass of the fat jet is less than 25 GeV and which corresponds to the 2–jet sample, needs only a negligible correction. It is therefore concluded that the uncorrected value in the two jet sample can be taken and the systematic error is 0.29% for the electron measurement and 0.28% for muons.

	Data [GeV]	$(< E_\nu >_{\text{Data}} - < E_\nu >_{\text{MC}})$ [MeV]	
neutrino type	$< E_\nu >$	(V–A)×(V–A) model	(V+A)×(V–A) model
b→X$e\nu_e$	6.44	–120 ± 120 ± 235	–1020 ± 120 ± 235
b→ X$\mu\nu_\mu$	6.08	180 ± 85 ± 217	–590 ± 85 ± 217

Table 5.9: The measured average neutrino energies $< E_\nu >$ in the data and the difference between the data and the Monte Carlo for the extreme assumptions. The first error is the statistical error for the average energy values estimated from the r.m.s. of the distributions; the second error is the combined systematic error.

5.3 Testing the space-time structure in weak b-decays

Once the charged lepton spectrum is correctly described by a given model, the neutrino energy spectrum is also predicted, as discussed in chapter 1. After tagging semileptonic b-decays as described, the missing energy spectrum of these hemispheres are obtained and compared with the different model predictions. With the described fragmentation function, the average momentum is found to be $12.15 \pm 0.09 \pm 0.10$ GeV for electrons and $11.99 \pm 0.06 \pm 0.10$ GeV for muons[2], where the first error is statistical and the second one systematic. The systematic uncertainty in the average charged lepton momentum mainly comes from the fragmentation function, and the semileptonic branching ratio, hence the purity of the sample. The uncertainty from the fragmentation function is assumed to be 100 MeV, as it is roughly half the discrepancy between data and Monte Carlo with the chosen parameter for the fragmentation function. This parameter as stated in the previous section is chosen such that the momentum spectrum of the candidates is best described by the Monte Carlo. This was achieved for $\bar{x}_{E_b} = 0.72 \pm 0.02$ for the weakly decaying b-hadron in the $\mathrm{V} - \mathrm{A} \times \mathrm{V} - \mathrm{A}$ case and $\bar{x}_{E_b} = 0.77 \pm 0.02$ in the $\mathrm{V} + \mathrm{A} \times \mathrm{V} - \mathrm{A}$ case. The semileptonic branching ratio is varied by 5% relative, which is roughly the uncertainty in the measurement described previously.

For the measurement of the neutrino momentum it is required that there is only one lepton candidate in the jet. Then the average electron neutrino energy is measured to be $6.44 \pm 0.12 \pm 0.24$ GeV and the muon neutrino $6.08 \pm 0.12 \pm 0.22$ GeV. The comparison with the models is shown in table 5.9. The difference in the average momentum between the data minus the Monte Carlo is –120 MeV for the electron neutrino in the V–A×V–A case and –1020 MeV in the V+A×V–A case. For the muon neutrino, the difference is 180 MeV for V–A×V–A and -590 MeV for V+A×V–A. The spectrum of the kaon-like V×V–A has a 400 MeV larger average neutrino energy than V–A×V–A case, so this case is disfavoured by the combined measurement with about 2 standard deviations.

The systematics in this measurement comes from the jet energy scale described in chapter 4.2, the purity of the sample which can be expressed by the uncertainty

[2]The numbers differ a little bit from the ones quoted in [72], since the number given here are without the requirement, that there is only one lepton in the jet.

Error Source	$\Delta E(e^{\pm})$ [MeV]	$\Delta E(\nu_e)$ [MeV]	$\Delta E(\mu^{\pm})$ [MeV]	$\Delta E(\nu_\mu)$ [MeV]
Jet Energy Calibration	–	150	–	150
Purity of b→ $X\ell\nu$ ±5%	10	150	20	120
$\ell^{\pm}$ Energy Uncertainty	100	100	100	100
Combined Error	101	235	102	217

Table 5.10: The dominant contributions to the systematic error for the average charged lepton and neutrino energy measurement.

in the semileptonic branching ratio b $\rightarrow \ell^{\pm}\nu$X, and the uncertainty in the average lepton momentum. The two uncertainties in the neutrino energy spectrum caused by the uncertainty in the charged lepton spectrum are evaluated analog the case of the charged lepton. The systematic errors are listed in table 5.10.

To compare the full spectrum the different resolution between data and Monte Carlo has to be taken into account. Due to the good agreement between the reconstructed neutrino spectrum and the Gaussian smeared spectrum, a Monte Carlo spectrum was obtained by smearing the generator spectrum with a gaussian resolution function of 4.2 GeV width. That this is feasible is discussed in chapter 4.2 and visible in figure 4.15.

Figure 5.9 shows the spectra of the neutrinos compared with the V–A×V–A and V+A×V–A model. The data of the electron neutrinos are well described by V–A×V–A model while the V+A×V–A Monte Carlo spectrum is harder. In the case of the muon neutrinos the data spectrum is slightly harder than the V–A×V–A case but softer than the V+A×V–A spectrum. This is quantified in table 5.11.

Comparing the range with hard neutrinos ($\geq$ 16 GeV, see table 5.11) the disagreement between V+A×V–A and the data is 5.7 standard deviations for the electron neutrinos and 3.7 standard deviations for the muons including systematic uncertainties. The V×V–A case is excluded by the electron neutrinos by 3.5 standard deviations while the muons neutrinos are consistent with both V–A×V–A and V×V–A.

5.4 The branching ratio b→ ν X and b→ $\tau\nu$ X

These branching ratios are measured in lifetime-tagged b events. After subtracting the background, the branching ratio is obtained by fitting the visible energy spectrum in the range between 15 and 60 GeV with a binned likelihood fit. In contrast to the study above, where the presence of the neutrino was assured by the presence of a charged lepton, high hadronic background has to be subtracted. This background contains hadronic b-decays, decays of other flavours and detector defects. The total sample of the two jet events is used to obtain an estimate for this background directly from the data. This sample has high statistics and

		$N_{Data} - N_{MC}$		
ν–energy [GeV]	N_{Data}	(V–A)×(V–A)	(V+A)×(V–A)	V×(V–A)
b→ $Xe\nu_e$ candidates				
< 0.0	960	-27 ± 39 ± 47	83 ± 39 ± 42	42 ± 39 ± 44
0.0–6.0	1782	11 ± 53 ± 101	97 ± 53 ± 96	39 ± 53 ± 99
6.0–16.0	2106	58 ± 58 ± 107	60 ± 58 ± 107	60 ± 58 ± 107
> 16.0	518	-42 ± 29 ± 21	-241 ± 31 ± 28	-140 ± 30 ± 24
b→ $X\mu\nu_\mu$ candidates				
< 0.0	1897	-76 ± 55 ± 119	37 ± 55 ± 112	-16 ± 55 ± 116
0.0–6.0	3245	-132 ± 71 ± 78	65 ± 71 ± 73	-54 ± 71 ± 76
6.0–16.0	3694	119 ± 75 ± 79	152 ± 75 ± 78	132 ± 75 ± 78
> 16.0	904	85 ± 37 ± 46	-258 ± 39 ± 65	-67 ± 38 ± 54

Table 5.11: The observed number of events for different neutrino energy regions in the data and the difference between the data and the different models. The errors given for the difference include the estimated statistical and systematic errors due to background, energy scale and the assumed accuracy of the neutrino measurement.

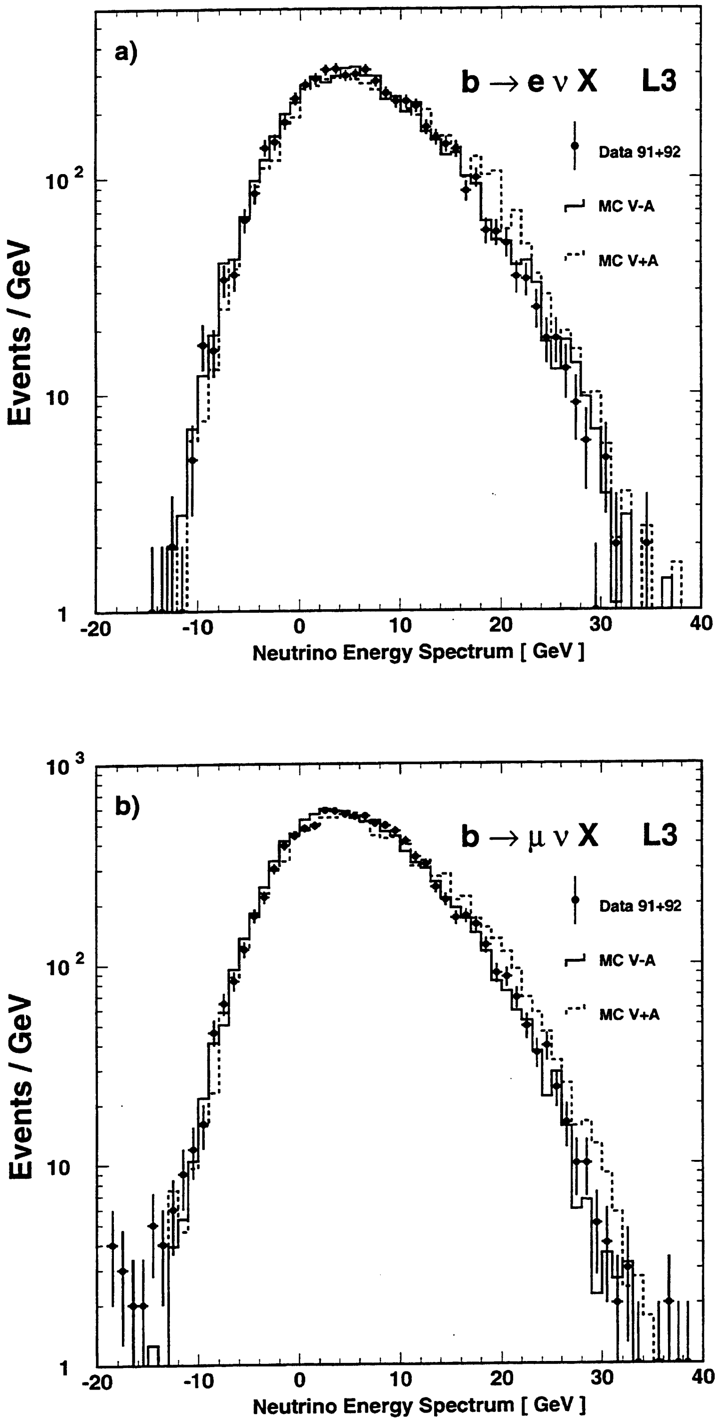

Figure 5.9: a) The electron neutrino spectrum compared with V–A×V–A and the V+A×V–A prediction. b) The same for the muon neutrino.

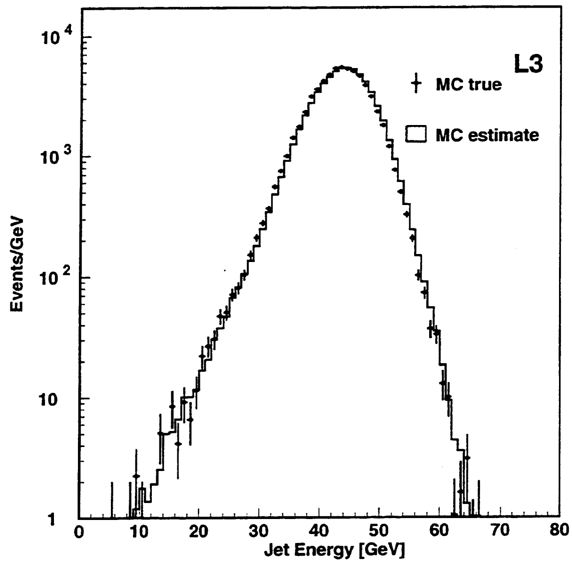

Figure 5.10: The hadronic background estimated from the two jet sample (histogram) compared with the hadronic background in the lifetime sample (dots). Compared is Monte Carlo with Monte Carlo.

no bias besides the mass cut. The main effect of the two jet criterion is the change of the b-purity from 21.6% to 22.85%.

The hadronic background is described with the two jet sample subtracting the remaining semileptonic b-decays during the fit procedure using Monte Carlo spectra and the actual branching ratio in the fitting procedure. Since b events have a higher contamination with neutrinos, the mean visible energy of the lifetime tagged events is lower than the one in the two jet sample. As it is the purpose of the two jet sample to describe the hadronic background, the scale has to be corrected with following shift :

$$\Delta E = E_{2-Jet} - E_{lifetime} + \Delta E_{2-Jet}^{hadronic} - \Delta E_{lifetime}^{hadronic} \tag{5.10}$$

where E_{2-Jet} means the mean energy in the two jet sample and $E_{lifetime}$ the mean energy in the lifetime sample taken from the data. $\Delta E_{2-Jet}^{hadronic}$ is the difference in the mean energy between the hadronic background and the full sample and $\Delta E_{lifetime}^{hadronic}$ is the same for the lifetime sample. $\Delta E_{2-Jet}^{hadronic}$ and $\Delta E_{lifetime}^{hadronic}$ are taken from the Monte Carlo. For the Monte Carlo this would lead simply to the difference between the mean energy of the background in the two jet sample and in the lifetime sample.

How well the corrected hadronic background in the two jet sample describes the hadronic background in the lifetime sample can be judged from figure 5.10, where the two spectra are compared. The background estimate from the two jet sample is normalised to the background events in the lifetime sample and good agreement between the two spectra is found.

The energies in the Monte Carlo lifetime tagged sample are corrected for the 150 MeV calibration bias. The shape of the neutrino spectrum in the b-enriched and in the background sample is then obtained by adding the semileptonic b-decay energy spectrum of the Monte Carlo with the ratio 1:1:0.25 for b-decays into electron, muon and tau respectively. Due to the theoretical uncertainty of the ratio of b $\to \tau\nu$X to b $\to$ eνX, a variation of $\pm$ 0.05 for the tau neutrino fraction is taken as systematic uncertainty.

Since the lifetime tag biases the leptonic branching ratio, mainly due to the different track multiplicity, this has also to be taken into account. Let now all energies in the two jet sample be shifted by ΔE, so $E' = E - \Delta E$, the hadronic background shape is then

$$\begin{aligned} N_{\tau_b}^{back}(E) = & N_{\tau_b} \\ & \cdot \left[P_{\tau_b}(1 - \alpha \cdot Br_\nu) + 1 - P_{\tau_b}\right] \\ & \cdot \frac{N_{\text{two jet}}(E') - N_{\text{two jet}} \cdot R_{\text{b}}^{\text{two jet}} \cdot Br_\nu \cdot n_{\text{two jet}}^{\nu X}(E')}{N_{\text{two jet}}\left[1 - R_{\text{b}}^{\text{two jet}} \cdot Br_\nu\right]} \end{aligned} \tag{5.11}$$

where τ_b denotes the lifetime tagged sample and E is the visible energy, N means the number of events, n the normalised fraction of events, P_{τ_b} is the purity in the lifetime sample, α is the bias of the branching ratio by the lifetime tag and Br_ν is the branching ratio b $\to \nu$X. The first term in brackets represents the predicted integrated fraction of background events, where the first summand is the fraction b $\to$ W* $\to$ hadronsX. The rest represents the fraction of non-b jets, and the fractional term represents the shape of the background spectrum. The predicted shape for the full sample is then

$$N_{\tau_b}^{pred}(E) = N_{\tau_b} \cdot P_{\tau_b} \cdot \alpha \cdot Br_\nu \cdot n_{\tau_b}^{\nu X}(E) + N_{\tau_b}^{back}(E) \tag{5.12}$$

Since the purity is given by the Monte Carlo, corrected by the number of leptons found in the data (lifetime) sample, and the shape for the visible energy spectrum of the neutrinos is also taken form the Monte Carlo, only one parameter is free, the branching ratio $B_\nu = Br(\text{b} \to \nu\text{X})$. This leads to the following likelihood

$$L = \prod_E P(N_{\tau_b}^{Data}(E)) \tag{5.13}$$

A binned fit is performed assuming a Poisson distribution for each bin:

$$P(N_{\tau_b}^{Data}(j)) = \frac{N_{\tau_b}^{pred}(j)^{N_{\tau_b}^{Data}(j)}}{N_{\tau_b}^{Data}(j)!} e^{-N_{\tau_b}^{pred}(j)} \tag{5.14}$$

giving the following log likelihood function [73]

$$l = \sum_{j=1}^{N} N_{\tau_b}^{Data}(j) \ln N_{\tau_b}^{pred}(j) - \ln(N_{\tau_b}^{Data}(j)!) - N_{\tau_b}^{pred}(j) \tag{5.15}$$

where j is going over energy bins and $N_{\tau_b}^{Data}(j)$ is the observed number of data events in that bin.

With this method a branching ratio of

$$\text{Be}(\text{b} \to \nu\text{X}) = 23.08 \pm 0.77 \pm 1.24\% \tag{5.16}$$

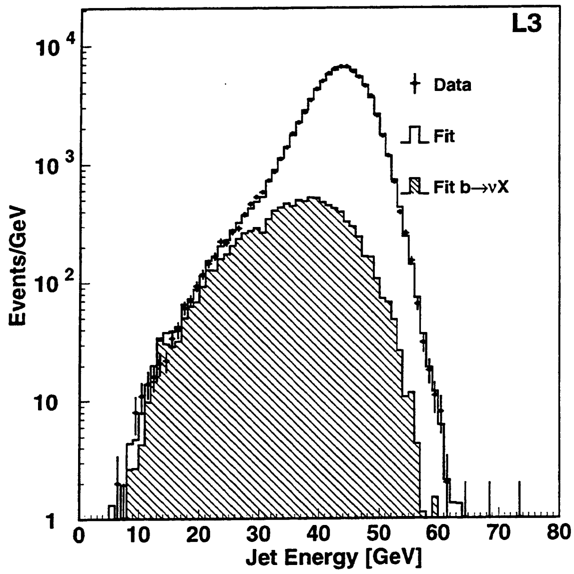

Figure 5.11: The final fitted distribution compared with the data. The neutrino content corresponds to the fitted branching ratio.

is obtained. The best fit to the visible energy distribution in lifetime tagged events and the contribution of semileptonic b-decays is shown in figure 5.11 and it can be seen that the fit describes the data well. The main systematic error sources are the purity of the lifetime tag, the energy uncertainties which were obtained from the V–A×V–A analysis, and the determination of the background. They are summarised in table 5.12

Error source	Systematic error [%]
background determination	± 0.61
purity of lifetime tag	± 0.90
assumed neutrino spectrum[a]	± 0.56
uncertainty in $b \to \tau\nu X$	± 0.20
Combined Error	± 1.24

Table 5.12: The systematic errors of the semileptonic branching ratio $b \to \nu X$.

[a]This energy uncertainty includes the uncertainties due to the b fragmentation function

The analysis chain is repeated constraining the background coming from semileptonic b decays into electron and muons. The central value of the combined branching ratio is $Br_\ell = \mathrm{Br}(\mathrm{b} \to \ell^\pm \nu \mathrm{X}) = 10.85\%$. So the determination of the hadronic background is now

$$N_{\tau_b}^{back}(E) = N_{\tau_b} \cdot [P_{\tau_b}(1 - 2 \cdot \alpha_\ell \cdot Br_\ell - \alpha_\tau Br_\tau) + 1 - P_{\tau_b}] \cdot \frac{N_{\text{two jet}}(E') - N_{\text{two jet}} \cdot R_{\mathrm{b}}^{\text{two jet}} \cdot (2 \cdot Br_\ell \cdot n_{\text{two jet}}^{\ell\nu X}(E') - Br_\tau \cdot n_{\text{two jet}}^{\tau\nu X}(E'))}{N_{\text{two jet}}\left[1 - R_{\mathrm{b}}^{\text{two jet}} \cdot (2 \cdot Br_\ell + Br_\tau)\right]} \tag{5.17}$$

where $Br_\tau = Br(\mathrm{b} \to \tau\nu\mathrm{X})$ and α_ℓ and α_τ are the bias of branching ratio into leptons or tau by the lifetime tag, respectively. Again Br_τ is the only free parameter and the full shape is given as

$$N_{\tau_b}^{pred}(E) = N_{\tau_b} \cdot P_{\tau_b} \cdot (2 \cdot \alpha_\ell \cdot Br_\ell \cdot n_{\tau_b}^{\ell}(E) + \alpha_\tau \cdot Br_\tau \cdot n_{\tau_b}^{\tau\nu X}(E)) + N_{\tau_b}^{back}(E) \tag{5.18}$$

The obtained branching ratio is

$$\mathrm{Br}(\mathrm{b} \to \tau\nu\mathrm{X}) = 1.7 \pm 0.5 \pm 1.1\% \ . \tag{5.19}$$

The resulting spectrum is shown in figure 5.12. Again the fit describes well the energy distribution of the data. The systematics in this measurement are similar to those in the b $\to \nu$X measurement. Since the background is partly constraint, some errors are smaller, but in addition there is a large systematic error due to the semileptonic branching ratio b $\to$ e(μ)νX. The errors are summarised in table 5.13.

Error source	Systematic error [%]
background determination	±0.33
purity of lifetime tag	±0.53
assumed neutrino spectrum[a]	±0.43
uncertainty in $Br(\mathrm{b} \to \mathrm{e}(\mu)\nu\mathrm{X})$	±0.79
Combined Error	±1.1

Table 5.13: The systematic errors of the semileptonic branching ratio b $\to \tau\nu$X.

[a] Again this energy uncertainty includes the uncertainties due to the b fragmentation function

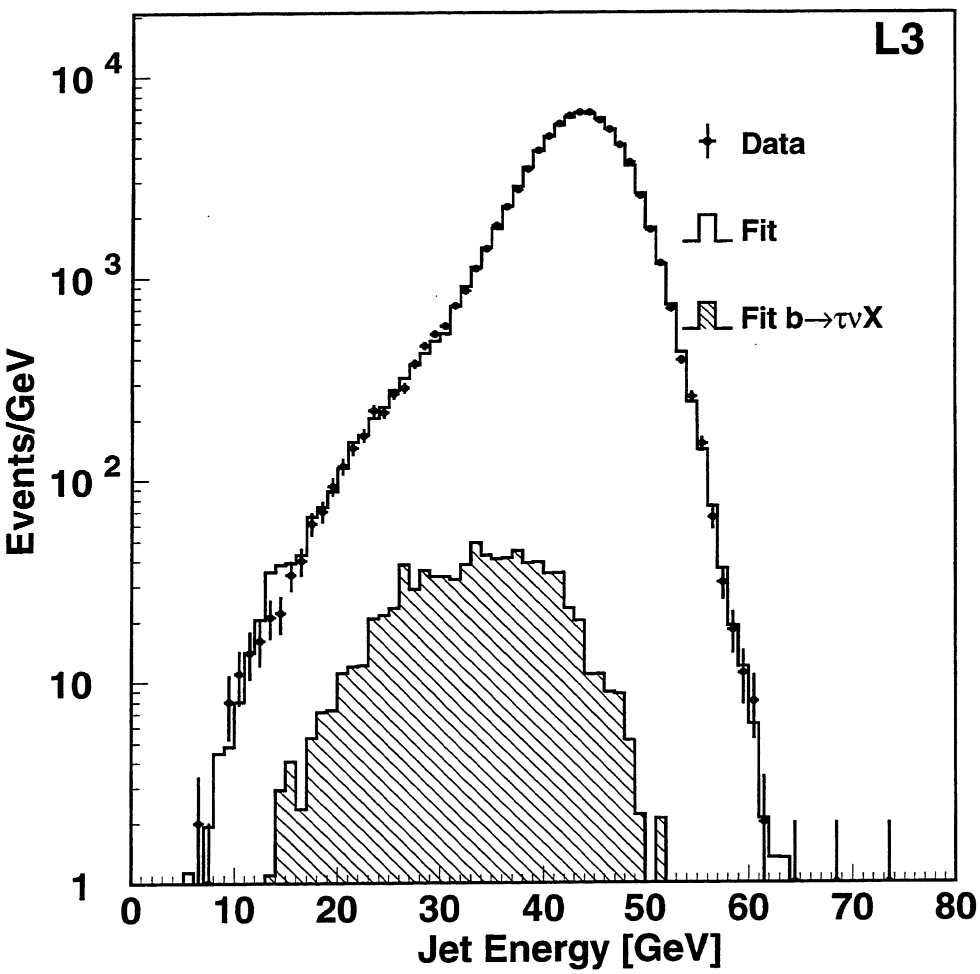

Figure 5.12: The final fitted distribution compared with the data and the τ neutrino content corresponding to the fitted branching ratio.

Chapter 6

Summary and Conclusions

The consequences of the preceding measurements in the framework of the Standard Model and beyond will be discussed. The first subject is the decay structure. Then the implication of the measurements for the CKM matrix will be discussed. In the next section of this chapter the result $Br(b \to \tau\nu X)$ is compared with theoretical predictions. At the end of the chapter final conclusions on the obtained results are given.

6.1 The space time structure of the weak charged current

The polarisation of the weak charged current has been tested, and a V–A×V–A structure of the charged current is found to be in good agreement with the data. The extreme assumption of a V+A×V–A structure is excluded by more than 6 standard deviations from the spectrum of hard neutrinos (more than 16 GeV) taking electron neutrinos and muon neutrinos together. The unpolarised case of V×V–A is disfavoured by more than 3 standard deviations.

An independent but less direct check of the V–A assumption is the branching ratio $b \to \nu X$. The Monte Carlo used to determine the efficiencies assumes a V–A structure, predicting a soft neutrino spectrum compared with the V+A assumption. If the data would have a V+A structure, this would lead to a much higher branching ratio of more than 27±1%[1] with our data. Under the assumption that a charged lepton is produced for each neutrino, hence demanding consistency between direct and indirect measurement of the branching ratio $b \to e(\mu)\nu X$, also the branching ratio measurement is inconsistent with a V+A b decay structure.

A further question is, whether this kind of measurements can distinguish the free quark model from exclusive decay models like the ISGW model [30]. Those models predict a V×V–A structure for the states $B_{u,d,s} \to D_{u,d,s}\ell\nu$. Most of the other states still have a V–A×V–A structure. The combination of different decay modes gives roughly the same charged lepton spectrum, while the neutrino spectrum is at most 50 MeV harder. This is smaller than the obtained experimental accuracy. This is also true for the assumption, that the b-quark polarisation is transfered

[1] 27% is the apparent branching ratio, where the observed excess is put into signal and background according to the purity.

to a b-baryon state. Even if this transfer is 100%, the net effect would result in a decrease of the average neutrino energy by only 80MeV.

In summary the V–A×V–A structure of the b-decay as it is implemented in JETSET is confirmed within the accuracy of this experiment. The dependence of the missing energy spectrum on exclusive decay models is below experimental precision. Nevertheless, for the first time, the neutrino spectrum is measured in identified semileptonic b-decays with a precision of ±200MeV for the average neutrino energy.

6.2 The semileptonic branching ratios and consequences for the CKM matrix

The semileptonic branching ratios Br(b $\rightarrow$ eνX) and Br(b $\rightarrow$ $\mu\nu$X) have been measured in a counting experiment, where the efficiencies are obtained using a JETSET simulation with the ACCMM model and a V–A structure for b hadron decays. The results are:

$$\mathrm{Br}(\mathrm{b} \rightarrow \mathrm{e}\nu\mathrm{X}) = 10.89 \pm 0.20 \pm 0.51\%$$
$$\mathrm{Br}(\mathrm{b} \rightarrow \mu\nu\mathrm{X}) = 10.82 \pm 0.15 \pm 0.59\%$$

which can be combined to

$$\mathrm{Br}(\mathrm{b} \rightarrow \mathrm{e}\nu\mathrm{X}) = \mathrm{Br}(\mathrm{b} \rightarrow \mu\nu\mathrm{X}) = 10.85 \pm 0.12 \pm 0.47\%$$

The result of Br(b $\rightarrow$ νX) $= 23.08 \pm 0.77 \pm 1.24\%$ taking into account the ratio 1:1:0.25 for branching into e,μ,τ respectively, gives

$$\mathrm{Br}(\mathrm{b} \rightarrow \mathrm{e}\nu\mathrm{X}) = \mathrm{Br}(\mathrm{b} \rightarrow \mu\nu\mathrm{X}) = 10.26 \pm 0.34 \pm 0.55\%$$

Combining the results of inclusive and exclusive measurements one obtains as the final result:

$$\mathbf{Br}(\mathbf{b} \rightarrow \mathbf{e}\nu\mathbf{X}) = \mathbf{Br}(\mathbf{b} \rightarrow \mu\nu\mathbf{X}) = 10.68 \pm 0.11 \pm 0.46\% \tag{6.1}$$

This is consistent with other measurements from LEP experiments [74] [75] [76] and model independent measurements from ARGUS [68] and CLEO [77] at the Υ(4S) production threshold. The results are summarised in table 6.1.

The next point to be discussed is which value for V_{cb} can be obtained. Equation 1.27

$$\Gamma(\mathrm{b} \rightarrow \ell\nu\mathrm{X}) = \frac{\mathrm{BR}(\mathrm{b} \rightarrow \ell\nu\mathrm{X})}{\tau_\mathrm{b}} = \frac{G_F^2 m_\mathrm{b}^5}{192\pi^3}(f_c|V_{cb}|^2 + f_u|V_{ub}|^2)$$

relates the partial width to the matrix elements V_{cb} and V_{ub} of the CKM-matrix. The width is given by the branching ratio and the average b-lifetime measured. The average lifetime value obtained by the particle data group PDG [22] is 1.537± 0.021 ps. This average from 1994 is consistent with recent measurements from

Experiment (Year)	Value [%]	R_b	$\bar{x}_{E_b}$
DELPHI (91-92)	$11.06 \pm 0.39 \pm 0.19 \pm 0.12\Gamma_{c\bar{c}}$	0.221	0.703
ALEPH (92-93) [a]	$11.01 \pm 0.10 \pm 0.21^{+0.24}_{-0.17}$	indep. [b]	0.707
This analysis (91-92)	$10.68 \pm 0.11 \pm 0.46$	0.216	0.72
OPAL (90-91)	$10.5 \pm 0.6 \pm 0.4 \pm 0.4$	0.224	0.696
Average	$10.94 \pm 0.18 \pm 0.25$(model) [c]	-	-
ARGUS	$9.7 \pm 0.5 \pm 0.4$	-	-
CLEO	$10.49 \pm 0.17 \pm 0.43$	-	-
LEP 94 [d]	$11.33 \pm 0.22 \pm 0.41$	-	-

Table 6.1: Summary of the different semileptonic branching ratio measurements. The first error is statistical, the second error is systematical and a third error indicates model dependency. All values at the Z are measured for different values of R_b and $\bar{x}_{E_b}$. If one would constrain them to a higher value of $R_b = 0.22$ and take the value recommended by LEP heavy flavour working group of $\bar{x}_{E_b} = 0.7$, the central of the measurements value would stay nearly (± 0.1) unchanged.

[a] This number is preliminary, the published value is in table 1.5.

[b] The measurement was done in a sample with more than 90 % b-purity.

[c] An assumption coming mainly from the Aleph model depedancy as it has the highest weight in the average.

[d] Compare table 1.5

LEP experiments, compare table 1.4, so it will be used here to extract $|V_{cb}|$. The partial width is then

$$\Gamma(\mathrm{b} \to \ell\nu\mathrm{X}) = 69.486 \pm 3.22\mathrm{ns}^{-1} = 45.74 \pm 2.12 \cdot 10^{-6}\mathrm{eV}$$

using the PDG average and the result in equation 6.1 of this analysis. From the width a circle can be defined in the $|V_{cb}|$, $|V_{ub}|$ plane, if the factors f_c and f_u are known. A factor f_q, where here q can be c or u, can be split into a phase space factor f^{PS} and a QCD correction f^{QCD}, so that

$$f_q = f^{PS}(x_q) \cdot f^{QCD}(x_q) \tag{6.2}$$

where

$$x_q = \left(\frac{m_q}{m_b}\right)^2 \tag{6.3}$$

The phase space factor can be written as

$$f^{PS}(x_q) = 1 - 8x_q + 8x_q^3 - x_q^4 - 12x_q^2 \ln x_q \tag{6.4}$$

if the lepton masses are neglected. The quark masses denoted here are the pole masses. The QCD corrections can be written as

$$f^{QCD} = 1 - \frac{2\alpha_s}{3\pi} \cdot g(x_q) + O(\alpha_s^2) \tag{6.5}$$

This ansatz can be found in Bigi et al. [78] and Nir [79], where $g(x_q)$ contains the mass ratio dependent part of the first order QCD correction. Nir calculates

Experiment	Model	Value
ARGUS [82]	ACCMM	0.11 ± 0.012
	WSB	0.13 ± 0.015
	KS	0.11 ± 0.012
	ISGW	0.20 ± 0.023
CLEO [83]	ACCMM	0.076 ± 0.008
	WSB	0.073 ± 0.007
	KS	0.056 ± 0.006
	ISGW	0.101 ± 0.010

Table 6.2: Values of $|V_{ub}/V_{cb}|$ obtained by ARGUS and CLEO.

the expression $h(x_q) = f^{PS}(x_q) \cdot g(x_q)$ to all orders of x_q. Since $x_q \leq 0.1$, it is sufficient to write

$$\begin{aligned} h(x_q) =& \pi^2 - \frac{25}{4} + x_q\,(68 + 24\ln x_q) - 32 x_q^{\frac{3}{2}} \pi^2 \\ &+ x_q^2 \left(16\pi^2 + 273 - 36\ln x_q + 36\ln^2 x_q\right) - 32 x_q^{\frac{5}{2}} \pi^2 + \mathrm{O}(x_q^4), \end{aligned} \tag{6.6}$$

and equation 1.27 can be rewritten as

$$\begin{aligned} \Gamma(\mathrm{b} \to \ell\nu \mathrm{X}) = & \frac{G_F^2 m_\mathrm{b}^5}{192\pi^3} \cdot \\ & \left[\left(f^{PS}(x_c) - \frac{2\alpha_s}{3\pi} h(x_c)\right)|V_{cb}|^2 + \left(f^{PS}(x_u) - \frac{2\alpha_s}{3\pi} h(x_u)\right)|V_{ub}|^2\right]. \end{aligned} \tag{6.7}$$

Since the masses of quarks are not well defined, because they are not observable, and even the pole mass depends on the renormalization ansatz used, some uncertainty is introduced with the choice of the mass. A detailed discussion is given by Ball et al. [80] using the result obtained in [79]. Here the pole masses are used given in a recent calculation from Ball et al. [81], they are $m_b = 5.05 \pm 0.06$ GeV and $m_c = 1.62 \pm 0.07$ GeV. The corresponding mass ratio is $\sqrt{x_c} = 0.321 \pm 0.014$. With this mass ratio the phasespace factor is $f^{PS}(x_c) = 0.47 \pm 0.03$ and $h(x_c) = 0.902 \pm 0.156$. The mass of the u quark is small, on the order of 5 ± 1.5 MeV [79], so the ratio can be taken as $\sqrt{x_u} \to 0$, thus $f^{PS}(0) = 1$ and $\lim_{x_u \to 0} h(x_u) = \pi^2 - \frac{25}{4}$. The quark masses are taken on their scale, which means for the running mass at the fix point $m_q(m_q)$. The remaining problem is the scale for α_s. It should be the one [79], where the second order correction are expected to be the smallest, so a value of $\alpha_s = 0.20 \pm 0.02$ [79] is used. The following factors are then obtained: $f_c = 0.432 \pm 0.031$ and $f_u = 0.846 \pm 0.015$.

The values of the measurements for $|\frac{V_{ub}}{V_{cb}}|$ from ARGUS [82] and CLEO [83] obtained from the endpoint spectrum of leptons are collected in table 6.2. The average value for the ACCMM model is 0.086 ± 0.007. Since this analysis is done in the ACCMM framework, this value is taken as experimental input to extract $|V_{cb}|$. The value obtained is

$$|V_{cb}| = 0.0373 \pm 0.0017 \tag{6.8}$$

and correspondingly

$$|V_{ub}| = 0.0032 \pm 0.00019 \tag{6.9}$$

which is shown in figure 6.1.

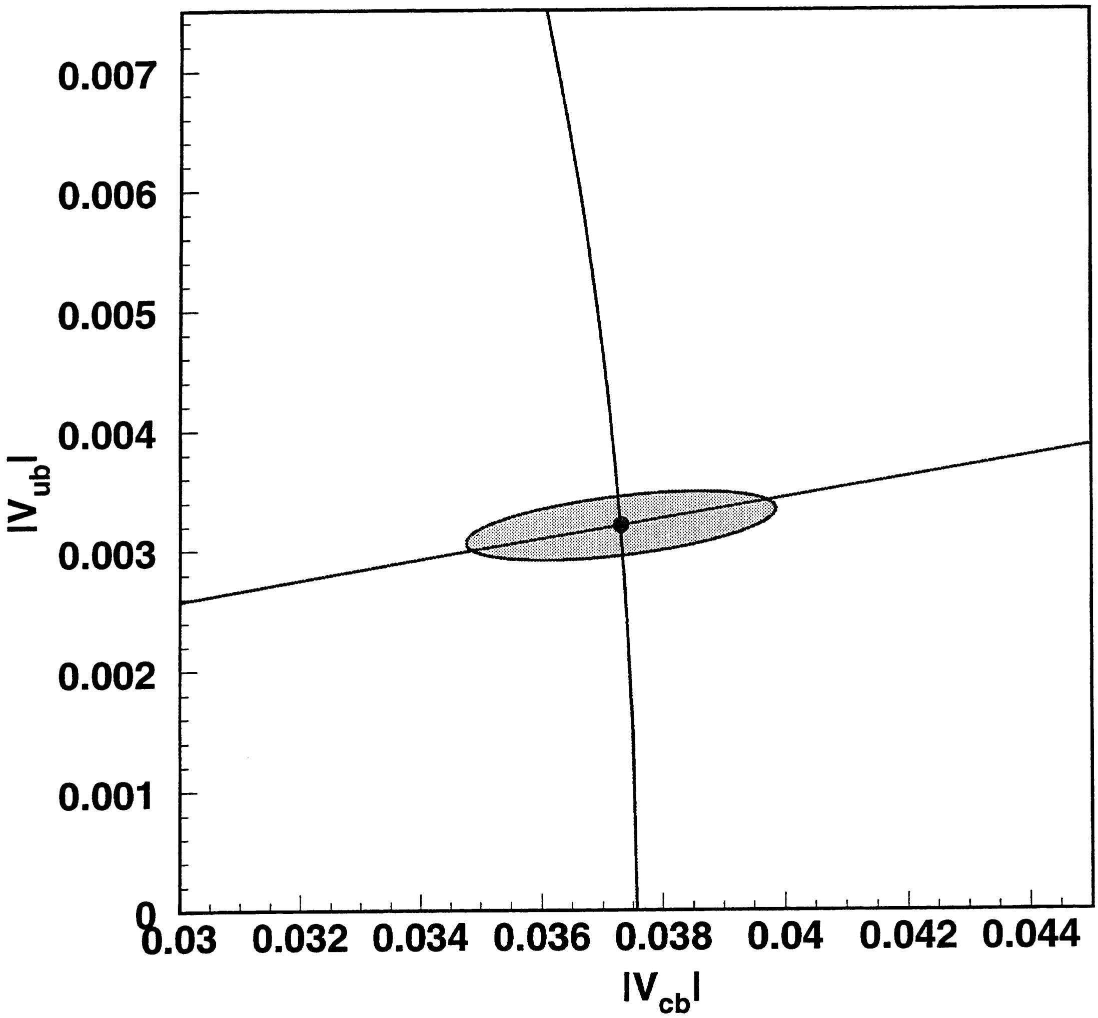

Figure 6.1: The result for the determination of $|V_{cb}|$ and $|V_{ub}|$. The part of the circle is obtained in this measurement and the straight line is from the ARGUS and CLEO measurement. The ellipse shows the 68% confidence range.

This result is lower than the result extracted by Neubert [84] in a review of recent experimental and theoretical efforts to obtain $|V_{cb}|$, but it is consistent within errors. The difference is mainly due to the b quark mass chosen and α_s.

Experimentally the value obtained here is consistent with the complementary measurements using the exclusive decay $B \to D^*\ell\nu$. Heavy quark effective theory

HQET gives an expression for the exclusive decay rate [85]:

$$\frac{d\Gamma}{d\omega} = \frac{G_F^2}{48\pi^3} m_{\mathrm{D}^{*+}}^3 (m_{\mathrm{B}^0} - m_{\mathrm{D}^{*+}})^2 \mathcal{F}^2(\omega) |V_{cb}|^2 \sqrt{\omega^2 - 1}$$
$$\times \left[4\omega(\omega+1) \frac{1 - 2\omega r + r^2}{(1-r)^2} + (\omega+1)^2 \right] \quad (6.10)$$

where $r = \frac{m_{\mathrm{D}^{*+}}}{m_{\mathrm{B}^0}}$ and ω is the scalar product of the four velocities of the $\overline{\mathrm{B}^0}$ and D^{*+} mesons. The function $\mathcal{F}(\omega)$ is not specified by HQET, but its value is normalized to one at $\omega = 1$ in the heavy quark limit ($\lim_{m_b \to \infty}$) and a value for finite quark masses is calculable at this point.
The experiments mentioned in table 6.3 measure $\frac{d\Gamma}{d\omega}$ and obtain $\mathcal{F}(1) \cdot |V_{cb}|$ through extrapolation, where $\mathcal{F}(1)$ contains now the QCD corrections. The value given by Neubert [84] for $\mathcal{F}(1) = 0.91 \pm 0.04$ is used to extract $|V_{cb}|$ in table 6.3. There the inclusive measurement is compared with the exclusive measurements. This analysis is found to be consistent within the errors and the error comparable with respect to the more model independent determination of $|V_{cb}|$.

Experiment	$\lvert V_{cb}\rvert$
CLEO [84]	0.0386 ± 0.0028
ARGUS [84]	0.0426 ± 0.0050
ALEPH [86]	0.0345 ± 0.0040
DELPHI [87]	0.0389 ± 0.0038
This measurement	0.0373 ± 0.0017

Table 6.3: Comparison with measurements using the exclusive decay $\mathrm{B} \to \mathrm{D}^* \ell \nu$ The error contains systematic, statistical and theoretical uncertainties. Note that following reference [84] a higher theoretical uncertainty of ± 0.005 should be assigned to the inclusive case.

6.3 Comparison of Br($\mathrm{b} \to \tau\nu\mathrm{X}$) with theory

The branching ratio $\mathrm{Br}(\mathrm{b} \to \tau\nu\mathrm{X})$ has not been calculated theoretically. Only the ratio

$$R = \frac{\mathrm{Br}(\mathrm{b} \to \tau\nu\mathrm{X})}{\mathrm{Br}(\mathrm{b} \to e\nu\mathrm{X})} \quad (6.11)$$

is calculated [88] [89]. This has the advantage to be less dependent on QCD corrections and mainly expresses the phase space suppression of the decay into τ. In the measurement presented here, the two branching ratios are measured consistently. Since they are correlated through the measurement method, the ratio has a reduced error. The result obtained is:

$$\mathrm{Br}(\mathrm{b} \to \tau\nu\mathrm{X}) = 1.7 \pm 0.5 \pm 1.1\%$$
$$\frac{\mathrm{Br}(\mathrm{b} \to \tau\nu\mathrm{X})}{\mathrm{Br}(\mathrm{b} \to e\nu\mathrm{X})} = 0.15 \pm 0.04 \pm 0.07$$

Experiment	Method	Br(b $\to \tau\nu$X) measured [%]	$\bar{x}_{E_b}$	Br(b $\to \tau\nu$X) for $\bar{x}_{E_b} = 0.72$
ALEPH [90]	lepton tag, lepton veto	$2.75 \pm 0.30 \pm 0.37$	0.714	2.64
L3 [91]	lepton tag, lepton veto	$2.4 \pm 0.7 \pm 0.8$	0.686	-[a]
OPAL[b] [92]	lifetime tag, shape fit	$2.58 \pm 0.11 \pm 0.51$	0.695	1.79
This measurement	lifetime tag, shape fit	$1.7 \pm 0.5 \pm 1.1$	0.72	1.7

Table 6.4: The comparison with the other measurements of Br(b $\to \tau\nu$X). To make the comparison easier also the value for our value of $\bar{x}_{E_b} = 0.72$ is given.

[a]Here no error on $\bar{x}_E$ was evaluated
[b]This is a preliminary result submitted to the ICHEP conference in summer 1996

Figure 6.2 shows that the measured value is consistent with the Standard Model prediction. A comparison with other measurements of b $\to \tau\nu$X is given in table 6.4. Note that all other measurements have not determined the branching ratio Br(b $\to$ e(μ)νX) in the same sample and used different parameters for R_b and $\bar{x}_{E_b}$. This makes a comparison difficult, nevertheless within errors the measurements are consistent. To ease the comparison the numbers are recalculated in table 6.4 to a common value $\bar{x}_{E_b} = 0.72$, since this gives the largest systematic effect.

Eventhough the results are consistent with Standard Model expectations, equation 1.39

$$\Gamma = \frac{|V_{cb}|^2 G_F^2 m_b^5}{192\pi^3}\left[\Gamma_W + \frac{1}{4} r^4 m_\tau^2 m_b^{Y2} \Gamma_H - 2\mathrm{Re}(r^2 m_\tau m_b^Y)\frac{m_\tau}{m_b}\Gamma_I\right]$$

allows to give a limit for the supersymmetry parameter $r = \frac{\tan\beta}{m_H^\pm}$. The contribution from b $\to$ u transitions is neglected, and we have the W mediated (W), the Higgs mediated (H) part and the interference term (I). The limit will be extracted for the free quark model, and the calculation will follow the prescription of Grossman and Ligeti [51]. Again only pole quark masses will be used with the numerical values given by [81] as in the previous section and $m_\tau = 1.7771 \pm 0.0005$GeV as given by the PDG [22]. In the free quark model $\Gamma_H = \Gamma_W$ and for the interference term one obtains $\Gamma_I = 0.07 \pm 0.25$, which is compatible with zero. So for the free quark model:

$$\Gamma = \frac{|V_{cb}|^2 G_F^2 m_b^5}{192\pi^3}\Gamma_W\left[1 + \frac{1}{4} r^4 m_\tau^2 m_b^2\right] \tag{6.12}$$

Again only the ratio of equation 6.11 should be used to avoid uncertainties in the QCD corrections. The following modified ratio R' is obtained

$$R' = R \cdot \left[1 + \frac{1}{4} r^4 m_\tau^2 m_b^2\right] \; . \tag{6.13}$$

The experimental 95% confidence level upper limit for the ratio, corresponding to 1.64σ, is 0.28. The measured ratio is smaller than the lowest value for the

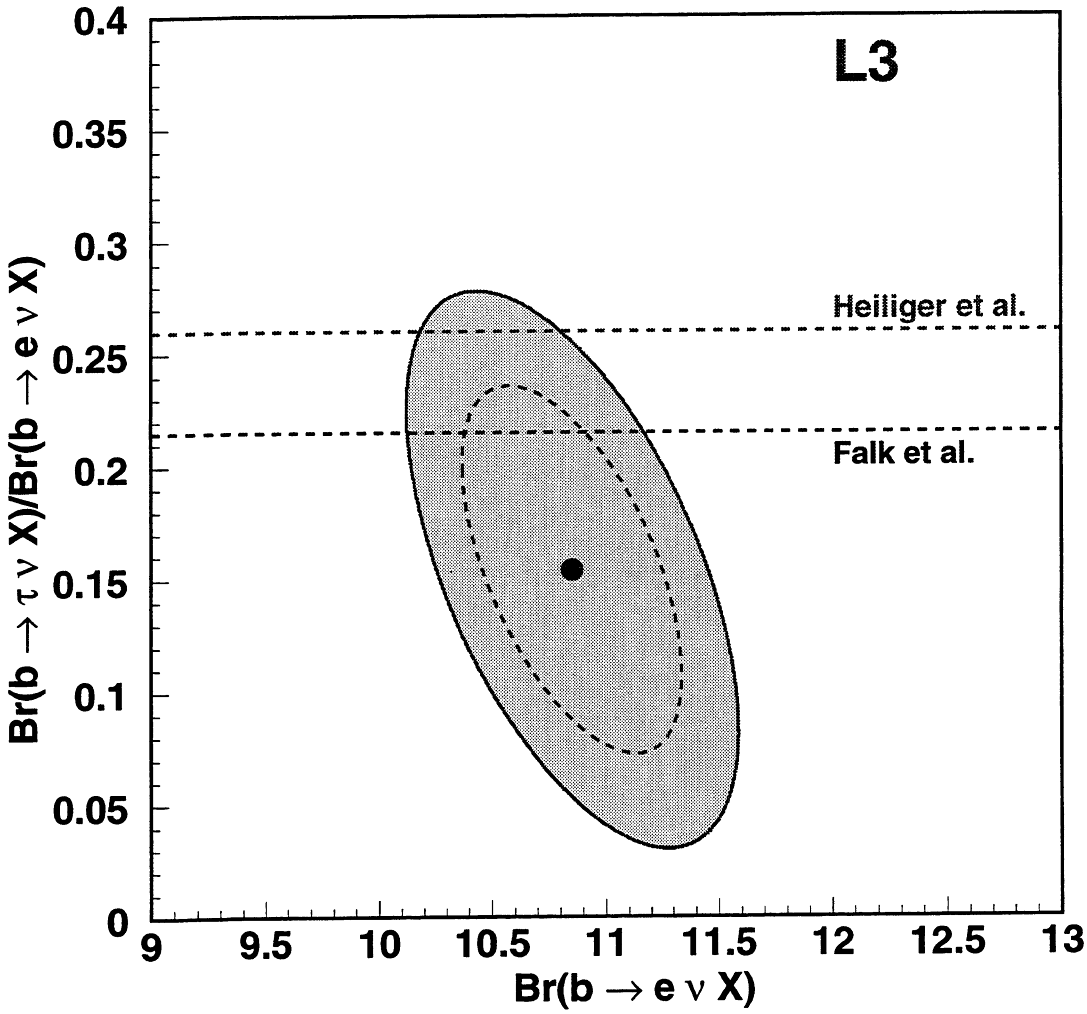

Figure 6.2: Comparison of the ratio of Br(b $\rightarrow \tau\nu$X) and Br(b $\rightarrow$ eνX) from this analysis with theory. The dashed ellipse shows the 39% confidence level and the solid ellipse the 68% confidence level.

theoretical Standard Model prediction of 0.22 [89]. To be conservative in setting the limit, this lower value is taken as the Standard Model value, and one obtains

$$\frac{R'}{R} < 1.27 , \tag{6.14}$$

so

$$r = \frac{\tan\beta}{m_{H^\pm}} < 0.24\text{GeV}^{-1} . \tag{6.15}$$

This limit of $r < 0.24\text{GeV}^{-1}$ at 95 % confidence level has to be compared with the limit obtained by ALEPH [90] of $r < 0.52\text{GeV}^{-1}$ at 90% confidence level in a similar analysis. The analysis of Br(b $\rightarrow$ sγ) is even more sensitive to a charged Higgs. In an analysis [93] of the CLEO measurement of Br(b $\rightarrow$ sγ) and the top discovery by CDF and D0, Chang and Lü obtain a limit of $m_{H^\pm} > 310$GeV at 95% confidence limit for $\tan\beta \rightarrow \infty$, which gives the lowest limit in this approach. This measurement then limits $\tan\beta < 74.4$ at 95% confidence level.

6.4 Final conclusions

The weak charged current is probed in semileptonic b-decays, where the focal point is the neutrinos in contrast to many other measurements. The physics goals are the study of

- the structure of the current in b-decays,
- the strength of the coupling and thereby the absolute value of the elements of the CKM matrix involved, and
- the question whether or not physics beyond the Standard Model is involved.

A first direct measurement of the space time structure of b-decays is made by comparing the charged lepton spectrum with the neutrino spectrum, and a V–A×V–A structure is found. This structure of the decay was up to now assumed by the different models and was now experimentally confirmed. The V+A×V–A structure could be excluded with more than 6 standard deviations. The missing energy measurement was made with a precision of ±200MeV or 3% relative for the average neutrino energy.

The question of the strength of the coupling was addressed with a measurement of the semileptonic branching ratio b $\rightarrow$ e(μ)νX. Furthermore the missing energy measurement is used to obtain the first result of the branching ratio Br(b $\rightarrow$ νX). This measurement is sensitive to the semileptonic branching ratio Br(b $\rightarrow$ e(μ)νX) as well as to Br(b $\rightarrow$ $\tau\nu$X). This measurement also gives an independent but indirect estimate of the decay structure. Again the V–A×V–A structure is confirmed and the absolute value of the elements V_{cb} and V_{ub} of the CKM matrix are extracted:

$$|V_{cb}| = 0.0373 \pm 0.0017$$
$$|V_{ub}| = 0.0032 \pm 0.00019$$

Branching ratio measurements suffer from rather large uncertainties due to the fragmentation parameter. To obtain more precise numbers, the fragmentation has to be measured to a much higher precision and the recently measured high value of R_b has to be understood. Besides these points the experimentally achievable limit is reached and the dominant uncertainty for $|V_{qb}|$ is on the theoretical side. The branching ratio Br(b $\rightarrow \tau\nu$X) is systematics limited. It suffers from the rather low purity of the lifetime tag and even more from the relatively high error on the purity. However, the tagging method used here could not profit from the L3 microvertex detector, since the upgrade of the L3 detector with a microvertex detector and the understanding of its systematics was unfortunally to late for this analysis. Nevertheless a stringent limit on $\frac{\tan\beta}{m_{H^\pm}} < 0.24\mathrm{GeV}^{-1}$ was set compared with similar analysis and the data are found to be fully consistent with Standard Model physics.

Appendix A

Calibration of the TEC

The tracks in the tracking device lay on a circle with good precision. The trajectory can be fixed with two points and the curvature of the track. The calibration constants are the parameters of the drifttime to driftdistance relationship. In most of the driftvolume this is a linear relation:

$$y_{local} = v_D t + y_0 \tag{A.1}$$

where y_{local} is the driftdistance in local coordinates of a sector, v_D is the driftvelocity. y_0 is the coordinate of the point where the field starts to have this linear behaviour; in the ideal case thus would be in the position of the grid. The time t is the measured drifttime with the time delay of the electronics t_0 subtracted. There are two complications. The simple one is the accelerating field for the gas amplification in the gap which leads to corrections up to the sixth power of the drifttime, but only for a short distance. The other one is the degradation of the linear behaviour towards the cathode region. The last effect starts roughly at two third of the driftregion and covers therefore a big volume. In this so called cathode region the drifttime to driftdistance relation is well approximated by a polynomial

$$y_{local} = a_1(t - t_{cathode})^3 + a_0(t - t_{cathode})^2 + v_D t + y_0 \tag{A.2}$$

where $t_{cathode}$ is taken as the time where the degradation starts. Since the transition between the cathode region and the linear region should be smooth, a constraint has to be made such that the first derivative of the relation has to be v_D and higher derivatives have to vanish at the point $t = t_{cathod}$. This is, as can be seen in equation A.2, achieved by construction.

The TEC is calibrated for the data taking period until 1993 with a $p_{t_{Beam}}$-constraint calibration. The reaction Z $\rightarrow$ $\mu\mu$ provides a pair of back to back tracks with a well known momentum. The $p_{t_{Beam}}$ of these muons provides the curvature, because the curvature is proportional to the transverse momentum of the track with respect to the beam. The momentum is measured with the muon chambers with a resolution of 2.5%, or, for the few which escape through holes in the muon system, can be constraint to the beam energy. A 45 GeV muon is minimum ionising in the electromagnetic calorimeter and releases around 2.5 GeV in the hadron calorimeter and can also be detected using the tracking device and the calorimeters.

The second constraint used in the calibration is the fill vertex which is obtained by using hadronic events. The additional point needed to fix the track is delivered by the TEC itself. Due to the geometry of the chamber, see figure 2.5, a half-sector of the inner sector covers a full sector of the outer. With a perfect calibration the extrapolation of the track containing the hits in the outer chamber should fit the ones in the inner too. This matching criterion between the chambers provides the remaining constraint. Also due to the geometry, a mismatch between the inner and outer segments characterises the kind of miscalibration. For this purpose segments are divided into regions. These regions are defined by the halfsectors of the inner and the outer where the tracks goes through.

The halfsector in positive ϕ direction is named +, the other –. The regions are then a combination of the halfsector of the outer chamber and a halfsector of the inner chamber. In detail, starting with low values in ϕ we have a halfsector in the inner (–) and a halfsector of the outer (–). The next region is the same halfsector of the inner and the other halfsector of the outer TEC (+). Then follows the same scheme with the next halfsector of the inner TEC (+). So the regions are $--$, $-+$, $+-$ and $++$ where the first sign indicates the inner halfsector and the second the outer halfsector.

The characterisation of the miscalibration can be shown in the following example. Assuming that the real driftvelocity in the segment is smaller than in the calibration, the track is shifted to larger distances. This means a negative shift of the mean residuals of the unfitted hits in the inner chamber in region $--$ and in region $++$ a positive shift.

The calibration is performed in two steps.h e global calibration of a segment fixes the tracks in space. The single wire calibration, which makes a correction to the calibration parameters according the individual behaviour of the wires. A set of calibration constants and the set of fillvertices with which the calibration is performed build then the final set of constants which can be used to measure the tracks. Due to this dependence and also due to the correlation of the global calibration with the single wire calibration, the whole calibration process, including the determination of the fillvertices, has to be iterated until the obtained corrections can be neglected.

The global calibration is done relative to a set of reasonable starting values. All tracks in the calibration set are fitted using all hits in the outer chamber except the last eight wires, were the boundary of the TEC influences the field, and the fill vertex. The average residuum of the hits in the inner chamber determines the mismatch between outer and inner. The following relation measures the quality of the matching:

$$\chi^2 = \sum_{i=++,+-,-+,--} \frac{\mathrm{Mean}_i^2}{\mathrm{RMS}_i^2} + \frac{\mathrm{RMS}_i^2}{<\mathrm{RMS}>^2} \tag{A.3}$$

where i runs over the different regions of the segment as described above. The mean is the mean residual, and the RMS is the root mean square residual of the hits in the unfitted inner chamber. $<$ RMS $>$ means the mean RMS of the whole segment. The second term in A.3 prevents to get a constant solution with mean zero. The surface of the χ^2 function can be sometimes "rough", but there is always strong correlation between the offset and the driftvelocity. Therefore it is often difficult to minimise, and a robust algorithm is used. The algorithm is a simple grid search using first widely spaced and later narrowly spaced lattices, where the center of the lattice is chosen to be at the minimal point of the previous iteration.

The single wire calibration is the step where the calibration track is treated as well determined and the hits are forced to lay on the track. The residuals as a function of the drifttime indicate directly the corrections. This can be seen in the case of an uncalibrated TEC where the input is the above mentioned reasonable set of calibration constants. A constant driftvelocity of $5.95\frac{mm}{\mu s}$ and no correction for non linear behaviour. In figure A.1 the mean residuals versus drifttime for the last wires of all sectors are shown. The slope in the beginning indicates the wrong driftvelocity. Also clearly seen is the nonlinear behaviour towards the cathode. This type of wire is the most extreme example found in the TEC. In figure A.2 examples of other types of wires are shown. Note that in the plots which show wires of the inner TEC the structure of the TEC is clearly indicated. To the left one sees the region where the cathode of the inner chamber is aligned with cathode of the outer. Then follows the resolution loss from the region where the anodes of the outer chambers are. In the middle, the cathode of the outer and the anode of the inner chamber is aligned.

In a first step the area reaching from the grid to $\frac{2}{3}$ of the maximum drifttime, where the wires behave nearly perfectly linearly, is calibrated using relation A.1. This is done by performing a linear least square fit to the residuals versus drifttime relation. This determines Δv_D and Δy_0, which is then used to correct the start values. The next step is the determination of the nonlinear correction in the area where the linear relation degrades. Leaving the linear part untouched, the linear term is taken from the region $t < t_{cathod}$. The problem can thus be linearised with

$$\begin{aligned} y' &= \frac{y - v_D t - y_0}{(t - t_{cathod})^2} && \text{(A.4)} \\ &= a_1(t - t_{cathode}) + a_0 && \text{(A.5)} \end{aligned}$$

The time where $t \to t_{cathod}$ is cut by the criterion $|y'| < 0.5$. For those anodes where the corrections would lead to local maxima in the drifttime to driftdistance relation, the corrections are switched off. The corrections are relatively small for most of the wires in the outer chamber, but more important in the inner chamber with its longer driftdistances and for the wires which are close to the boundaries of the chamber. Again in this procedure the residuals are used, and Δa_1 and Δa_0 are determined. This procedure is iterated several times until the constants are stable. The results of this calibration as shown in figure A.3. Figure A.4 shows that a resolution degradation is present only on the very edge of the halfsectors.

As mentioned above, the whole process of global and single wire calibration is iterated several times. If the constants are stable, the fill vertices are redetermined and the calibration process is redone until all observed changes in the parameters are small. Crosschecks can be done by using dielectrons and looking for the matching between the TEC and the BGO.

For the 1992 data, with which the main parts of the method are developed, a

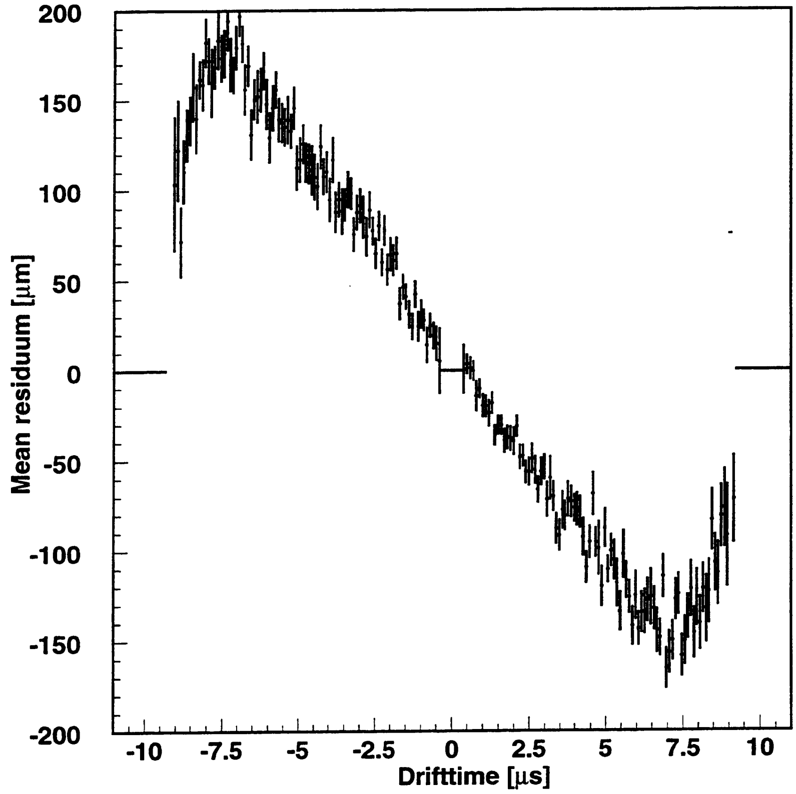

Figure A.1: The mean residuals of the last wire of all outer TEC sectors as a function of drifttime, before the calibration process.

momentum resolution of $1.8\% \cdot p_{t_{Beam}}[GeV]$ and a resolution of 109 μm for the distance of closest approach DCA was obtained [55] for more than 80% of the tracks. The average resolution can be seen in figure A.5. The dependence of the resolution on local ϕ is shown in figure A.6. There also the zones, where cathodes or anodes are found, are clearly indicated. Since the lifetime tag which was used to classify b-events and which was described in the analysis, is very sensitive to the DCA resolution, this areas must be taken out of the acceptance. The result for the 1992 data was reproduced for the 1991 and 1993 data.

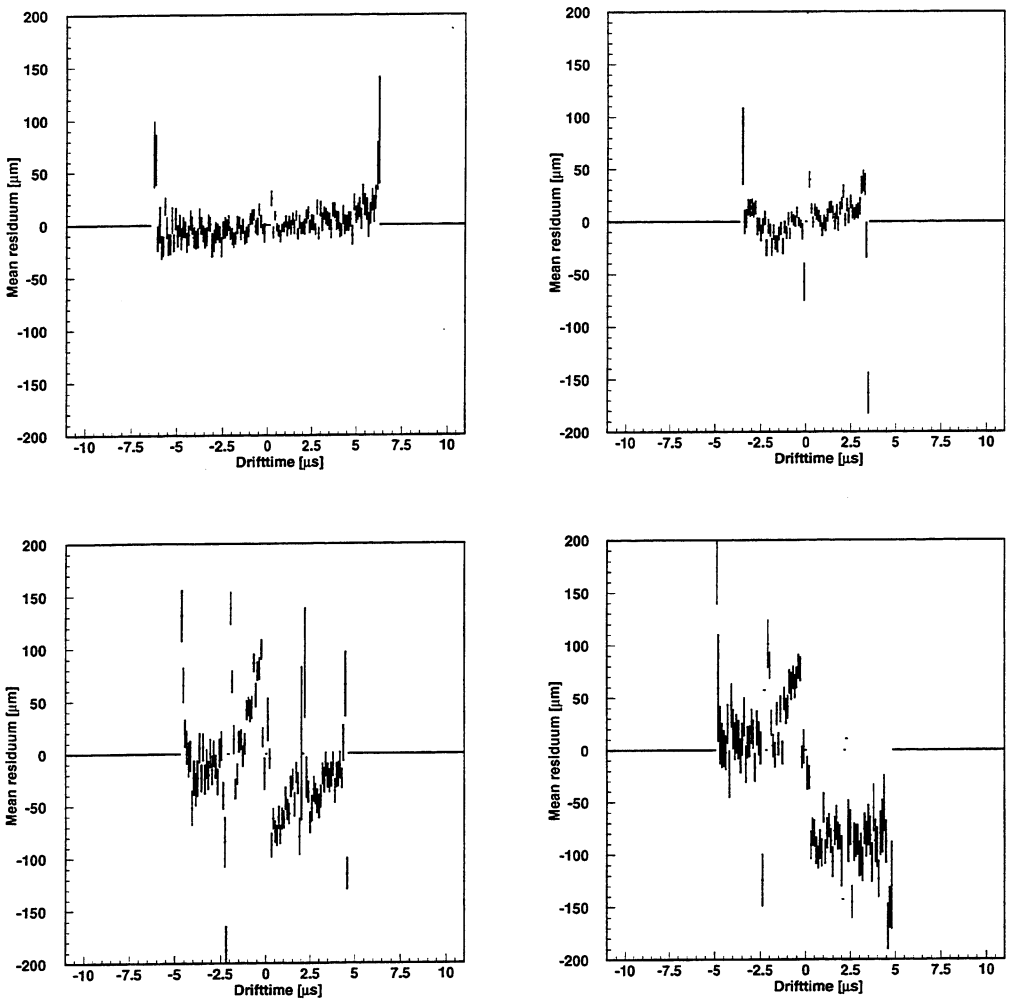

Figure A.2: The mean residuals per wire, integrated over all sectors as a function of drifttime, before the calibration process. The upper plots show on the left an average outer wire, the right the first outer wire. The lower plots show on the left the first wire of the inner and the second wire of the inner chamber. The second wire of the inner chamber is a charge division wire.

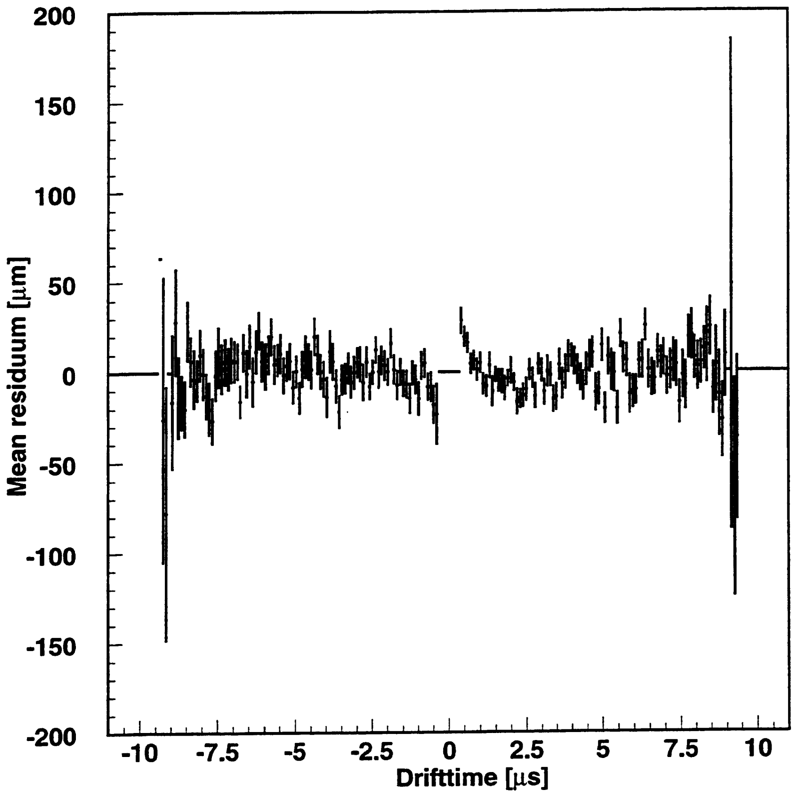

Figure A.3: The mean residuals of the last wire of all outer TEC sectors versus drifttime, after the calibration process.

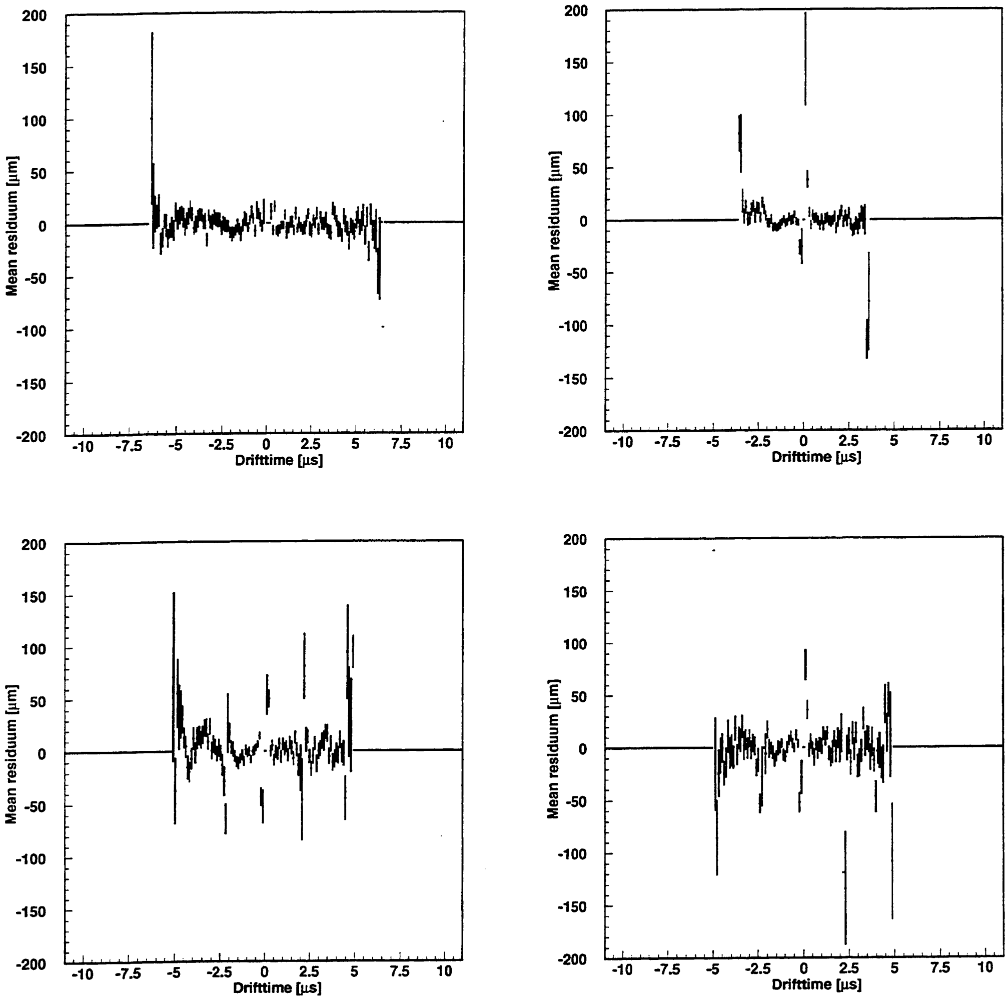

Figure A.4: The mean residuals per wire integrated over all sectors versus drift-time, after the calibration process. The upper plots show on the left an average outer wire, on the right the first outer wire. The lower plots show on the left the first wire of the inner and on the right the second wire of the inner chamber.

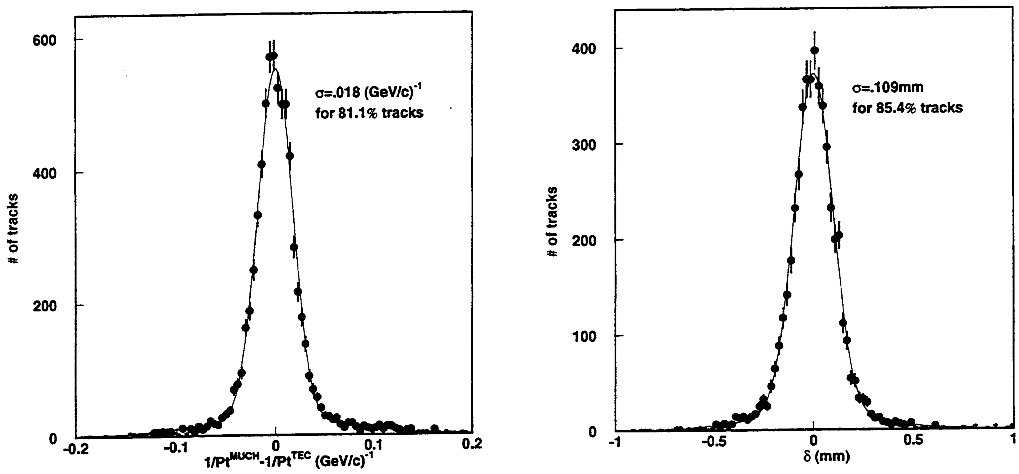

Figure A.5: Left the resolution for transverse momentum with respect to the muon chamber measurement. The DCA resolution measured with Z $\rightarrow$ e^+e^- events.

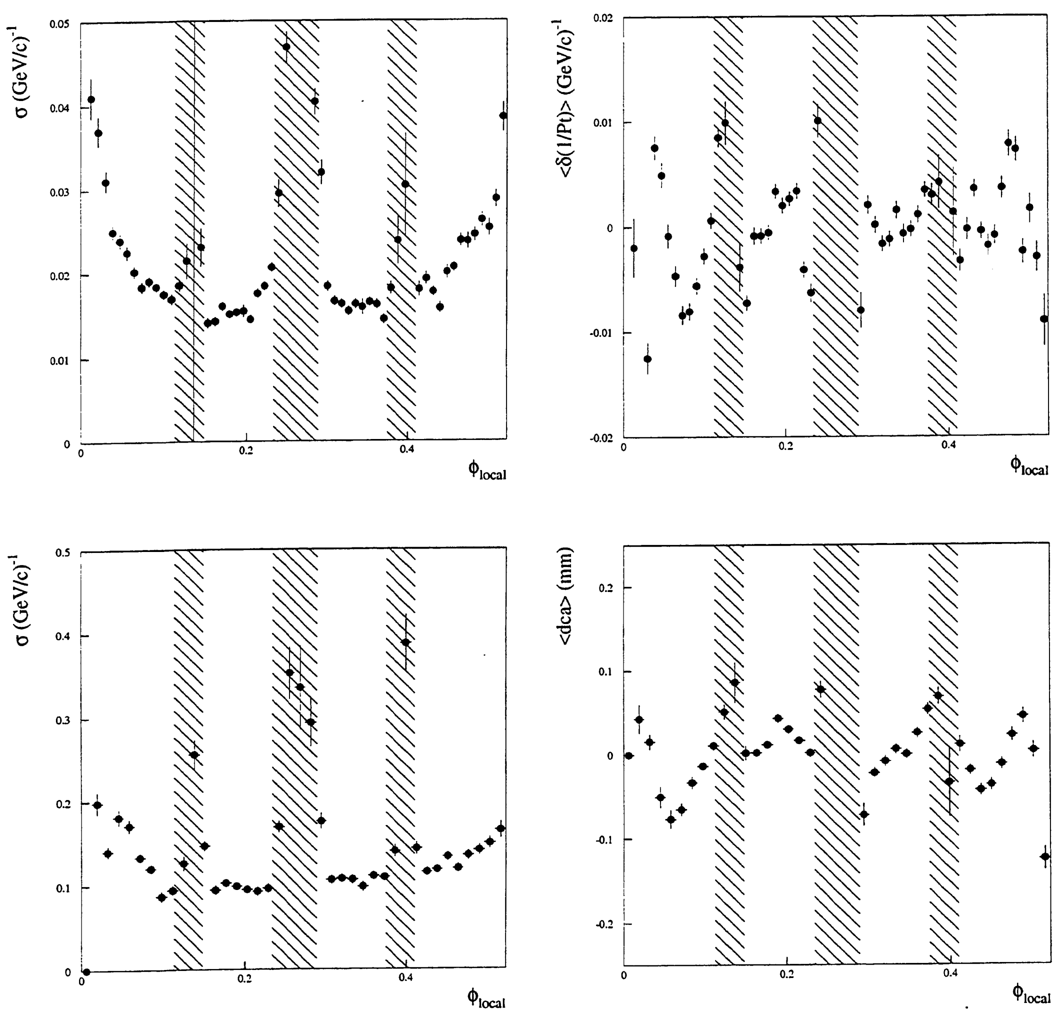

Figure A.6: The upper left plot shows the transverse momentum resolution as a function of local ϕ of an inner sector, the upper right plot shows the systematic offset of this distribution. The lower plots show the same for the DCA resolution.

Bibliography

[1] S.L. Glashow, Partial-Symmetries of Weak Interaction, Nucl. Phys. **22** (1961) 579

[2] A. Salam, in Elementary Particle Theory, ed. N. Svartholm, p. 367, Almqvist and Wiksell, Stockholm, 1968

[3] S. Weinberg, A model of leptons, Phys. Rev. Lett. **19** (1967) 1264

[4] Reports of the Working Group on Precision Calculations for the Z Resonance, CERN Report 95-03, eds. D. Barkin,W. Hollik and G. Passarino

[5] The LEP Electroweak Working Group and the SLD Heavy Flavor Group, A Combination of Preliminary LEP and SLD Electroweak Measurements and Constraints on the Standard Model, Internal Report LEPEWWG/96-02, ALEPH 96-107 PHYSIC 96-98, DELPHI 96-121 PHYS 631, L3 Note 1975, OPAL Technical Note TN 399, SLD Physics Note 52, 1996, Prepared from Contributions of the LEP and SLD Experiments to the 1996 summer conferences

[6] A.J. Buras and M.K. Harlander, A Top Quark Story: Quark mixing, CP Violation and Rare Decays in the Standard Model, in Heavy Flavours, ed. A.J.Buras and M.Lindner, volume 10 of *Advance Series on Directions in High Energy Physics* World Scientific, 1992

[7] W. Hollik, Electroweak Radiative Corrections, M_Z, M_W, and the Heavy Top, in Heavy Flavours, ed. A.J.Buras and M.Lindner, volume 10 of *Advance Series on Directions in High Energy Physics* World Scientific, 1992

[8] Francis Halzen and Alan D. Martin, Quarks & Leptons, John Wiley & Sons, 1984

[9] UA1 Collaboration, G. Arnison et al., Experimental Observation of Isolated Large Transverse Energy Electrons with Associated Missing Energy at $\sqrt{s} =$ 540GeV, Phys. Lett. **B122** (1983) 103

[10] UA2 Collaboration, M. Banner et al., Observation of Single Isolated Electrons of High Transverse Momentum in Events with Missing Transverse Energy at the CERN anti-p p collider, Phys. Lett. **B122** (1983) 476

[11] UA1 Collaboration, G. Arnison et al., Experimental Observation of Lepton Pairs of Invariant Mass around 95 GeV/c^2 at the CERN SPS collider, Phys. Lett. **B126** (1983) 398

[12] UA2 Collaboration, P. Bagnaia et al., Evidence for $Z^0 \rightarrow e^+e^-$ at the CERN anti-p p collider, Phys. Lett. **B129** (1983) 130

[13] CDF Collaboration, F. Abe et al., Observation of Top Prodction in $p\bar{p}$ Collisions with the Collider Detector at Fermilab, Phys. Rev. Lett. **74** (1995) 2626

[14] D0 Collaboration, S. Abachi et al., Observation of the top quark, Phys. Rev. Lett. **74** (1995) 2632

[15] The LEP Electroweak Working Group, A Combination of Preliminary LEP Electroweak Results for the 1995 Summer Conferences, Internal Report LEPEWWG/95-02, ALEPH 95-093 PHYSIC 95-086, DELPHI 95-137 PHYS 562, L3 Note 1814, OPAL Technical Note TN312, 1995

[16] CDF Collaboration, Electroweak Measurements from CDF, Preprint eps024, EPS, 1995, Contribution to the International Europhysics Conference on High Energy Physics

[17] S.L. Glashow,J. Iliopoulos and L. Maiani, Weak Interactions with Lepton-Hadron Symmetry, Phys. Rev. **D2** (1970) 1285

[18] P. Becher, M. Böhm and H. Joos, Eichtheorien der starken und elektroschwachen Wechselwirkung, B. G. Teubner, second edition, 1983

[19] J.H. Christenson,J.W. Cronin,V.L. Fitch and R. Turlay, Evidence for the 2π Decay of the K_2^0 Meson, Phys. Rev. Lett. **13** (1964) 138

[20] M. Kobayashi and M. Maskawa, CP-Violation in the Renormalizable Theory of Weak Interaction, Prog. Theor. Phys. **49** (1973) 652

[21] R.N. Mohapatra, J.C. Pati and L. Wolfenstein, Superweak model of CP violation in unified gauge theory, Phys. Rev. **D11** (1975) 3319

[22] Particle Data Group, M. Aguilar-Benitez et al., Review of Particle Properties, Phys. Rev. **D50** (1994) 1173

[23] L. Wolfenstein, Parametrization of the Kobayashi-Maskawa Matrix, Phys. Rev. Lett. **51** (1983) 1945

[24] S. Pokorski, Gauge Field Theories, Cambridge Monographies on Mathematical Physics Cambridge University Press, 1987

[25] J. Honerkamp, Stochastische Dynamische Systeme, VCH Verlagsgesellschaft, 1990

[26] C. Itzykson and J.B. Zuber, Quantum Field Theory, McGraw-Hill, 1985

[27] CLEO Collaboration,M.S. Alam, First Measurement of the Rate for the Inclusive Radiative Penguin Decay $b \rightarrow s\gamma$, Phys. Rev. Lett. **74** (1995) 2885

[28] M. Neubert, Heavy-Quark Symmetry, Phys. Rep. **245** (1994) 259

[29] G. Altarelli, N. Cabibbo, G. Carbó, L. Maiani and G. Martinelli, Leptonic decay of heavy flavors: a theoretical update, Nucl. Phys. **B208** (1982) 365

[30] N. Isgur et al., Semileptonic B and D decays in the quark model, Phys. Rev. **D39** (1989) 799

[31] J.G. Körner and G.A. Schuler, Exclusive semileptonic decays of bottom mesons in the spectator quark model, Z. Phys. **C38** (1988) 511, erratum ibid. **C41** (1989) 690

[32] M. Wirbel, B. Stech, M. Bauer, Exclusive Semileptonic Decays of Heavy Mesons, Z. Phys. **C29** (1985) 637

[33] ALEPH Collaboration, A Precise Measurement of the Average b Hadron Lifetime, Preprint eps0413, EPS, 1995, Contribution to the International Europhysics Conference on High Energy Physics

[34] L3 Collaboration, O. Adriani et al., Measurement of the Average Lifetime of b Hadrons, Phys. Lett. **B317** (1993) 474

[35] DELPHI Collaboration, P. Abreu et al., Updated Precision Measurment of the Average Lefetime of B Hadrons, Preprint CERN-PPE/96-13, CERN, 1996

[36] OPAL Collaboration, P.D. Acton et al., Measurement of the average b hadron lifetime in Z^0 decays, Z. Phys. **C 60** (1993) 217

[37] J.R. Patterson, Weak and Rare Decays, in Proceedings of the XXVII International Conference on High Energy Physics, Glasgow, ed. P.J. Bussey and I.G. Knowles, p. 149 International Union of Pure and Applied Physics, Institute of Physics Publishing, 1994

[38] M. Gronau and S. Wakaizumi, Testing the chirality of b to c coupling in $\mathrm{B} \to \mathrm{D}^*\ell\nu$, Phys. Lett. **B280** (1992) 79

[39] M. Dittmar and Z.Wąs, How to measure the structure of the weak charged current in semileptonic b decays, Phys. Lett. **B332** (1994) 168

[40] M. Creutz, Quarks, gluons and lattices, Cambridge Monographs on Mathematical Physics Cambridge University Press, 1985

[41] G. Altarelli and G. Parisi, Asymptotic Freedom in Parton Language, Nucl. Phys. **B126** (1977) 298

[42] T. Sjöstrand, The Lund Monte-Carlo for jet fragmentation and e^+-e^- physics Jetset version 6.2, Comp. Phys. Comm. **39** (1986) 367

[43] T. Sjöstrand and M. Bengtsson, The Lund Monte-Carlo for jet fragmentation and e^+-e^- physics Jetset version 6.3 - an update, Comp. Phys. Comm. **43** (1987) 367

[44] G. Marchesini and B. Webber, Monte Carlo simulation of general hard processes with coherent QCD radiation, Nucl. Phys. **B310** (1988) 461

[45] G. Marchesini et al., Herwig 5.1 - a Monte Carlo event generator for simulating hadron emission reaction with interfering gluons, Comp. Phys. Comm. **67** (1992) 465

[46] C. Peterson et al., Scaling violations in inclusive e^+e^- annihilation spectra, Phys. Rev. **D27** (1983) 105

[47] C.Q. Geng, Remarks on charge quantization of fermion and bosons, Phys. Rev. **D41** (1990) 1292

[48] A. Abbas, Spontaneus symmetry breaking, quantization of the electric charge and the anomalies, J. Phys. **G16** (1990) L 163

[49] Rabindra N. Mohapatra, Unification and Supersymmetry, Graduate Texts in Contemporary Physics Springer-Verlag, 2ndth edition, 1992

[50] J. Wess and B. Zumino, Supergauge Transformation in Four Dimension, Nucl. Phys. **B70** (1974) 39

[51] Y. Grossman and Z. Ligeti, The inclusive $\bar{B} \to \tau\bar{\nu}X$ decay in two Higgs doublet models, Phys. Lett. **B332** (1994) 373

[52] Reports of Activities in the Divisions, Internal report, CERN, 1994, Annual Report 1994-Volume II

[53] L3 Collaboration, B. Adeva et al., The Construction of the L3 Experiment, Nucl. Inst. Meth. **A289** (1990) 35

[54] R.L. Glückstern, Uncertainties in track momentum and direction due to multiple scattering and measurement errors, Nucl. Inst. Meth. **24** (1963) 381

[55] F. Behner, G. Rahal-Callot and P.Zemp, TEC calibration and performaces in 1992, Internal Report L3 note 1528, L3, 1993

[56] The L3-BGO Collaboration, Calibration of the L3 electromagnetic calorimeter in electron beam, Internal Report L3 Note 1712, 1995

[57] K. Kleinknecht, Detektoren für Teilchenstrahlung, Teubner Studienbücher:Physik Teubner, 1992

[58] L3 Collaboration, O. Adriani et al., Results from the L3 Experiment at LEP, Physics Reports **236** (1993) 1

[59] CERN, The ZEBRA system, February 1995, CERN program library long writeups Q100/Q101

[60] L3 Collaboration, B. Adeva et al., Measurement of Electroweak Parameters from Hadronic and Leptonic Decays of the Z^0, Z. Phys. **C51** (1991) 179

[61] HRS Collaboration, P.Keston et al., Comparison of light and charm quark fragmentation, Phys. Lett. **B161** (1985) 412

[62] Y. Karyotakis and M. Wadhwa, Results of the Energy Calibration on the Low Energy Electromagnetic Bumps, Internal Report L3 Note 1727, 1995

[63] A. Ricker, G-factors, Internal Report L3 Note 1394, 1993

[64] A. Kunin, M. Maity and G. Marjunder, G-factors, Internal Report L3 Note 1840, 1995

[65] The L3 detector simulation is based on GEANT Version 3.15.
See R. Brun et al., "GEANT 3", CERN DD/EE/84-1 (Revised), September 1987.
The GHEISHA program (H. Fesefeldt, RWTH Aachen Report PITHA 85/02 (1985)) is used to simulate hadronic interactions.

[66] DELCO Collaboration, W. Bacino et al., Semileptonic decays of the D meson, Phys. Rev. Lett. **43** (1979) 1073

[67] MARK-III Collaboration, R.M. Baltrusaitis et al., Direct Measurement of the Charmed D^+ and D^0 Semileptonic Branching Ratios, Phys. Rev. Lett. **54** (1985) 1976

[68] ARGUS Collaboration, H. Albrecht et al., A model-independent determination of the inclusive semileptonic decay fraction of B mesons, Phys. Lett. **B318** (1993) 397

[69] The LEP Collaborations, Combining Heavy Flavour Electroweak Measurements at LEP, Preprint PPE/96-017, CERN, 1996, Submitted to Nucl. Inst. Meth.

[70] Ulrich Uwer, Messung der Myonpaarproduktion auf der Z-Resonanz, Ph.D. thesis, RWTH Aachen, December 1994

[71] L3 Collaboration, B. Adeva et al., Measurement of $Z^0 \to b\bar{b}$ Decays and the Semileptonic Branching Ratio $\mathrm{Br}(b \to l + X)$, Phys. Lett. **B261** (1991) 177

[72] L3 Collaboration, M. Acciarri et al., Measurement of the Weak Charged Current Structure in Semileptonic b-Hadron Decays at the Z Peak, Phys. Lett. **B351** (1995) 375

[73] S. Brandt, Datenanalyse, Bibliographisches Institut-Wissenschafts Verlag, third edition, 1992

[74] F. Behner, The Inclusive Semileptonic Branching Ratios of B-Hadrons at LEP, in Proceedings of the International Europhysics Conference on High Energy Physics, ed. C. Vander Velde J. Lemonne and F.Verbeure, p. 448, World Scientific Publishing, 1996

[75] DELPHI Collaboration, P. Abreu et al., Measurement of $\frac{\Gamma_{b\bar{b}}}{\Gamma_{had}}$ using Impact Parameter Measurements and Lepton Identification, Zeit. Phys. **C 66** (1995) 323

[76] OPAL Collaboration, R. Akers et al., Measurement of B^0-$\bar{B}^0$ mixing, $\Gamma(Z^0 \to b\bar{b})/\Gamma(Z^0 \to$ hadrons and semileptonic branching ratios for b-flavoured hadrons in hadronic Z^0 decays, Z. Phys. **C60** (1993) 199

[77] CLEO Collaboration, B. Barish et al., Measurement of the B Semipleptonic Branching Fraction with Lepton Tags, Phys. Rev. Lett. **76** (1996) 1570

[78] I. Bigi, B. Blok, M. Shifman and A. Vainshtein, The baffling semileptonic branching ratio of B mesons, Phys. Lett. **B323** (1994) 408

[79] Y. Nir, The mass ratio m_c/m_b in semileptonic b-decays, Phys. Lett. **B221** (1989) 184

[80] P. Ball and U. Nierste, Mass definition in heavy quark effective theory and a new determination of V_{cb}, Phys. Rev. **D50** (1994) 5841

[81] P. Ball, M. Beneke and V.M. Braun, Resummation of Running Coupling Effects in Semileptonic B Meson Decays and Extraction of $|V_{cb}|$, Phys. Rev. **D52** (1995) 3929

[82] ARGUS Collaboration, H. Albrecht et al., Reconstruction of semileptonic b$\to$u decays, Phys. Lett. **B255** (1991) 297

[83] CLEO Collaboration, J. Bartelt et al., Measurement of Charmless Semileptonic Decays of B Mesons, Phys. Rev. Lett. **71** (1993) 4111

[84] M. Neubert, Uncertainties in the Determination of $|V_{cb}|$, in '95 Electroweak Interactions and Unified Theories, Les Arcs, ed. J. Trân Thanh Vân, Moriond Particle Physics Meetings:Leptonic Session, p. 169, Editions Frontieres, 1996

[85] M. Neubert, Model Independent Extraction of V(cb) from semileptonic decays, Phys. Lett. **B264** (1991) 455

[86] ALEPH Collaboration, D. Buskulic et al., A Measurment of $|V_{cb}|$ from $\bar{\mathrm{B}}^0 \to \mathrm{D}^{*+}\ell^-\bar{\nu}_\ell$, Phys. Lett. **B359** (1995) 236

[87] DELPHI Collaboration, D. Buskulic et al., Determination of $|V_{cb}|$ from semileptonic decay $\bar{\mathrm{B}}^0 \to \mathrm{D}^{*-}\ell^+\nu$, Preprint CERN-PPE/96-11, CERN, 1996

[88] P. Heiliger and L.M. Sehgal, Semileptonic decays of b-mesons into tau tau-neutrino, Phys. Lett. **B229** (1989) 409

[89] A.F. Falk, Z. Ligeti, M. Neubert and Y. Nir, Heavy quark expansion for the inclusive decay anti-B $\to$ tau anti-neutrino X, Phys. Lett. **B326** (1994) 145

[90] ALEPH Collaboration, D. Buskulic et al., Measurment of the $b \to \tau^-\bar{\nu}_\tau X$ Branching ratio and an Upper Limit on $\mathrm{B}^- \to \tau^-\bar{\nu}_\tau$, Phys. Lett. **B343** (1995) 444

[91] L3 Collaboration, M. Acciarri et al., Measurement of the Inclusive b $\to \tau\nu$X Branching Ratio, Phys. Lett. **B332** (1994) 201

[92] OPAL Collaboration, Measurement of the branching ratios b $\rightarrow \tau^-\bar{\nu}_\tau$X and b $\rightarrow$ D$^{*+}\tau^-\bar{\nu}_\tau$(X), Internal Report OPAL Physics Note PN209, 1996, Contributed paper to ICHEP96, Warsaw

[93] C.H. Chang and C. Lü, Implications on two Higgs doublet models from the latest $b \rightarrow s\gamma$ measurement and top discovery, Preprint AS-ITP-95-23, hep-ph/9507384, CCAST (world Laboratory) and Institute of Theoretical Physics, Academia Sinica, Beijing, 1995

Acknowledgement

I thank Prof. H. Hofer for the hospitality and friendly atmosphere at his institute and the interesting discussions about scientific policy in the monthly ETH group meetings.

I am grateful to J. Ulbricht and M. Pohl, who introduced me to the institute. I thank particulary M. Pohl for the academic freedom in his group, which was at the same time connected with his personal support and good advice especially during the write up.

My gratitude is also for G. Rahal, with whom I had excellent cooperation and who supported me during the time, when we did the TEC calibration. I like to thank A. Biland for all the explanation on how to calibrate a device by itsself and all the computer talk. I am thankful to D. McNally for explaning me all the mysteries of charge division wires.

Thanks also to G.Kogler, the heart and soul of the ETH-CERN group.

Since I did so much system administration stuff, it is a joy to thank T.Bell from IBM for his patience, support and explanations during those years.

I thank V.Brigljevic for his assistants in the system administration during the hot final phase of this thesis, and for the basketball games on monday.

My thanks C.M.E. Paus for helping us with the correctly normalized line shape plots.

To P. Zemp I want to express my thankfulness for friendship, cooperation, skiing and nice evenings we shared together.

My gratitude is for M. Dittmar who impressed me by his "gut" feeling on physics and who gave me the know how to fudge right. He has been more than once the driving force which brought our small group Peter, him and me ahead.

I like to thank Prof. F.Pauss for acting as my co-examiner and her support during the critical phase of the discussion "What comes after".

I am grateful to all the people in L3 who made the experiment work as well as all the world wide taxpayers which finance all this.

Finally I want to thank my wife Eva, without her support and her patience this work would have been impossible.

Curriculum Vitae

- Born on November the 20$^{\text{th}}$, 1963, in Cologne, Germany
- Autum 1971 beginning of primary school in Cologne
- Spring 1972 moved to Saarlouis, Germany
- Autum 1974 beginning of secondary school at the Robert-Schuman-Gymnasium Saarlouis
- Spring 1984 Abitur
- Autum 1984 beginning of the physics studies at the Rheinische-Friederich-Wilhelms Universität Bonn
- Autum 1986 Vordiplom in physics at the Universität Bonn
- Autum 1987 changed to Eidgenössische Technische Hochschule Zürich as Hörer in Fortbildung
- Autum 1988 exam to be full student at ETH
- Autum 1990 diploma in physics with a thesis in lattice QCD "Eigenschaften von Quarkpropagatoren in der Confinementphase" at the theory departement of PSI under supervision of F. Jegerlehner
- Winter 1990/91 Programmer at Computer Gesellschaft Konstanz, Germany
- Since February 1991 Ph.D. student at the Labor für Hochenergiephysik of the ETH, working on TEC calibration, computer system administration and analysis of b-decays